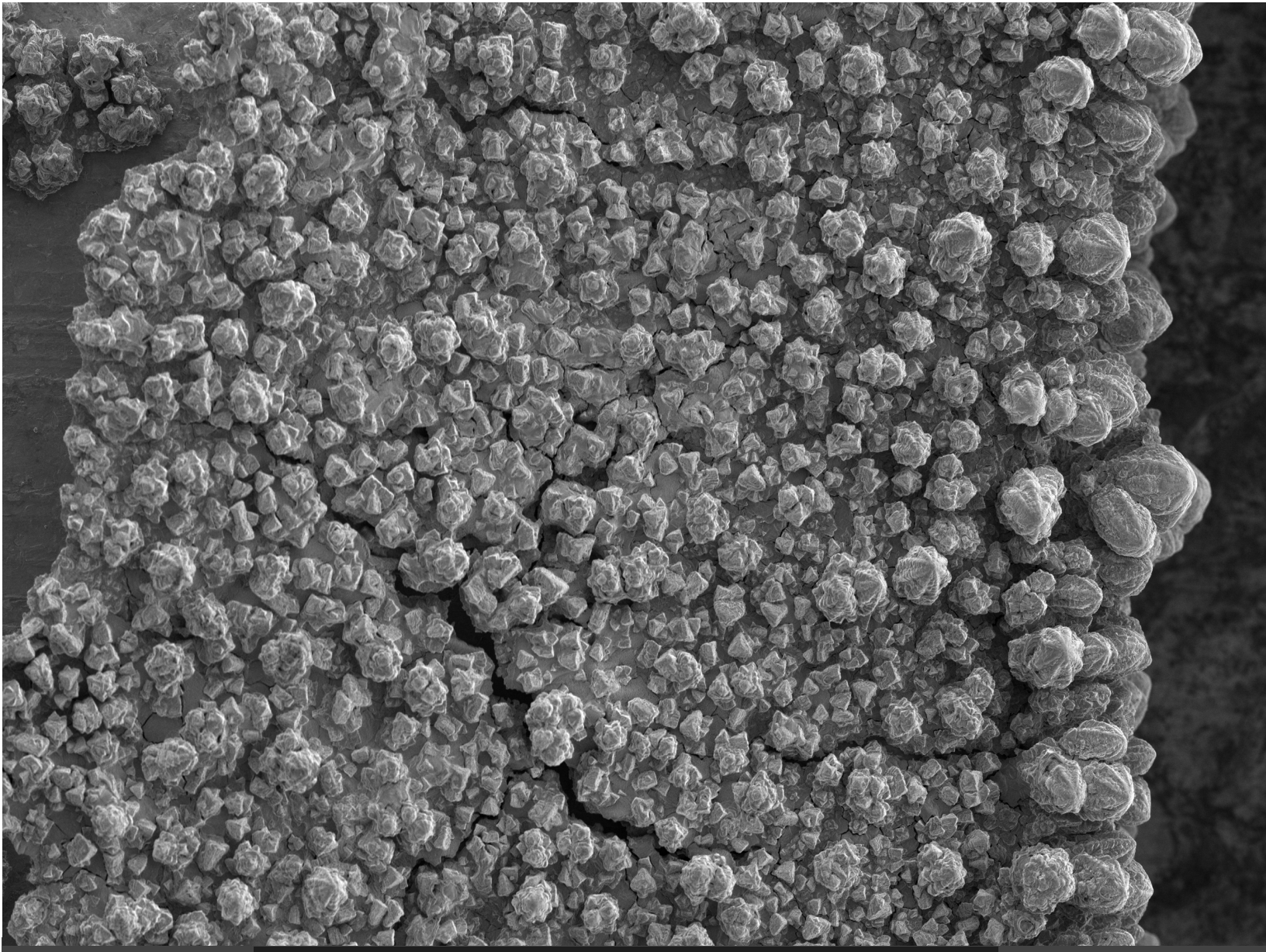

Optimal electrode material study for an alkaline electrolyser integrated into a micro-scale methanol plant

by
Rodrigo Martínez Picazo

TU Delft

ZEF

Optimal electrode material study for an alkaline electrolyser integrated into a micro-scale methanol plant

Zero Emission Fuels

by

Rodrigo Martínez Picazo

to obtain the degree of Master of Science
at the Delft University of Technology,
to be defended on Thursday May 28, 2020 at 1:45 PM

Student number	4746422	
Project duration:	February 2019 - May 2020	
Thesis Committee	Prof.dr. FM Mulder	TU Delft (chair)
	Dr.ir. D.A. Vermaas	TU Delft (supervisor)
	Dr. ir. J.W. Haverkort	TU Delft
	Ir. Jan van Kranendonk	ZEF (supervisor)

TU Delft

Z E F

Abstract

Zero Emission Fuels B.V. (ZEF) is developing an integrated micro-plant to produce methanol from captured CO_2 and green Hydrogen produced via alkaline water electrolysis. The electrolysis unit represents one of the largest financial and energetic costs in the system and is required to operate at 166 mA/cm^2 under 2 V. In order to decrease the costs, ZEF is looking to synthesize highly efficient nickel-based electrodes to avoid using expensive noble-metal ones.

The objective of this work was the synthesis of efficient and stable nickel-based electrodes. Two electrodes were synthesized through electrodeposition (Raney nickel and NiFe) and one was synthesized through hydrothermal treatment (NiFe-LDH) and were compared to a RuO_2-containing (Permascand) electrode and to a smooth nickel electrode. On/off cycles for 2.5 hours were carried out to measure the stability of the electrodes. Additionally, performance tests in a pressure range of 1-5 bar were carried out to measure the effect of increasing pressure. The experiments were carried out in an in-house designed and built zero-gap alkaline electrolysis cell.

Raney nickel, with a measured roughness factor of 150 was the best performing of the synthesized electrodes. After the stability tests, it was able to produce 166 mA/cm^2 at 1.9 V (1.73 and 2.12 V for Permascand and smooth nickel, respectively). Raney nickel as anode material presented significant degradation. Raney nickel is the most promising material for HER, none of the synthesized materials presented significant stability for OER.

From the nickel-iron electrodes, NiFe with a roughness factor of 19.5 presented the best performance of the synthesized materials with 2.04 V for the mentioned current density. NiFe presented significant degradation, especially as anode material. NiFe presented a relative high performance considering its low electrochemical active surface area attributed to the presence of highly efficient active sites. NiFe-LDH was quickly degraded during the tests as cathode and anode material.

The pressure tests showed an inverse relationship between voltage and pressure. This hints that a decrease in bubble size with pressure is the cause behind the decrease in voltage. A simple model, based on experimental data and thermodynamic considerations, estimated that operating the cell at 50 bar reduces the voltage by 0.25 V compared to operation at 1 bar. The estimated reduction in voltage at a pressure of 50 bar would allow to operate the electrolysis cell under 2 V even with smooth nickel mesh as electrode.

Acknowledgments

I would firstly like to thank may supervisors Dr.ir. D.A. Vermaas and Jan van Kranendonk for their help throughout this project and for sharing their knowledge with me. I would also like to mention that I appreciate their understanding and flexibility. I would also like to thank everybody at ZEF, especially Ulrich Starke and Hessel Jongebreur for their support and encouragement. Special thanks to Peter for helping me out with the setup.

I would like to thank students and supporting staff at the Transport Phenomena group and in the Chemical Engineering department in general. Special thanks to Christiaan Schinkel and Lorenz Baumgartner for their help in the lab. I would also like to thank my thesis committee, Prof.dr. FM Mulder and Dr. ir. J.W. Haverkort, for taking the time to review my work and for their flexibility as well.

I would like to remind me myself how important health, well-being and friendship are. And that success stems from happiness and not the other way around. I thank Moisés for starting this journey with me, and I would like to thank Elda, Ignacio, Keshav and Yasmin for sharing theirs with me. I, of course, thank my parents for supporting me in my studies and life. I understand that their effort and help have taken me to where I am, and I am deeply grateful for that.

Rodrigo Martínez Picazo
Delft, May 2020

Contents

List of Figures

List of Tables

List of Symbols

C_{DL}	Double-layer capacitance
α	Symmetry coefficient
η	Overpotential
Ω	Ohm
ΔG	Gibbs free energy
A	Electrode geometric area
a	Activity
b	Tafel slope
C	Concentration
d	Mean diameter
E	potential
F	Faraday constant
i	Current
j	Current density
j_o	Exchange current density
k	Rate constant
l	Spacing between electrodes
n	Number of electrons
P	Pressure
R	Universal gas constant
R_f	Roughness factor
s	Scanning rate
T	Temperature
v	Reaction rate
σ	Conductivity
N	Number of active sites
J_{ECSA}	Current density referred to ECSA

List of Abbreviations

AWE	Alkaline Water Electrolysis
BEC	Backscattered electron composition
C-PVC	Chlorinated polyvinyl chloride
DL	Double layer
ECSA	Electrochemical active surface area
EDS	Energy-dispersive spectroscopy
HER	Hydrogen evolution reaction
LDH	Layered double hydroxide
LFL	Lower flammability limit
MEA	Membrane electrode assembly
Nl	Normal litters
OER	Oxygen evolution reaction
PDA	Peripheral differential amplifier
PEM	Polymer electrolyte membrane
RDS	Rate determining step
RNi	Raney nickel
SEI	Secondary electron image
SEM	Scanning electron microscopy
SHE	Standard hydrogen electrode
TOF	Turn over frequency
XPS	X-Ray photoelectron spectrometer
ZEF	Zero Emission Fuels

1

Introduction

The threat of climate change resulting from greenhouse gases emissions, like CO_2, has boosted the search for alternative energy sources to decrease the use of fossil fuels and diminish their negative impact. The development of wind, solar and biomass energy has sought to decrease the consumption of coal and liquid fossil fuels for the production of electricity, and to power the global industry and transportation systems. There is, however, some limitations to these sustainable sources of energy. Biomass energy is limited by land resources and involves concerns regarding competition with food production. Wind and solar energy are challenged by the intermittent nature of their energy production capacity [1].

One way to solve the intermittency issue, is the use of energy storage or conversion to gain flexibility on when to use the energy produced. Electricity coming from a solar panel, for example, can be stored in a battery or can be used to produce hydrocarbons (together with CO_2) [1]. When the latter process produces a liquid hydrocarbon, it is known as Power-to-liquid. One of the most developed methods is the use of CO_2 and green H_2 to produce methanol [2]. Being a liquid fuel, methanol offers chemical stability as well as easy storage and transportation [3]. Methanol provides a solution to the challenges brought by the intermittent nature of solar or wind energy while having the stability and flexibility of biofuels.

The CO_2 needed for the synthesis of methanol can be sourced directly from air (direct air capture) or from carbon-rich waste streams. The green H_2 needed for the synthesis can be obtained from water electrolysis using electricity produced by non-fossil sources. The integration of CO_2 capture, production of H_2 and synthesis of methanol with a green source of energy represents an interesting opportunity to decrease CO_2 emissions while increasing the widespread use of sustainable energy sources[3].

1.1 Zero Emission Fuels (ZEF) and Alkaline Water Electrolysis

Zero Emissions Fuels (ZEF) is a start-up in Delft with the ambitious goal of creating a fully automated and modular methanol micro-plant. Air and solar energy are the only inputs for the synthesis of methanol. The creation of a micro-plant instead of an industry-sized methanol plant allows ZEF to greatly decrease the costs and time of development. Additionally, a system small in size allows for the technology to be deployed in big numbers helping to advance the implementation of solar energy. ZEF's final goal is to help fight climate change while producing innovative and integrated technology.

Figure 1.1 is a simplified explanation of the methanol synthesis process envisioned by ZEF. The process starts with the obtention of CO_2 and water directly from air with direct air capture. After desorption, CO_2 and water are separated in a degasser. The CO_2 is then sent to the methanol synthesis reactor while water is supplied to the electrolyser. The hydrogen obtained through electrolysis is then supplied to the methanol reactor. The final product needs to be distilled to decrease the water content and deliver 99.8% methanol. The energy driving the process is produced by three 300 W solar panels.

Water electrolysis is one of the main constraints in the development of the process. There are two main challenges for the development of the electrolyser: cost of electrodes and the energetic cost of the system. To circumvent the challenge, ZEF decided to implement alkaline water electrolysis (AWE) as it is possible to use abundant transition metal oxides as electrodes as opposed to using scarce noble metals, like Pt, in PEM electrolysis [4].

The most efficient electrode materials for AWE are RuO_2 and IrO_2, materials with high cost that would greatly increase the cost of the electrolysis unit [4]. Recent research indicates that nickel-based materials are very promising alternatives to noble metals. Nickel-based electrodes doped with iron and with large surface area are specially interesting due to their high performance [5]. ZEF is looking to research easy to manufacture nickel-based electrodes with high performance for AWE.

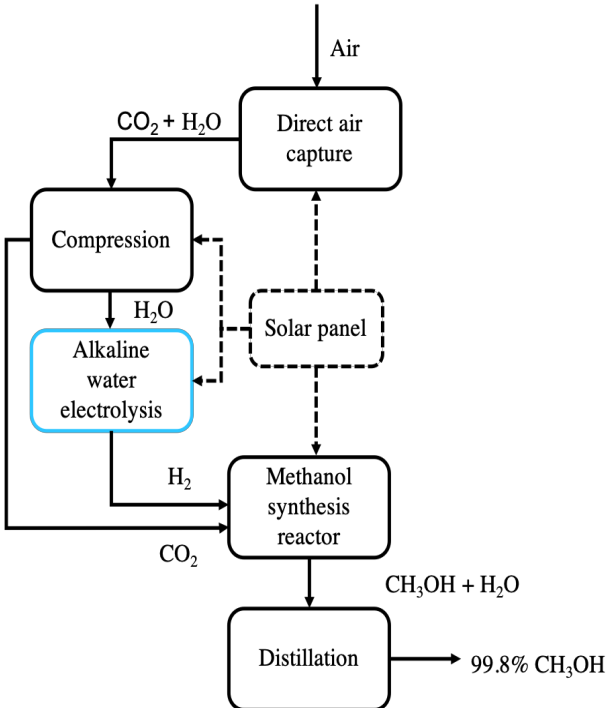

Figure 1.1. Schematic description of the methanol synthesis process envisioned by ZEF. Adapted from [6]

ZEF's electrolyser unit is based on the zero-gap concept for each of the individual cells, and the cells are connected in series with a concept similar to bipolar plates. The current requirements for the electrolyser prototype are presented in Table 1.1. The operating pressure of 50 bar is needed to meet the requirements of the methanol synthesis reactor. The operating temperature of 90ºC was selected to increase the efficiency of electrolysis and to provide preheated hydrogen to the methanol reactor.

Table 1.1. ZEF's current electrolyser prototype specifications

Design	Zero-gap
Operating pressure (bar)	50
Electrode geometric area (cm^2)[1]	60
Operating temperature (ºC)	90
Electrolyte concentration	30% wt. KOH
Operating voltage (max. per cell)	2 V
Operating current (A)[2]	10
Membrane material	ZirfonPerl UTP 500
Number of cells	20

[1]The geometric area used for this project was 30 cm^2.
[2]The current used for this project was 5 A.

1.2 Objective of thesis and research questions

The main objective of this thesis was the synthesis and testing of electrode materials for ZEF's zero-gap alkaline electrolysis unit. As mentioned before, nickel-based materials were selected for this project due to their low cost and promising performance. Synthesis techniques, such as electrodeposition and hydrothermal treatment, were selected for their simplicity, scalability and versatility for experimentation.

The electrochemical tests also functioned as a way to test ZEF's electrolyser unit as they were carried out on a simplified setup based on ZEF's prototype design. These tests verified the proper manufacturing of the prototype, electrical connections and zero-gap concept implementation. This represented the first-time electrolysis was performed on ZEF's current electrolyser prototype. The use of this setup also allowed to test the effect of pressure on voltage.

The need to find high performing and stable nickel-based electrode materials, and the need to understand the effect of pressure on the performance of the electrolyser led to the main research question (1) and secondary question (2):

1. What is the performance of in-house synthesized nickel-based electrodes?

    - What are the surface characteristics of synthesized materials?
    - What are the electrochemical parameters of synthesized materials?
    - What is the long-term stability of synthesized materials?
    - What are the surface changes impacting long-term stability of the synthesized materials?

2. What is the effect of high-pressure operation of a zero-gap alkaline water electrolyser?

    - What is the influence of an increasing pressure on the voltage required?
    - What is the most likely source of the observed pressure effect on voltage?

A commercially sourced highly active nickel-based electrode and bare nickel mesh will be used for performance comparison.

1.3 Report structure

The report is structured as follows: in chapter 2 an overview of AWE, nickel-based electrocatalysts and electrochemical reaction kinetics is given. Additionally, the effect of temperature, pressure and cell architecture is discussed. Chapter 3 gives insights on the electrochemical methods followed for the tests, electrocatalayst synthesis techniques, surface characterization techniques and setup description. Chapter 4 presents the results obtained giving special attention to stability of materials and the effect of pressure on the performance. Finally, chapter 5 closes the report with conclusions and recommendations.

2

Theory

Finding alternative materials for alkaline water electrolysis (AWE) electrodes requires an understanding of the fundamental thermodynamic and chemical concepts governing water electrolysis. More specific factors, such as electrolysis cell design and impact of operation parameters are needed to understand the expected performance of the ZEF alkaline water electrolyser. This chapter begins with AWE fundamentals in section 2.1. Section 2.1 gives insight about the zero-gap cell design and its advantages. The influence of temperature and pressure is briefly discussed in section 2.3. Section 2.4 discusses the fundamentals of electrode kinetics. Sections 2.5 and 2.6 go over the individual characteristics of HER and OER, respectively. Finally, section 2.7 gives insight on nickel-based electrocatalysts for AWE.

2.1 Alkaline water electrolysis fundamentals

Water electrolysis is the reaction of splitting water into its two components: hydrogen and oxygen. This reaction is non-spontaneous, and it needs an applied voltage to occur. Equation 2.1 presents the overall reaction including the hydrogen evolution reaction (HER) and oxygen evolution reaction (OER). The standard equilibrium potential for the reaction is 1.23 V. This means, that more than 1.23 V need to be applied to an electrolytic cell to split water [7]. The water electrolysis reaction is an endothermic reaction; heat needs to be provided for the reaction to proceed. The thermoneutral potential of 1.48 V represent the real equilibrium barrier to be overcome, this potential includes the heat consumed by the reaction [7].

$$H_2O \rightarrow H_2 + 1/2\, O_2 \tag{2.1}$$

Water electrolysis can occur in an acidic or alkaline medium, Figure 2.1 presents a simple AWE unit which consists of an anode and cathode connected to an external circuit for power supply. The electrodes are submerged in a conducting electrolyte, and each electrode is separated into a compartment with the help of an OH^- conducting membrane. The most common electrolyte is KOH with a concentration of 25-30 % wt.[8]. When a direct current is applied to the unit, electrons flow from the negative terminal of the power source to the cathode where a reduction reaction takes place and H_2 is produced (HER), at the same time,

an oxidation reaction takes place in the anode producing O_2 (OER). In the whole process, water molecules move to the cathode while hydroxide ions move towards the anode [7].

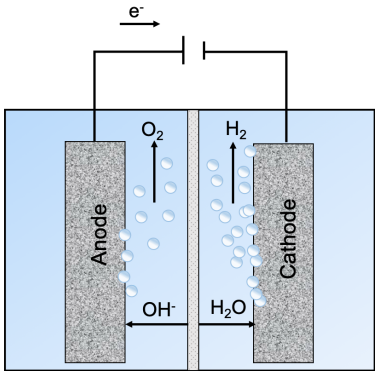

Figure 2.1. Schematic representation of an alkaline electrolysis cell.

The electrochemical reactions taking place in an alkaline electrolyte are presented in Equations 2.2 and 2.3.

$$Cathode: 2H_2O + 2e^- \rightarrow H_2 + 2\,OH^-(E^o = -0.83\,V\ vs\ SHE) \quad (2.2)$$

$$Anode: 2\,OH^- \rightarrow \frac{1}{2}O_2 + H_2O + 2e^-(E^o = 0.40\,V\ vs\ SHE) \quad (2.3)$$

The equilibrium voltage of an electrochemical cell can be obtained from the change in Gibbs free energy (ΔG) related to the redox reaction taking place. For the overall cell reaction, the Gibbs free energy expression is as follows:

$$\Delta G^o_{cell} = -nFE^o_{cell} \quad (2.4)$$

where n is the number of electrons exchanged, F is the Faraday constant and E^o_{cell} is the standard equilibrium potential for water electrolysis. The change in Gibbs free energy in the cell (ΔG_{cell}) in non-standard conditions is related to ΔG^o_{cell} through the equilibrium constant in the following expression:

$$\Delta G_{cell} = \Delta G^o{}_{cell} + RTln\left(\frac{p_{H_2}p_{O_2}^{1/2}}{a_{H_2O}}\right) \quad (2.5)$$

where p is the partial pressure of H_2 or O_2, a is the water activity, R is the ideal gas constant and T is the temperature. Equations 2.4 and 2.5 can be combined to obtain the Nernst equation (Eq. 2.6) to calculate the cell potential at different conditions.

$$E_{cell} = E^o_{cell} - \frac{RT}{nF} ln\left(\frac{p_{H_2} p_{O_2}^{1/2}}{a_{H_2O}}\right) \tag{2.6}$$

The measured voltage of an electrolysis cell not only depends on thermodynamics, the current (i) applied to the cell will influence overpotentials (η) as well as voltage drops related to resistances in the cell (R_{cell}). η is individually defined for one electrode according to Equation 2.7:

$$\eta = E - E^0 \tag{2.7}$$

where E corresponds to the measured voltage at the electrode and E^o is the standard potential for the reaction at the electrode. E is composed by the activation overpotential related to electrode kinetics, and by the Nernstian overpotential resulting from non-standard conditions of the reactants.

The ohmic losses at the cell consider electrical resistances in the circuit, resistance to ionic transport at the electrolyte solution and membrane (or separator). They also consider the ohmic losses due to the presence of gas bubbles at the electrode surface and adjacent electrolyte. The sum of all the resistances in an electrolysis cell are shown in Eq. 2.8.

$$R_{cell} = R_{electric} + R_{bubble,O2} + R_{electrolyte} + R_{membrane} + R_{bubble,H2} \tag{2.8}$$

To minimize the voltage needed for water splitting in the electrolysis cell, efficient electrocatalysts are needed to minimize η. This can be done with highly electro-active materials with high surface area [9]. For the cell resistances, electrochemical engineering can be applied to minimize the inter-electrode gap, to maximize ionic conductivity at the electrolyte and membrane, and to assure gas escapes from the electrode surface and electrode gap efficiently [10].

The measured voltage of an electrolysis cell is composed by the thermodynamic potential plus the kinetic and Nernstian overpotentials at the electrodes and ohmic losses at the cell (Eq. 2.9).

$$E_{cell} = E^o_{cell} + \sum \eta + iR_{cell} \tag{2.9}$$

The efficiency of an electrolysis cell can be calculated with Eq. (2.10). The thermoneutral potential of 1.48 V will be used in this work to quantify the efficiency of the cell.

$$efficiency: \frac{E^{o}_{cell}}{E_{cell}} 100\% \tag{2.10}$$

2.2 Alkaline electrolysis cell architecture: Zero-gap design

As mentioned before, alkaline electrolysis allows the use of cheaper and abundant materials for the electrodes [10]. Traditional alkaline electrolysis has some drawbacks, however. Low current densities of less than 0.25 Acm^{-2} and efficiencies below 60% are common [9]. In comparison, polymer electrolyte membrane (PEM) electrolysis can operate at 2 Acm^{-2} and an efficiency of 72% [9]. The advantages of PEM electrolysis are offset by the high cost of noble metal electrodes (Pt, Ir). For this reason, there is a significant interest in increasing the efficiency of alkaline electrolysis.

One way to increase the efficiency of an alkaline electrolyser is by changing the configuration of the membrane electrode assembly (MEA) [11]. The MEA for traditional alkaline electrolysis includes a space between the electrodes and the membrane which results in ohmic losses due to ionic transport. The zero-gap concept looks to diminish those ohmic losses [12]. Pressing porous or mesh-structured electrodes against the membrane results in a separation between both electrodes equal to the membrane thickness (< 0.5 mm) (see Figure 2.2) [10].

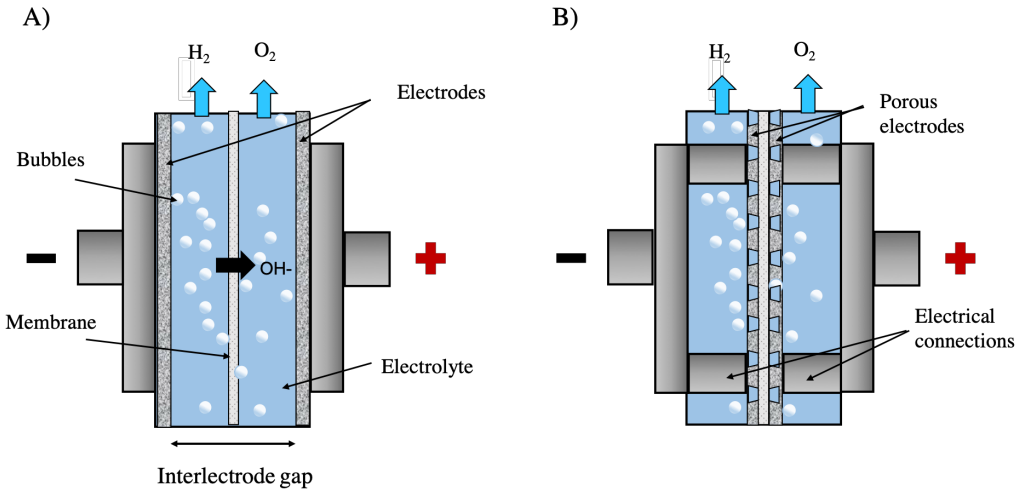

Figure 2.2. Schematic comparison of a traditional alkaline electrolysis architecture (a) and zero-gap configuration (b). Extended electrical connections can take the place of gas diffusion layers to electrically connect the electrodes while leaving space for the electrolyte.

The implementation of the zero-gap concept decreases the voltage drop related to the electrolyte resistance ($R_{electrolyte}$) as it decreases the distance between the electrodes and the membrane (see Eq. 2.11).

$$iR_{electrolyte} = \frac{il}{A\sigma} \tag{2.11}$$

where i is the current, l is the spacing between the electrodes and the membrane, A is the electrode surface area, and σ is the electrolyte conductivity.

The zero-gap configuration also affects the bubble resistance ($R_{bubbles}$) at the electrolyser. $R_{bubbles}$ is composed by two factors: 1) bubbles covering the surface of the electrodes and 2) bubbles creating a void volume between the electrodes. The second effect increases the resistance for the transport of hydroxide ions since the electrolyte solution is displaced by the bubbles. The negative effect of this void volume on ionic transport is diminished with the zero-gap architecture as the bubbles are forced to the back of the electrodes [10].

2.3 Influence of temperature and pressure on voltage

Increasing the operating temperature of an alkaline electrolyser has a positive impact on the voltage needed to drive water splitting. A higher temperature improves ionic conductivity in the electrolyte, and it also enhances the kinetics of the surface reaction at the electrodes. Temperature also influences the thermodynamic voltage which decreases with increasing temperature. However, increasing the temperature does have a negative effect, it increases the corrosive behavior of the electrolyte (*e.g,* KOH). Operating at high temperatures reduces the lifespan of the electrolyser components [8].

Increasing the operating pressure of an alkaline electrolyser increments the thermodynamic voltage according to Equation 2.6. However, it is believed that higher pressure decreases the ohmic loses related to the presence of gas bubbles. It has been reported that a pressure of 35 bar greatly reduce the size of bubbles produced at the electrodes [13]. Smaller bubbles represent a lower ohmic drop due to a lower void volume between the electrodes and less coverage of the electrodes surface [10].

2.4 Electrode kinetics: current density vs voltage

The electrical current density flowing through an electrolysis cell is proportional to the reaction rate, $\nu = j/nF$. Where j is the current density related to the electrode area. From experimental data, it is known that the reaction rate is a function of voltage [14].

Equation 2.12 represents the simplest redox reaction controlled by the transfer of an electron. The description of the kinetics starts with a forward oxidation reaction and backward reduction reaction.

$$R \leftrightarrow O + ne \tag{2.12}$$

The overall reaction rate is the difference between the oxidation rate and the reduction rate as presented in Equation 2.13:

$$v_{net} = K_{ox}C_{red}^{s} - K_{red}C_{ox}^{s} \tag{2.13}$$

where C_{red}^{s} and C_{ox}^{s} are the surface concentrations for the reduced and oxidized species, respectively. K_{ox} and K_{red} are the oxidation and reduction rate constants, respectively.

The observed *j* related to the electrode reaction is represented by equation 2.14:

$$j = Fv_{net} = F[K_{ox}C_{red}^{s} - K_{red}C_{ox}^{s}] \tag{2.14}$$

Equation 2.15 presents the individual *j* for the oxidation and reduction reactions.

$$j_{ox} = FK_{ox}C_{red}^{s}; \quad j_{red} = FK_{red}C_{ox}^{s} \tag{2.15}$$

Equation 2.16 presents the definition for the rate constants K_{ox} and K_{red}.

$$K_{ox} = k_o exp\left\{\frac{\alpha F(E-E^o)}{RT}\right\}; \; K_{red} = k_o exp\left\{-\frac{(1-\alpha)F(E-E^o)}{RT}\right\} \tag{2.16}$$

E is the potential applied to the electrode and E^orepresents the reference potential, in this case the standard potential. k_o is the rate constant at E^o and α is the symmetry coefficient. It indicates the fraction of change in E that leads to a change in *j* [14].

Combining the definitions presented in Equation 2.16 and Equation 2.14 we can write the Butler-Volmer equation (see Eq. 2.17).

$$j = Fk_o\left\{C_{red}^{s}exp\left(\frac{\alpha F(E-E^o)}{RT}\right) - C_{ox}^{s}exp\left(-\frac{(1-\alpha)F(E-E^o)}{RT}\right)\right\} \tag{2.17}$$

In general, E^o is not the potential reference in the situation of zero net current. E^{eq} is a more useful reference point and can be calculated with the Nernst equation presented in Equation 2.18:

$$E^{eq} = E^0 + \frac{RT}{F} ln \frac{C_{ox}^b}{C_{red}^b} \tag{2.18}$$

where C_{ox}^b and C_{red}^b are the bulk concentrations for the oxidized and reduced species, respectively. Using this relation and defining $\eta = E - E^{eq}$ we can write a second version of the Butler-Volmer expression (see Eq, 2.19).

$$j = Fk_o {C_{red}^b}^{(1-\alpha)} {C_{ox}^b}^{\alpha} \left\{ \frac{C_{red}^s}{C_{red}^b} exp\left(\frac{\alpha F\eta}{RT}\right) - \frac{C_{ox}^s}{C_{ox}^b} exp\left(-\frac{(1-\alpha)F\eta}{RT}\right) \right\} \tag{2.19}$$

Equation 2.19 can be simplified by assuming that mass transport from the bulk to the surface is much faster than the reaction rate, meaning that $C_{red}^s = C_{red}^b$ and $C_{ox}^s = C_{ox}^b$. This simplification results in equation 2.20:

$$j = j_o \left\{ exp\left(\frac{\alpha F\eta}{RT}\right) - exp\left(-\frac{(1-\alpha)F\eta}{RT}\right) \right\} \tag{2.20}$$

where j_o is the exchange current density defined by Equation 2.21:

$$j_o = Fk_o {C_{red}^b}^{(1-\alpha)} {C_{ox}^b}^{\alpha} \tag{2.21}$$

j_o is a kinetic parameter indicating the electron transfer activity at the electrode at equilibrium conditions.

Equation 2.20 can be simplified for high η, anodic or cathodic, leading to the simplified linear expression of the Tafel equation (Eq. 2.22). The value of the equation intercept can be used to calculate j_o at $\eta=0$ (equilibrium potential). The slope of the equation represents the Tafel slope, this value provides insight into the reaction mechanism and also indicates the rate at which η increases when increasing the current [15].

$$\eta = \frac{RT}{\alpha F} ln(j_0) - \frac{RT}{\alpha F} ln(j) \tag{2.22}$$

2.5 Hydrogen Evolution Reaction

The reaction happening at the cathode is the hydrogen evolution reaction (HER). In an alkaline electrolyte it corresponds to the reduction of water [15], the reaction mechanism can be described by a combination of the Volmer step and the Heyrovsky or Tafel steps:

(Volmer step) $$H_2O + e^- + M \leftrightarrow M - H + OH^-$$

(Heyrovsky step) $$M - H + H_2O + e^- \leftrightarrow H_2 + OH^- + M$$

(Tafel step) $$2M - H \leftrightarrow H_2 + 2M$$

The reaction mechanism can follow different routes for the production of H_2, however, the rate determining step (RDS) determines the value of the Tafel slope obtained from a η vs. *ln(j)* plot. Tafel slopes of 120, 40 and 30 mV dec^{-1} are reported for the Volmer, Heyrovsky and Tafel steps, respectively [16]. Since a larger Tafel slope means a lager increase in overpotential with current, it is desirable that the RDS are either the Heyrovsky or Tafel step. The RDS depends on the surface characteristics and it is potential dependent [15].

Figure 2.3 presents a comparison between the activity of metals towards HER and their M-H bond strength that gives insight into the expected RDS for different metals. Pt is the most active metal for the production of hydrogen; however, it is too expensive to be used as a cathode in industrial applications [9]. The high performance observed for Pt is a proof of the Sabatier's principle, which states that the adsorption energy should not be too low or too high for optimal catalytic performance [17].

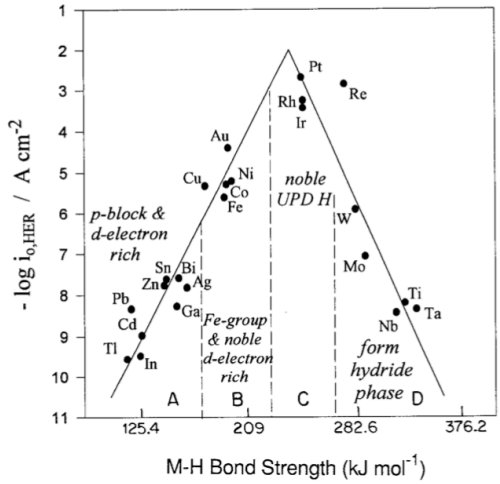

Figure 2.3. Comparison between M-H bond strength vs exchange current density for HER for different metals. Adapted from [18]. Higher exchange current density equals higher catalytic activity.

Metals that do not present the optimal energy for the formation of hydrides (M-H) have lower catalytic performance (see Fig. 2.3). The metals on the left side of the plot, like Ni and Fe, will most likely have the Volmer step as RDS due to their lower M-H bond energy. On the other hand, metals like Rh and Ir will most likely have desorption of H as RDS (Heyrovsky or Tafel) [19]. Quaino P *et al*. present additional factors influencing the catalytic performance, such as different crystalline structures and specific interaction with hydrogen atoms [17].

Transition metals like Ni and Fe are used as catalysts in different processes [20]. Their catalytic behavior comes from their ability to exist in different oxidation states allowing them to lend or withdraw electrons to the reacting molecules. This stabilization of the reaction intermediates presents a lower-energy alternative path for the reaction to occur, incrementing the number of successful interactions and therefore incrementing the reaction rate [21].

Many potential electrocatalysts for HER and OER are based on Ni due to its resistance to corrosion in alkaline conditions and availability on earth. Current research is also interested in bifunctional electrocatalyst, like NiFe or NiMo, for a higher performance while keeping the costs down [22].

2.6 Oxygen Evolution Reaction

The reaction happening at the anode is the oxygen evolution reaction (OER). This reaction is known as a two or four electron step, however, there is not consensus on the mechanism for this reaction [15]. Adzic *et al*. identified the superoxide anion (OO^-) as the intermediate in the oxygen reduction reaction (ORR) in alkaline medium [23]. Takanabe *et al*. assume that the mechanism for OER is the reverse of ORR and propose the following mechanism at a single active site [15]:

$$M + OH^- \leftrightarrow MOH + e^- \tag{2.23}$$

$$MOH + OH^- \leftrightarrow MO + H_2O + e^- \tag{2.24}$$

$$MO + OH^- \leftrightarrow MOOH + e^- \tag{2.25}$$

$$MOOH + OH^- \leftrightarrow MOO^- + H_2O \tag{2.26}$$

$$MOO^- \leftrightarrow M + O_2 + e^- \tag{2.27}$$

The theoretical value of Tafel slopes for each step of the reaction (Eq. 2.23 to Eq. 2.27) depends on the set of assumptions taken for modelling the kinetics of OER. Takanabe *et al*. proposed a model that considers the influence of potential on the reaction rate as well as the influence of intermediate coverage (θ) on the electrocatalyst surface [15].

Table 2.1. Theoretical Tafel slopes values for the reaction steps proposed by Takanabe *et al*. [15].

Rate determining step (RDS)	Tafel slope value with increasing current density (mV dec^{-}) Increasing current density→			
(2.23)	120			
(2.24)	30	120		
(2.25)	21	40	120	
(2.26)	22	30	60	120
(2.27)	22	40	120	

In a similar way to HER, a lower Tafel slope is desirable to limit the rapid increase of overpotential for OER. The specific RDS for OER is very hard to define since the reaction pathway is very sensitive to surface characteristics and may be time dependent. Additionally, the electrocatalytic surface is expected to be transformed since the reaction steps involve the formation and breakage of metal and oxygen species making it more difficult to define a clear mechanism for OER [19].

Since the metal-oxygen bond (M-O) is stronger than the oxygen bond (O-O), the OER always takes place on a metal oxide surface. As a result, the metal oxide employed as an electrocatalyst must be able to undergo redox transformation in solid state during the reaction [19]. Figure 2.4 compares the overpotential for OER with the transition enthalpy of lower to higher oxides, RuO_2 to RuO_3 for example. The comparison indicates that RuO_2 has the optimal transition enthalpy while metal oxides like NiO_X or Fe_3O_4, deviating from the optimal transition enthalpy, present a lower performance.

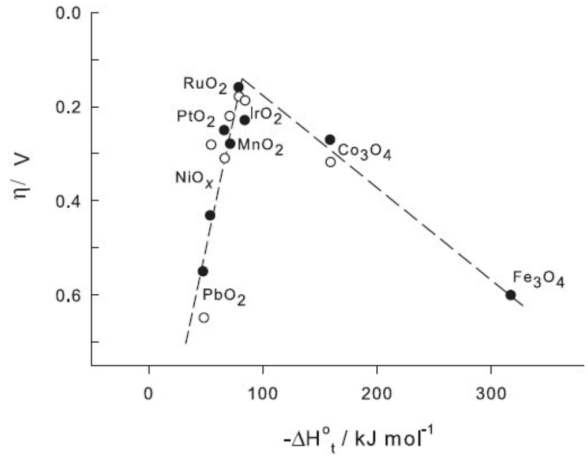

Figure 2.4. Comparison of transition enthalpy of lower to higher oxides vs overpotential for OER for different metal oxides. Adapted from [19].

Electrocatalysts containing noble metal oxides have been extensively researched, with oxides of Ru, Ir and Pd being the most active ones [24]. However, as it is the case for electrocatalysts for HER, the high prices of noble metals hinder their widespread use. Electrocatalysts containing nickel-based oxides represent the most promising option due to their high activity for OER and stability in an alkaline medium [5] and are much cheaper in comparison to noble metals.

There are different approaches to increase the activity of nickel-based electrocatalysts, such as making nickel alloys with other transition metals [5]. Li *et al*. reported that iron is the most promising metal to enhance the activity of nickel-based materials [25]. The addition of iron is believed to stabilize higher oxidation states of nickel facilitating the OER [26]. The nickel-iron stoichiometry can then be tuned to obtain an optimal electrocatalyst performance.

Manipulating the surface morphology is also a way to increase the performance. Surface structures that provide higher electroactive area exposed to the electrolyte can provide a higher activity. The roughness of the surface and hydrophilic behavior of it can also improve the performance by helping gas bubbles escape from the electrocatalyst surface. Just as atomic composition, surface morphology can be tuned for an optimal performance.

2.7 Electrocatalysts for alkaline water electrolysis: nickel-based materials

The overpotentials for HER and OER contribute to the voltage needed to drive the electrolysis of water in a cell. However, the overpotential for OER is higher due to the multi-electron transfer reaction for the production of oxygen. The more complex OER requires special attention for the selection of an appropriate electrocatalyst. The oxidative conditions at the anode are also a challenge for the electroactive materials

due to rapid degradation of the mechanical and chemical stability. In general, the electrocatalysts for AWE should have the following properties [4]:

1. highly active surface area with easy access to reactants and easy exit for gas products
2. high electrical conductivity
3. mechanical and chemical stability
4. low overpotential for HER and OER

Additional properties important for ZEF, and for the widespread application of AWE, are low cost and abundant materials. As mentioned before, nickel-based materials are especially promising due to their lower price compared with Ru or Ir, as well as their ability to catalyze both HER and OER. The relative easiness to synthesize nickel-based materials through electrodeposition or thermal treatment also lowers the cost of the electrodes. The ideal nickel-based material would mimic the performance of electrocatalysts containing noble-metals while keeping the costs low.

2.7.1 Electrodeposited materials: Raney nickel and NiFe

Electrodeposition is a commonly used method to synthesize electrocatalysts due to its low reaction temperature, tunability of film morphology, low cost equipment and crystallinity of the films deposited. It is usually used as a direct method of synthesis by providing a cathodic current to the substrate which is the base material of the electrode, and functions as support for the electrocatalytic film [27]. The simplest setup for electrodeposition includes a potentiostat, to control current or voltage, the substrate material, a counter electrode to close the circuit, and an electrochemical bath.

In an electrochemical bath containing Ni^{2+} ions in an acidic pH, the reactions happening at the cathode electrode are presented in Equations 2.28 and 2.29.

$$Ni^{2+} + 2e^- \leftrightarrow Ni_{(s)}\ (0.25\ V\ vs\ SHE) \tag{2.28}$$

$$2H^+ + 2e^- \leftrightarrow H_2 \tag{2.29}$$

On the anode side, at least one oxidation reaction is happening. Its nature depends also on pH and the voltage applied, in the case when the anode (counter electrode) is metallic nickel, the counter electrode is dissolved into water as described in Equation 2.30.

$$Ni_{(s)} \leftrightarrow Ni^{2+} + 2e^{-} \quad (2.30)$$

The process of electrodeposition at an atomic level can be described in four steps [27]:

1. the metal ion (M^{++}) approaches the substrate surface through diffusion, convection and migration processes
2. M^{++} loses its solvation shell
3. reduction by charge transfer forming a neutral adsorbed atom (M_{ads})
4. migration of M_{ads} to lower energy adsorption sites on the substrate (free defect sites) where nucleation takes place

The main factor affecting the characteristics of the deposited material is current density. Low current density results in a coarse deposited film since the creation of nucleation sites is slower than crystal growth. Higher currents increase the rate of nucleation (decreasing crystal size) resulting in a smoother surface. However; hydrogen evolution at high current densities can produce porous and discontinuous materials [27].

Two other important factors affecting the surface morphology are pH and temperature. Low pH values favor the HER [28]. Higher temperatures tend to increase the grain size due to enhanced ionic transport in the electrochemical bath [29]. The surface characteristics can be tuned by changing current density, pH, temperature and other factors such as bath composition or additives.

Raney nickel

One of the ways to increase the catalytic activity of nickel-based electrocatalysts is to increase the active area. Raney nickel is the "spongy" version of nickel, highly porous and with an increased surface area. Co-deposition of nickel alloys is one of the easiest ways to produce electrodes covered with a film of Raney nickel. The co-deposited metal, Zn or Al, is then leached in an alkaline medium leaving behind a porous and cracked structure (see Figure 2.5) [30].

Nickel electrodes with microporous structures are especially useful for water electrolysis as they allow removal of gas bubbles produced at the surface. Electro (co)deposition at high current densities produce the desired porous size as HER is favored. The bubbles of hydrogen produced block (temporarily) the deposition of nickel resulting in porous structures [31]. Herraiz-Cardona *et al*. reported a stable Raney-nickel electrode that decreases the voltage needed for AWE by 0.5 V compared to a smooth nickel electrode at a current density of 20 mA/cm^2 [32].

When Raney nickel electrodes are placed in an aqueous solution, they develop a layer of $Ni(OH)_2$ on top of the original NiO layer (Ni reacts with air). The hydroxide layers continue to grow across the anodic potential. Figure 2.6 shows the cyclic voltammogram for a nickel-based electrode, the anodic peaks correspond to the $Ni(OH)_2$/ NiOOH redox couple. It has been suggested that $Ni(OH)_2$ exists in two phases, resulting in two different phases of NiOOH as well [5].

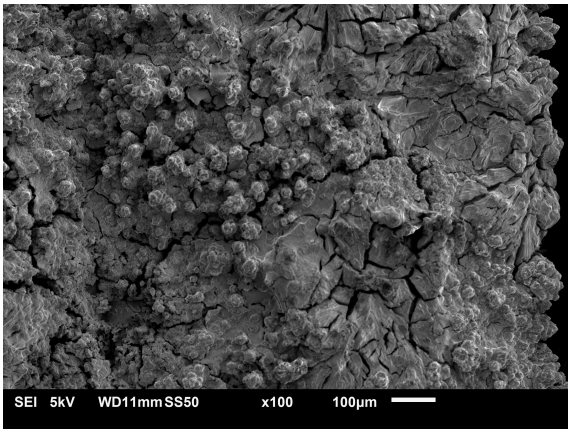

Figure 2.5. SEM picture of an aged Raney nickel electrode.

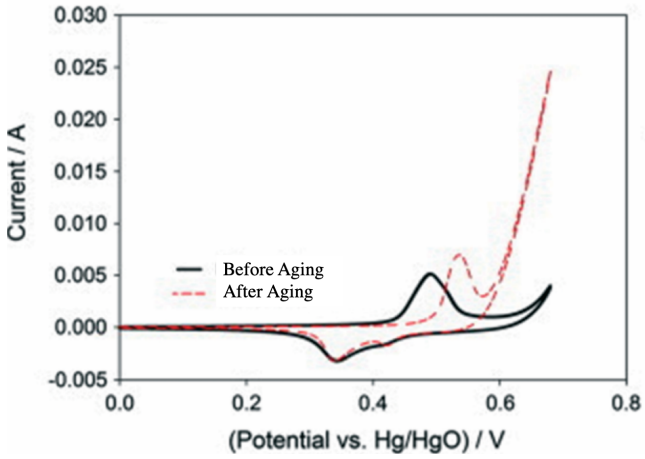

Figure 2.6. Cyclic voltammogram obtained for a nickel-based electrode before and after aging. Adapted from [5].

It is believed that β- $Ni(OH)_2$, more anhydrous and crystalline than α- $Ni(OH)_2$, is oxidized into β- NiOOH. This phase presents the optimal conditions for OER [33]. Nickel in β- NiOOH has a lower oxidation number compared to γ- NiOOH (resulting from α- $Ni(OH)_2$). The α phase of $Ni(OH)_2$ turns into the β phase upon cycling meaning that the activation of nickel-based electrodes is time dependent (see Figure 2.6). The β phases of the redox couple are believed to also increase the roughness factor, incrementing the active surface area [5].

NiFe

Doping nickel-based electrocatalysts with iron has been proved to increase the electroactivity in comparison to both pure metals [5]. The optimal atomic percentage of Fe mixed with Ni is different according to the source and synthesis method, and ranges from 10% to 50%, being 40% the most frequently reported [4, 34, 35]. Iron can be co-deposited with nickel taking advantage of the simple electrodeposition procedure, the composition of the electrochemical bath can be tuned to obtain the desired alloy.

Landon J. *et al*. detected, through X-ray spectroscopy, that the film composition changes with the atomic percentage of iron. The coexistence of $NiO/NiFe_2O_4$ phases was detected up to a 25% content of Fe.

A separated phase of Fe_2O_4 was detected at percentages above 25% indicating that Fe is not incorporated into the NiO lattice. The $NiFe_2O_4$ phase is believed to be the reason behind the increased catalytic performance as an increment in coordination of Fe atoms during OER was detected [34].

Louie M. *et al*. reported that the addition of iron to a nickel electrocatalyst shifts the potential of the $Ni(OH)_2$/ NiOOH redox couple. Iron suppresses the oxidation of the nickel couple and causes the number of electrons transferred during the reaction to decrease, decreasing the average oxidation number of Ni (see Figure 2.7). Figure 2.7 does not present a peak related to a Fe redox couple since Fe(II)/Fe(III) transition happens at potentials between -0.5V and -1.2V vs Hg/HgO [35].

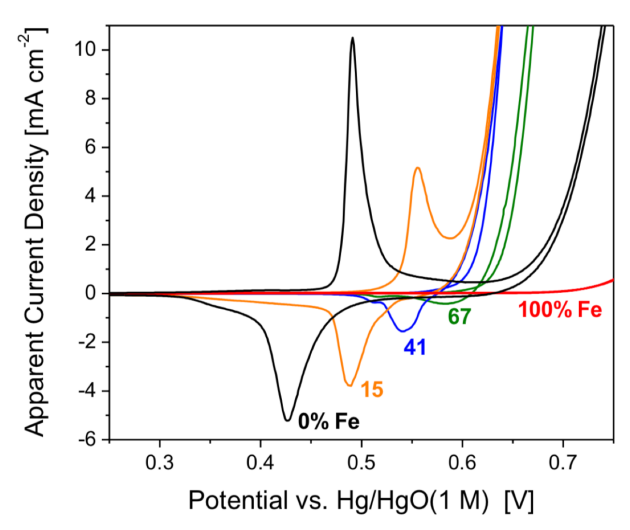

Figure 2.7. Effect of Fe on the $Ni(OH)_2$/ NiOOH redox couple in 0.1 M KOH. The addition of Fe up to 41% content increases the performance of the nickel-based electrocatalyst Adapted from [35]

Louie M. *et al*. propose that adding Fe to Ni has a similar effect as the activation of nickel films by aging (see Figure 2.6). According to Raman spectroscopy, the addition of Fe to Ni results in a structure similar to β- NiOOH albeit less crystalline. Iron not only changes the average oxidation number of nickel but also changes its local environment [35].

2.7.2 Hydrothermal treatment electrode: NiFe-LDH

NiFe-LDH (layered double hydroxide), have sparked great interest due to its electrocatalytic activity for water electrolysis, low cost, simple preparation method and abundant starting materials [36]. NiFe-LDH can be used directly as electrocatalysts or support material to synthesize different catalysts due to its interesting nanostructure and large surface area [37].

NiFe-LDH materials have the structure presented in Figure 2.8. The structure consists in sheets of edge-shared nickel oxide octahedra with iron substituting nickel atoms. The amount of substitution depends on the composition. Ni^{2+} or Fe^{3+} are surrounded by six hydroxides. The excess positive charge introduced

by Fe^{3+} (when substituting Ni^{2+}) is balanced by interlayer anions [38]. Figure 2.9 shows the nanostructured sheets present in NiFe-LDH.

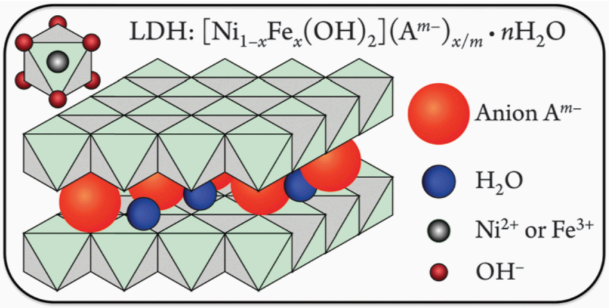

Figure 2.8. Schematic representation of NiFe-LDH structure. Adapted from [38].

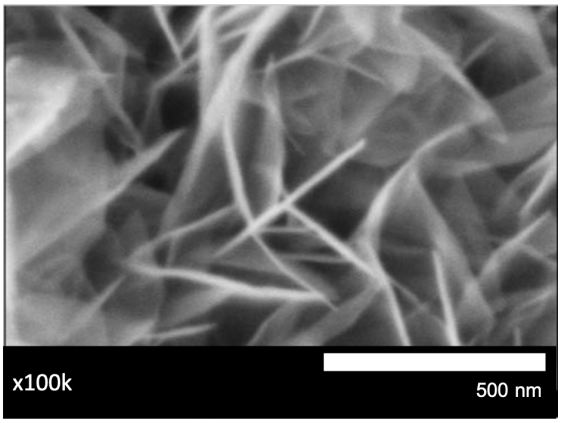

Figure 2.9. SEM image of NiFe-LDH. The nanostructured sheets of nickel and iron are visible. Taken from: [36]

One of the most common methods of NiFe-LDH synthesis is the co-precipitation of nickel and iron hydroxides. This can be achieved when heating a solution containing Ni^{2+} and Fe^{3+} ions and urea. The hydrolysis of urea produces carbonate and hydroxide ions [39]. The carbonate ion takes part as the interlayer anion in the LDH structure.

Just as in electrodeposited NiFe electrocatalysts, the interaction between nickel and iron during HER or OER is still not completely clear. Rui Li *et al*. suggest that the LDH enhances the transformation from $Ni(OH)_2$ to NiOOH increasing the activity for OER [40]. However, B. Hunter *et al*. reported that an increased content of Fe at the edges of the LDH structures increases activity indicating that Fe sites are active for OER [38].

3

Methodology

An electrolysis cell was designed and built to mimic the geometry and cell concept of the alkaline electrolyser designed by ZEF. Additionally, three electrode materials were synthesized to investigate alternatives to highly efficient noble-metal electrodes for alkaline electrolysis. This chapter begins with a description of the general experimental setup in section 3.1. Section 3.2 discusses the safety considerations. Section 3.3 further describes the zero-gap concept of the cell. In section 3.4, an explanation on how the different voltages of the cell were measured is given. Section 3.5 gives a description of the electrochemical tests performed on the electrodes while section 3.6 mentions the electrode surface characterization techniques. Finally, section 3.7 gives an overview on how the electrodes were synthesized.

3.1 General electrolysis setup

The general electrolysis setup consisted of a zero-gap alkaline electrolysis cell connected to a system that controlled a flow of N_2 to safely dilute and purge the produced H_2/O_2 mixtures out of the cell. In addition to serve as a safety measure, N_2 was also utilized to pressurize the cell to carry out tests at different pressures. The setup included a 5A Ivium potentiostat for the electrochemical tests and a temperature sensor to register the external temperature of the cell. 30% wt. KOH was used as electrolyte and the experiments were self-heated (temperature was not controlled).

The system to control the flow of N_2 included a manual valve and pressure regulating valve at the exit of the N_2 tank to initiate the gas flow. A Bronkhorst mass controller, calibrated for N_2 and rated for a pressure of 100 bar, secured the correct flow of N_2. A manometer located before the cell was used to read the pressure inside the cell. At the exit of the cell, a pressure relief valve was utilized as a back-pressure regulator to set the experimental conditions in a range of 1 – 5 bar (absolute). An additional manual valve was added at the exit of the cell for the recharging of the electrolyte. Figure 3.1 illustrates the general characteristics of the setup.

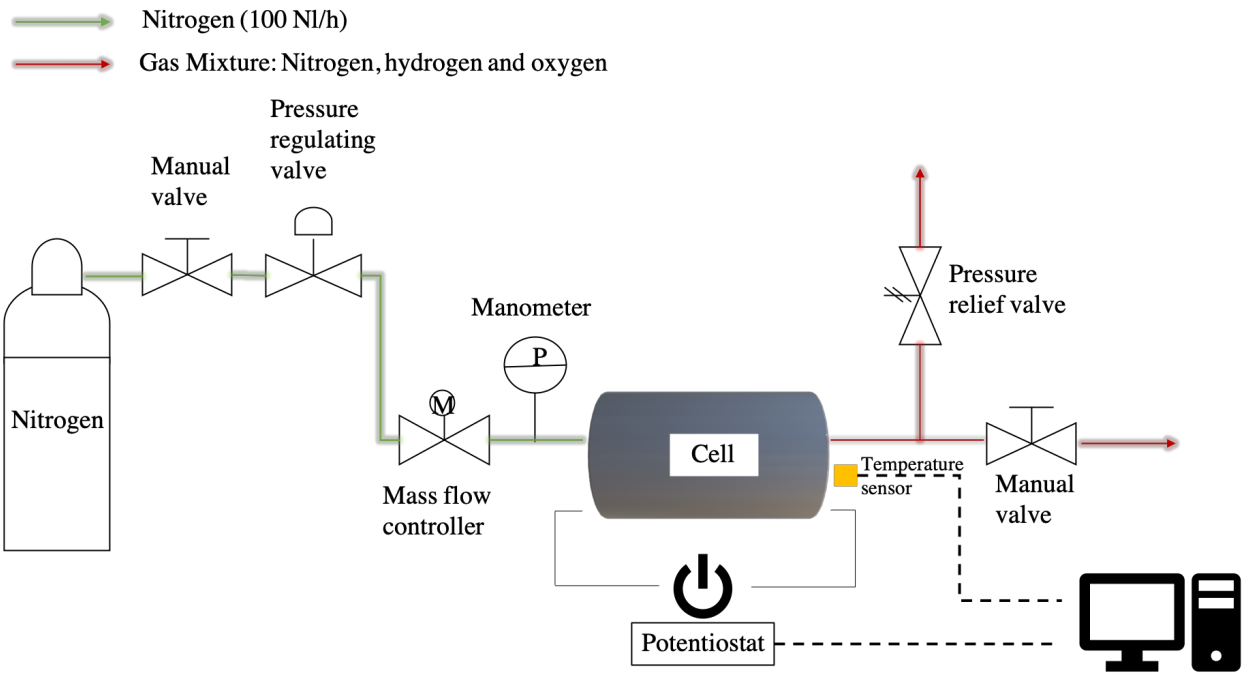

Figure 3.1 General zero-gap alkaline electrolysis setup. Self-heating setup with 30% wt. KOH as electrolyte. An H_2 detector was located inside the fume hood at the vicinity of the setup. The temperature sensor consisted of a negative temperature coefficient thermistor (NTC).

3.2 Safety considerations

As mentioned in the previous section, N_2 was used to safely dilute the H_2/O_2 mixture. The flow of N_2 was determined by calculating the theoretical production of H_2/O_2 at the maximum electrical current employed during the experiments to ensure safety throughout the tests. The production of H_2 and O_2 at 5 A is as follows (100% faradic efficiency):

H_2: 0.093 mol/h

O_2: 0.046 mol/h

The amount of H_2 and O_2 produced is low considering that the maximum current will be reached only intermittently. However, the closed geometry of the electrolysis cell (see Figures 3.3 and 3.4) required the gas products to be diluted and purged. The expected maximum temperature during experiments was calculated to be 103 ºC (see Appendix A). Figure 3.2 indicates that the lower flammability limit (LFL) for H_2 at this temperature is 3.5% in a tertiary system of $N_2/H_2/O_2$ at similar composition as air [41].

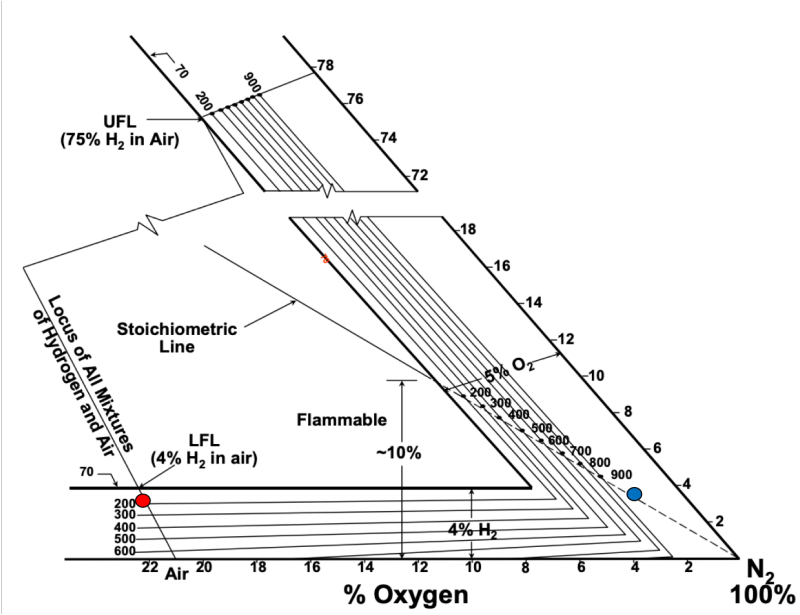

Figure 3.2 Tertiary diagram for H_2, O_2 and N_2 at elevated temperatures [41]. The red dot represents the LFL for H_2 in air, the blue dot represents the same concentration of H_2 (3.5%) at the conditions inside the cell. 103 ºC equals 217 ºF.

The production of H_2 and O_2 is stoichiometric (H_2 +1/2 O_2), as a result, keeping the concentration of H_2 below 3.5% and the concentration of the O_2 below 1.75% allows for the safe management of the gases inside the electrolysis cell and at the gas exit. Figure 3.2 illustrates the composition of gas mixtures containing 3.5% of H_2 inside the cell (blue dot) and at the exit of cell (red dot) when the mixture enters in contact with air. The N_2 flow selected for the operation of the electrolyser is equivalent to 3.74 mol/h of N_2. This flow rate results in the following percentage of gases in the mixture:

N_2: 96.4%

H_2: 2.4%

O_2: 1.2%

The percentage of H_2 provided a safe operation of the experiments and gave room for slight fluctuations of N_2 flow. However, no fluctuations were detected during the experiments. Table 3.1 presents the volumetric flow of N_2, H_2 and O_2 in normal liters (Nl). In addition to the control of N_2 flow with the mass-flow controller, a H_2 detector was located inside the fume hood at the proximity of the setup. The hydrogen detector manufactured by Crowcon had a pre-set alarm at 30% of the LFL, 1.4% of H_2 in air at 20ºC.

Table 3.1. Volumetric flow of N_2 and gas products in the alkaline electrolysis setup.

Gas	Volumetric flow (Nl/h)
N_2	100
H_2	2.24
O_2	1.12

The volumetric flow of H_2 and O_2 correspond to a current of 5 A and 100% faradic efficiency.

3.3 Alkaline electrolysis cell construction: zero-gap concept

The experimental setup utilized in this work was based on an alkaline electrolyser prototype envisioned and built by ZEF. The electrolysis cell here presented is an adaptation of said prototype, and the figures and schematic representations are a simplification to explain the basic concept of the electrolyser.

The construction of the setup started with the 3D design. The design was done with the software Fusion 360 and had the following requirements:

- Maintain as much as possible the geometry of the full electrolyser prototyped by ZEF
- Ensure a modular construction practical for experimentation
- Guarantee the leak-tightness of the setup for an absolute pressure of 5 bars
- Facilitate the construction of the cell segments by 3D milling

The construction process was iterative and the base material for the setup was C-PVC. Leak-tightness and functionality for experimentation were the main challenges. To solve these problems, a series of cells were milled and tested resulting in the following modifications:

- Betterment of the alignment of the manufactured segments in the 3D milling machine
- Modification of O-ring grooves deepness
- Length limitation of protruding elements with thickness less than 1 mm

The resulting electrolysis cell is shown in Figures 3.3 and 3.4. Each figure represents one compartment of the cell, anode or cathode. The frontal part of the compartments is a mirrored image of the other and are closed together to create the zero-gap arrangement of the cell. The exact measurements are not presented in this document due to confidentiality reasons. It can be mentioned that the geometric area of the electrodes is 30 cm^2 and that the electrolyte chamber has a volume of 75 mL.

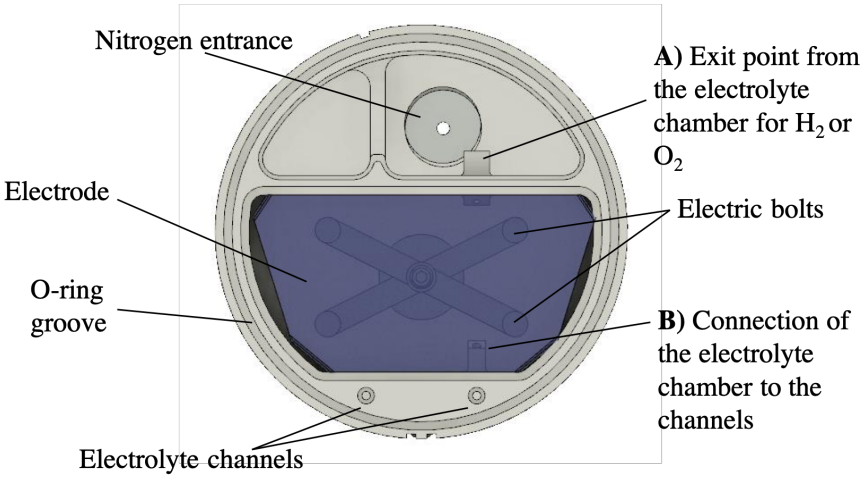

Figure 3.3. Front view of one side of the alkaline electrolysis cell.

The space created on top of the electrolyte and electrode chamber allowed the flow of N_2. Feature **A** in Figure 3.3 is a vertical channel connecting the electrolyte to the open space, in this manner, H_2 or O_2 can exit the chamber and be carried away by the N_2 flow. Feature **B** is a vertical channel connecting (through the electrolyte channels) the electrolyte chamber to the chamber in the other compartment to secure the same level of electrolyte. The interconnected electrolyte also permits a single electrolyte charging point (see Figure 3.4).

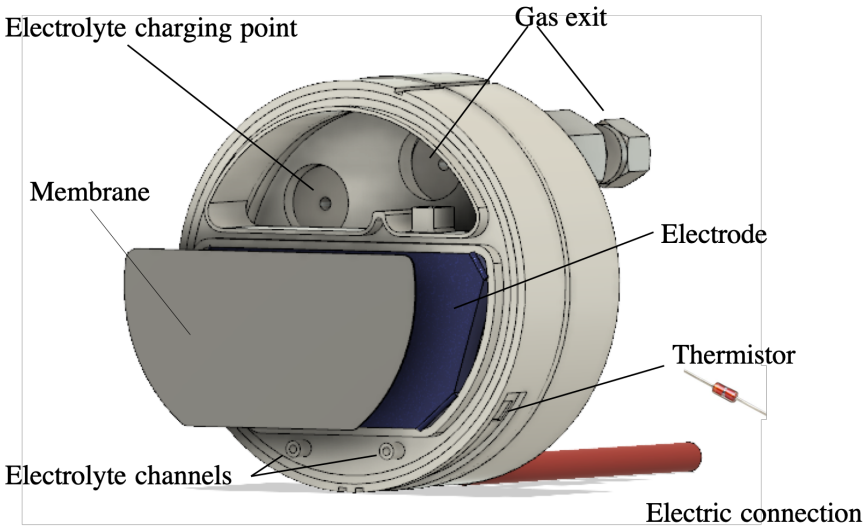

Figure 3.4. Three-dimensional view of one side of the alkaline electrolysis cell.

Figure 3.4 presents additional features for the connection and operation of the cell. The membrane, Agfa Zirfon Perl, is a separator membrane employed in AWE [42]. The Thermistor groove allows the temperature sensor to be placed closer to the electrolyte chamber. The temperature was recorded with an Arduino Mega microcontroller and a computer.

The gas exit, electrolyte charging port, as well as the N_2 entrance, consist of custom-made stainless-steel connectors compatible with Swagelok accessories. The connections to the other parts of the setup were done with 6 mm plastic tubing. The electrical connection was achieved through the external part of the stainless-steel structure supporting the electric bolts (see Figure 3.5 **A**).

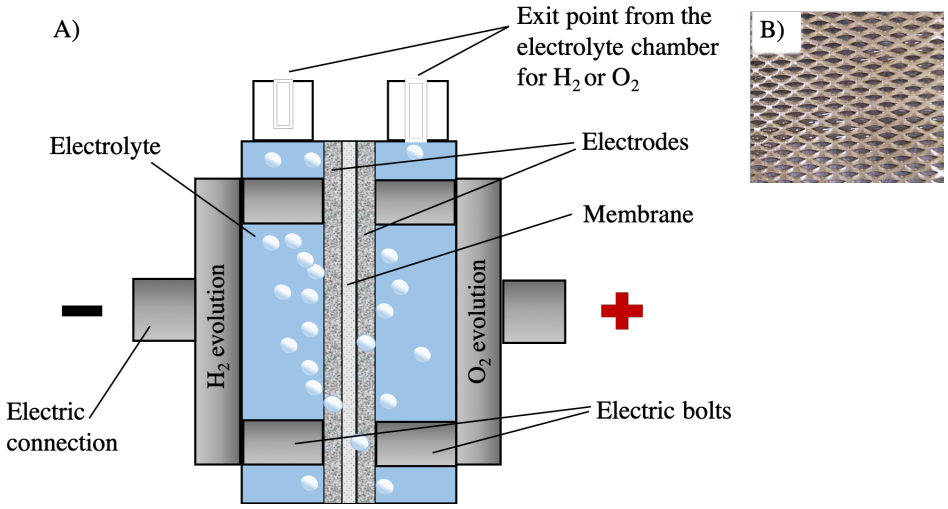

Figure 3.5. A) Illustration of the zero-gap alkaline electrolysis cell side view. B) Nickel mesh as electrode substrate

The zero-gap configuration obtained when closing both compartments together is illustrated in Figure 3.5 **A**. The cathode (-) and anode (+) are pressed together with the membrane in between, the movement of bubbles produced at the front of the electrodes is possible due to their mesh structure (Figure 3.5 **B**). The clearer view of the exit points for H_2 and O_2 in Figure 3.5 **A** shows that the gas bubbles need to rise and be directed to the exit channel in order to leave the electrolyte chamber.

Table 3.2 presents a summary of the experimental conditions at the electrolysis cell.

Table 3.2. Summary of experimental conditions at the electrolysis cell.

Design	Zero-gap
Operating pressure (bar)	1-5
Electrode geometric area (cm^2)	30
Operating temperature (ºC)	Self-heating
Electrolyte concentration	30% wt. KOH
Electrolyte volume (mL)	75
Operating current (A)[1]	5
Membrane material	ZirfonPerl UTP 500
Cell material	C-PVC

[1]Maximum current utilized during experiments

3.4 Potential differences measurements and electrical connections

Figure 3.6 A depicts the side view of one of the cell compartments including a Pt wire used as a pseudo-reference electrode. The pseudo-reference electrode was utilized to measure the overpotential at each side of the cell. Figure 3.6 B presents the different voltages measured during the experiments:

- V 1: Potential difference of the whole cell
- V 2: Potential difference between the pseudo-reference electrodes
- V 3: Anode overpotential
- V 4: Cathode overpotential

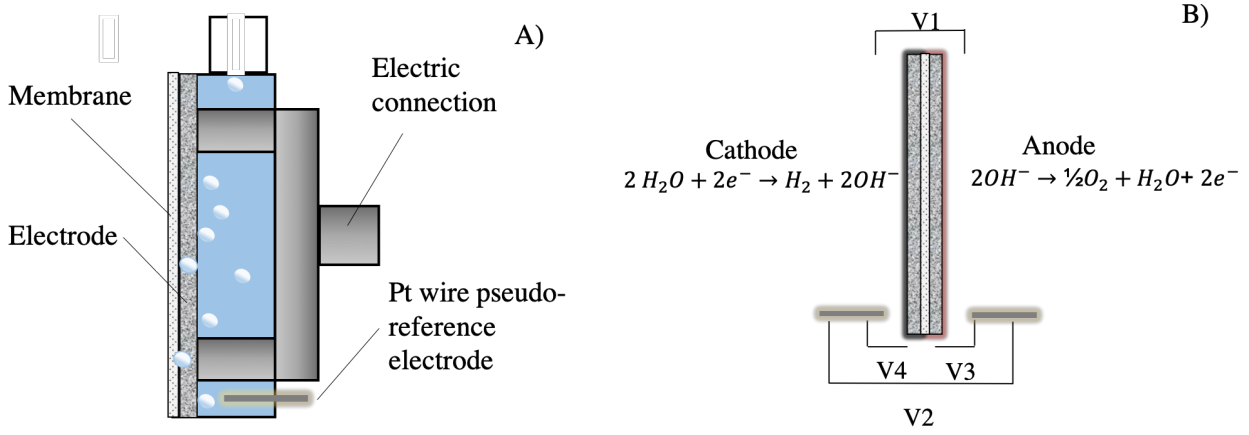

Figure 3.6. A) Illustration of a single-cell compartment with a Pt wire pseudo-reference electrode. B) Schematic representation of potentials measured during the experiments.

The sum of voltages 2,3 and 4 equals voltage 1. The reason for this is that the chemical reaction happening during the measurement of V2 corresponds to the formation of water. This also means that V3 and V4

indicate the kinetic overpotentials for anode and cathode, respectively. Equation 3.1 corresponds to the reaction taking place at the anode's pseudo-reference electrode. Equation 3.2 corresponds to the reaction taking place at the cathode's pseudo-reference electrode, and together with Eq. 3.1 results in the formation of water (Eq. 3.3).

$$\frac{1}{2}\,O_2 + H_2O + 2e^- \rightarrow 2OH^- \tag{3.1}$$

$$H_2 + 2OH^- \rightarrow 2H_2O + 2e^- \tag{3.2}$$

$$H_2 + \frac{1}{2}O_2 \rightarrow H_2O \tag{3.3}$$

The use of Pt wire as a pseudo-reference electrode instead of a conventional one was decided due to its advantages related to the experimental setup. The small diameter of the Pt wire (0.25 mm) avoids disrupting the geometry of the cell, and it also allows easier sealing of the setup for operation at different pressures. However, the use of a pseudo-reference means that the voltage measured depends on the conditions at the electrolyte [43]. The undefined concentrations of H_2, O_2 and OH^- at the pseudo-reference electrodes surfaces limit the comparability of the results obtained with V3 and V4 measurements.

The electrical current for the experiments was provided with a 5A IviumStat potentiostat, which was connected to the stainless-steel electric connections of the cell. The working electrode was connected to the cathode and the counter electrode was connected to the anode to carry the current. The reference and sensing electrodes were connected to the anode and cathode, respectively, to carry the voltage signal to the potentiostat. These electrodes were connected to a Peripheral Differential Amplifier (PDA) to measure the additional potential differences presented in figure 3.6 B. Figure 3.7 presents the electrical connections at the PDA to measure voltages 1 to 4 which correspond to channels 1 to 4.

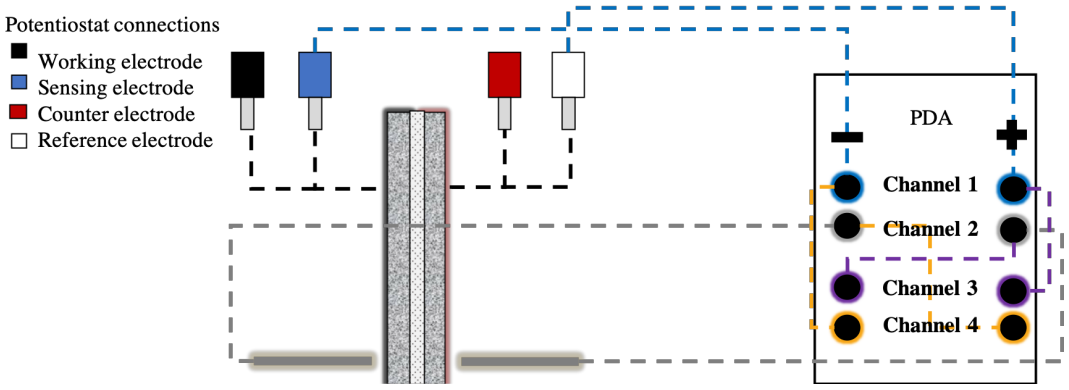

Figure 3.7. Electrical connections between the cell, PDA and potentiostat. Channel 1 corresponds to the whole cell voltage, channel 2 corresponds to the potential difference between both reference electrodes, and channel 3 and 4 correspond to the kinetic overpotentials at the anode and cathode respectively.

3.5 Electrode performance: electrochemical tests

The electrochemical characterization of the different electrodes had the objective to evaluate the performance and stability of each sample. The electrodes were analyzed (in order) with 1) cyclic voltammetry, 2) double layer capacitance test, 3) cyclic galvanometry and 4) stability test. After test 4, the samples were analyzed again with tests 1 and 2. In all the tests, unless stated otherwise, the anode and cathode consisted of the same electrode material evaluated. 30% wt. KOH was used as electrolyte in all the tests. The electrical connection employed in these tests is illustrated in Figures 3.6 B and 3.7.

The following list presents the details of the electrochemical tests performed:

1) Cyclic voltammetry

Cycles with a scanning rate of 50 mV/s in a range of -1.23 to 1.23 V were carried out to characterize the anodic and cathodic peaks corresponding to the chemical species at the electrode surface. The comparison of the charge associated to the chemical transformation (peak area) permits a relative comparison of electroactive surface area among the electrode materials [44]. The voltage range in this experiment refers to V1 (voltage for the whole cell). The reported cyclic voltammograms in the results section corresponds to the fifth cycle.

2) Double layer capacitance test

In order to measure the double layer charging or capacitive behavior of the different electrode materials, cyclic voltammetry in a non-faradic voltage range was performed on every electrode. The cyclic voltammetry was carried out at eight different scanning rates: 0.005, 0.01, 0.025, 0.05, 0.1, 0.4, and 0.8 V/s. The working electrode was held at each potential vertex for 10 s before continuing the sweep. Afterwards, the capacitive current at the middle point of the voltage range was plotted against the scanning rate to obtain a straight line with a slope equal to the double layer capacitance. The same procedure was presented by McCrory *et al*. [45].

Capacitive current (i_c) is related to scanning rate (s) and double-layer capacitance (C_{DL}) according to equation 3.4.

$$i_c = sC_{DL} \tag{3.4}$$

3) Cyclic galvanometry

Cycles with a scanning rate of 50 mA/s in a range of 0 to 5A were carried out to obtain the electrochemical parameters describing the electrode performance: exchange current density and Tafel slope. The tests

consisted of 5 cycles to make sure that the results were reproducible and that the values obtained correspond to activity towards water electrolysis and no initial changes in the electroactive surface. The reported results correspond to the fifth cycle in a backward direction (from 5 to 0 A). The results were corrected by subtracting the ohmic losses due to electrical connections (0.0163 Ω per cell side).

4) Stability tests

In order to evaluate the stability of the different electrode materials, on/off cycles with a current of 5 A where carried out. The cycles were composed of 75s at 5A and 25s at 0A, the number of cycles was 90 (2h and 30 minutes). The results were corrected by subtracting the ohmic losses due to electrical connections (0.0163 Ω per cell side).

3.6 Electrode surface characterization: SEM, EDS and XPS analysis

Scanning electron Microscopy (SEM) images were obtained at different magnifications using JEOL JSM 6010LA (JEOL, Tokyo, Japan). The same equipment was utilized for Energy-dispersive X-ray spectroscopy (EDS) elemental analysis. The SEM images and EDS analyses were obtained after the aspiration of loose particles on the electrode samples. No other pre-treatment was applied to the samples. The detector parameters for SEM and EDS were SEI 5kV and BEC 20 kV, respectively.

X–Ray Photoelectron Spectroscopy (XPS) of fresh and spent electrodes were obtained with a ThermoFisher K-Alpha Photoelectron Spectrometer. The analysis results correspond to the measurement taken after etching the samples two times.

The surface characterization analyses were carried out before and after the electrochemical tests. The sample sizes for all the analyses were 2 x 1 cm.

3.7 Electrode Synthesis

Five electrode materials were tested during the experiments. A commercial sample of a nickel-based electrode was obtained from Permascand as well as bare nickel mesh (long-way of diamond hole: 4 mm; short-way: 2 mm; thickness: 1 mm). In addition to these two materials, three electrode materials were synthesized: Raney Nickel (RNi) and NiFe (nickel-iron) through electrodeposition and NiFe-LDH (layered double hydroxide) through hydrothermal treatment.

Expanded nickel mesh (long-way of diamond hole: 4 mm; short-way: 2 mm; thickness: 1 mm) with a geometric area of 30 cm^2 was employed as the substrate for the three different electrode coatings. The pretreatment steps of the substrates before electrodeposition or hydrothermal treatment are presented below:

1. Sandblasting to create a coarser surface for better adherence of the material
2. Degreasing with 25% wt. NaOH (1 min) and 18% wt. HCl (1 min) at 90ºC
3. Rinsing with deionized water
4. Drying under pressurized air
5. Pretreating cathodically at -27 mA/cm^2 in a nickel solution (240 g/L $NiCl_2$ and 120 mL/L HCl) for 5 minutes. This step was not realized for the NiFe-LDH electrode.

3.7.1 Electrodeposited electrodes: Raney Nickel and NiFe

The RNi and NiFe electrodes were prepared through simple electrodeposition. This procedure consisted of applying a cathodic current to the pretreated substrate inside an electrochemical bath containing the chemical species to be deposited on the substrate surface. The 5A Ivium potentiostat was also used for this procedure. The experimental setup for electrodeposition is illustrated in Figure 3.8.

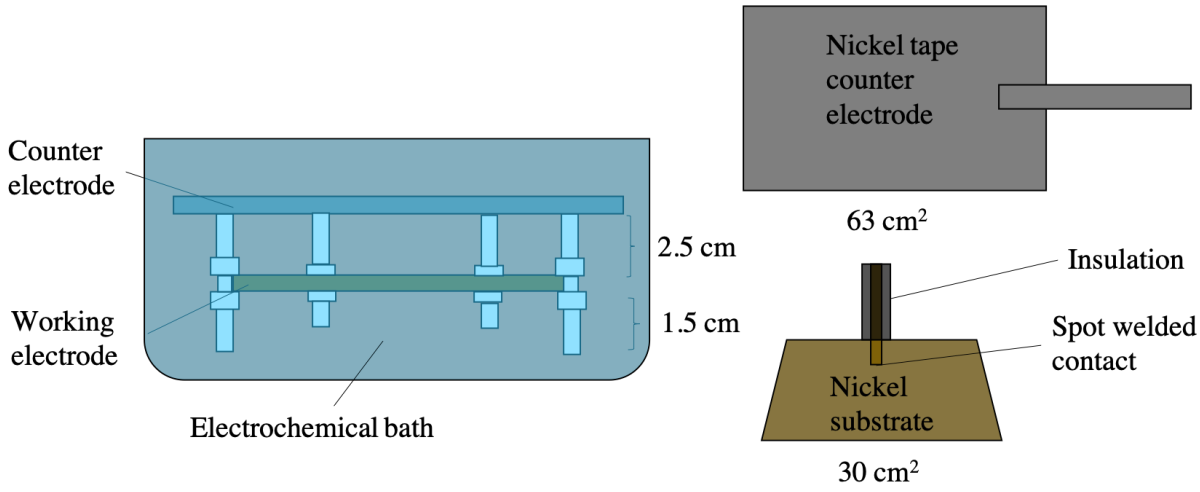

Figure 3.8. Simplified representation of electrodeposition setup.

Table 3.3 presents a summary of the bath composition and conditions used for the electrodeposition of the electrodes. The baths were prepared with deionized water and all the chemicals used were of reagent grade (≥ 95%) and purchased from Alfa Aesar. These experimental conditions were presented by Herraiz-Cardona *et al*. and McCory *et al*. [32, 46].

Table 3.3. Conditions for electrodeposition.

Electrode	Bath composition	(g/L)	Experimental Conditions	
RNi[1]	$NiSO_4 \cdot 6H_2O$	330	Temperature (°C)	25
	$NiCl_2.6H_2O$	45	j (mA/cm^2)	166
	H_3BO_3	37	Time (min)	60
	$ZnCl_2$	20	pH	4.5
NiFe[2]	$NiSO_4 \cdot 6H_2O$	2.40	Temperature (°C)	25
	$FeSO_4 \cdot 7H_2O$	2.50	j (mA/cm^2)	50
	$(NH_4)SO_4$	2.92	Time (s)	50
			pH	2.5

Adapted from Herraiz-Cardona *et al*.[1] and McCrory *et al*.[2] [32, 46].

After the electrodeposition procedure, the samples were left to dry inside a fume hood for 24 h and no additional treatment was done for the NiFe electrode. In the case of RNi, further activation was needed to increase the porosity of the material. The activation procedure consisted of Zn leaching from the electrode surface with concentrated KOH according to Equation 3.5. This procedure leaves a porous structure behind. Herraiz-Cardona *et al*. used a concentration of 6M for 24 h which resulted in the destruction of the RNi sample.

$$Zn + 2KOH + 2H_2O \rightarrow K_2[Zn(OH)_4] + H_2 \quad (3.5)$$

Additional activation experiments with different and lower KOH concentration were carried out. KOH 1M during 24 h resulted in an activated sample that held its mechanical stability and adherence to the substrate. After the activation, the RNi electrodes were placed inside a flask containing 30 % wt. (6.90 M) KOH at 50 ºC for 1 h to test their stability at similar conditions occurring during the electrochemical tests. Figure 3.9 presents the SEM images comparison of the activated samples with 6 and 1 M KOH, the sample activated with 1 M presented better adherence to the substrate, less visible cracks and maintained the protruding structures.

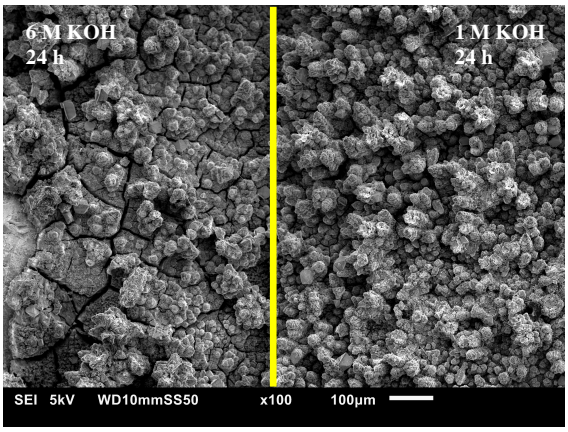

Figure 3.9. SEM analysis of samples activated with 6 and 1 M KOH.

3.7.2 Hydrothermal synthesis: NiFe-LDH

The NiFe-LDH samples were deposited on nickel mesh substrates via simple hydrothermal synthesis. After pretreatment, the substrates were located against the walls of an autoclave. 100 mL of a bath containing 0.40 g of $Ni(NO_3)_26H_2O$, 0.56 g of $Fe(NO_3)_39\ H_2O$, and 0.83 g of urea was poured inside the autoclave. The samples were taken to a temperature of 120 ºC and maintained at that temperature for 12 hours. The autoclave was then allowed to cool naturally to room temperature, and the samples were dried with pressurized air. A similar procedure was reported by J. Luo *et al*. [47].

4

Results

This chapter aims to answer the research questions looking to find an alternative to noble-metal electrodes for alkaline electrolysis and to elucidate the effect of high-pressure operation on a zero-gap alkaline electrolyser. Section 4.1 starts with the surface and electroactive characteristics of the materials. Section 4.2 presents the performance results at atmospheric conditions while section 4.3 assesses the stability of the materials. Section 4.4 presents the changes in surface and electroactive characteristics of the materials after the stability tests. Section 4.5 investigates the effect of pressure on cell voltage and 4.6 closes with a summary of performance considerations and a simple cost comparison of the materials.

4.1 Initial electrode characterization: SEM, EDS, XPS and cyclic voltammetry

SEM (scanning electron microscope), Energy-dispersive X-Ray Spectroscopy (EDS) and X-Ray Photoelectrons Spectroscopy (XPS) were used on the fresh electrodes to observe the morphology and composition of the initial material. As initial electrochemical tests, cyclic voltammetry in different voltage ranges and scan rates was used to compare the electroactive surface area. Surface composition and area, and electroactive interactions with the electrolyte help to understand the observed performance for the different electrode materials. Appendix G presents pictures of the synthesized electrodes.

4.1.1 Electrode surface morphology and elemental composition: SEM, EDS and XPS

Figure 4.1 presents the SEM images of the fresh electrodes tested in this project as well as for the commercial Permascand electrode. The images have a magnification of x100 and x500 (left and right, respectively). The images seek to compare qualitatively the surface morphology for the different materials. A rougher and/or more porous surface is related to higher electroactive surface area.

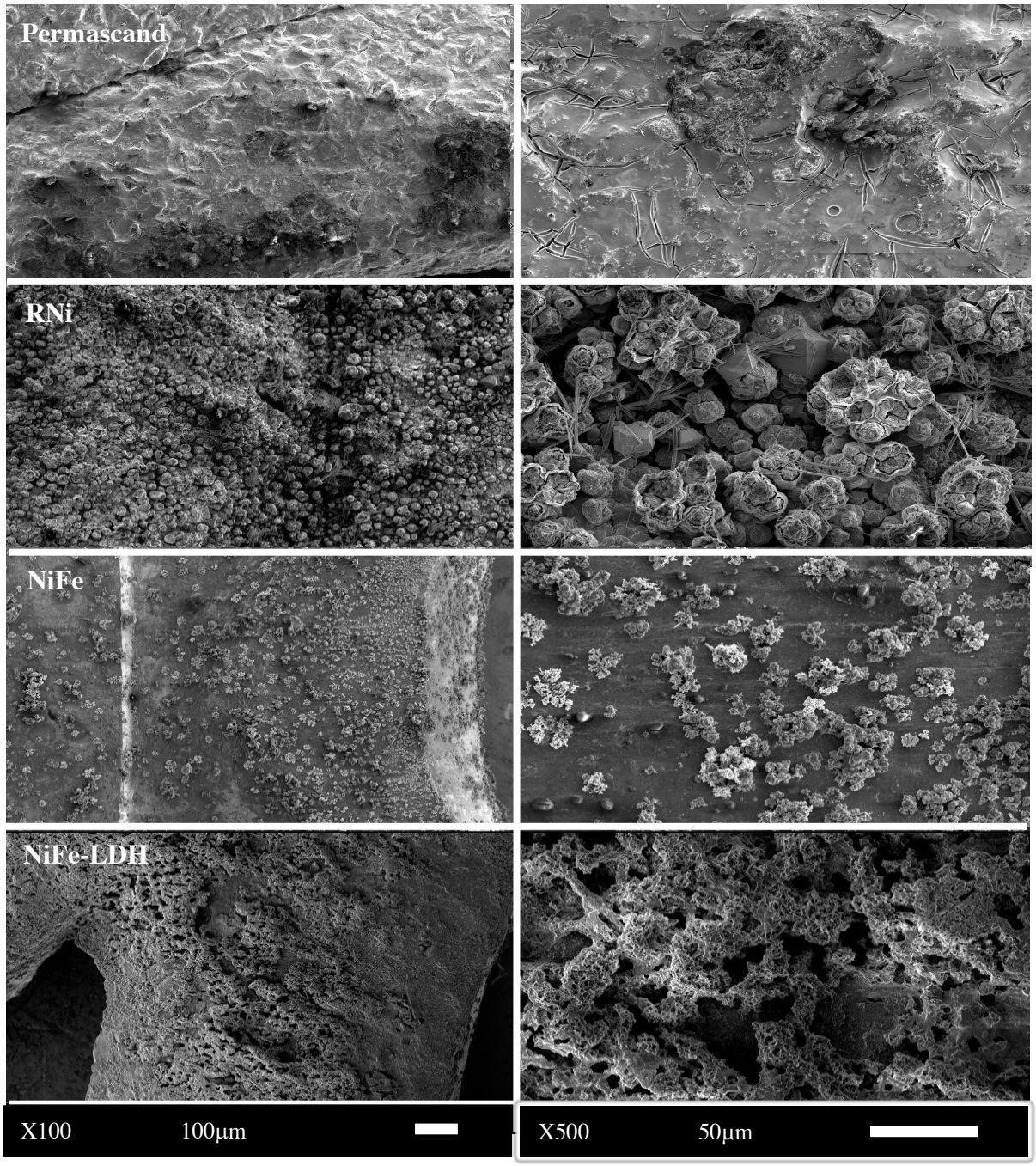

Figure 4.1. SEM pictures for the fresh electrodes at different magnifications. From left to right: x100 and x500. Detector parameters: SEI 5kV.

The Permascand images show a grainy smoothed surface without surface structures. The only distinguishable features are cracks and darker spots, identified by EDS analysis as nickel chloride.

The Raney nickel (RNi) images show a grainy and fractal-like structure. The tip of the protruding structures presents channels and porous structures. The angular and needle-shaped crystals observed in the sample correspond to a Zn salt, most probably $K_2[Zn(OH)_4]$.

The Nickel-iron (NiFe) images show a splattered coverage of the substrate due to the low electrodeposition time. The clusters of material deposited present two different appearance: smooth and dendritic. The smooth material consists mainly of nickel-iron hydroxides and the dendritic material has a higher content of metallic nickel-iron [48]. The higher ratio metals/oxygen of the dendritic structures gives them their brighter appearance. Species with higher atomic number emit backscattered electrons more strongly during the SEM analysis appearing brighter [49].

The NiFe-LDH (layered double hydroxides) images show a non-homogenous porous structure supported on the substrate. In 2018, Alobaid also reported the characteristic flake-like structures of layered double hydrides obtained through hydrothermal synthesis [36]. The reported porous structures with dimensions in the nanoscale were not observed in this sample with the microscope utilized. The qualitative analysis of the SEM images hints that NiFe-LDH and RNi electrodes are the materials with the highest surface area.

Table 4.1 presents the elemental analysis for the fresh electrodes. EDS and XPS were utilized to obtain the elemental composition of the samples. EDS and XPS give information at different deepness of the surface. EDS provides composition of the bulk of the material in the range of μm [50], while XPS gives information at approximately 5nm in depth [51]. XPS information is more relevant as it characterizes the atomic layers that participate in the electrolysis reaction. The relatively high nickel content obtained with EDS analysis in NiFe-LDH, NiFe and RNi is possibly due to the electron beam reaching the nickel substrate during the analysis. The observations for each material refer to the surface composition (XPS results).

Table 4.1 Elemental analysis for as-synthesized electrodes.

	Atomic content (%)	
	EDS	**XPS**
Permascand		
O	71.58	60.91
Al	0.96	1.24
Ni	8.39	11.07
Ru	19.05	20.34
Cl	-	4.08
Si	-	2.34
Raney Nickel (RNi)		
O	54.45	64.31
Ni	32.90	5.73
Zn	12.63	26.10
Si	-	3.84
NiFe		
O	55.49	68.53
Ni	40.67	10.52
Fe	3.78	20.94
NiFe-LDH		
O	63.95	60.72
Ni	33.55	17.84
Fe	2.48	9.58
Si	-	11.82

The XPS results for Permascand show that the deposited layer consists of oxidized species of ruthenium and nickel. The surface is mainly composed of ruthenium species, the Ru/Ni ratio is 2. The low content of Al and Si may indicate they are present on the surface only as contaminants. The comparison of EDS and XPS results indicate that the bulk of the deposited material has the same composition as the surface.

The results obtained for RNi indicate that the surface consists mainly of oxidized zinc, the Zn/Ni ratio is 4.5. This implies that after the leaching of zinc it is still the dominant species at the surface or at the adjacent atomic layers. Roventi *et al*. reported that anomalous co-deposition of zinc and nickel at densities higher than 15 mA/cm^2 favors the discharge of zinc [52]. The leaching process might only affect the first atomic layers of Zn leaving behind a still high amount of this metal. Just as in the Permascand sample, Si is present in a small percentage on the sample most probably as a contaminant. No other element analyzed in XPS showed a similar binding energy to Si that could lead to be mistaken as Si.

The results for NiFe indicate that iron is the dominant species at the surface of the electrodeposited material, the Fe/Ni ratio is 2. The anomalous co-deposition favoring the discharge of iron over nickel has been attributed to the faster kinetics of Fe^{2+} [48]. The adsorption of Fe hydroxide on the substrate surface during electrodeposition is believed to prevent the reduction of Ni^{+2} resulting also in lower content of deposited nickel [53].

The atomic composition obtained for NiFe-LDH indicates a Ni/Fe ratio of 2. Luo *et al*. reported an atomic ratio of ~3 with the same method [54], and Alobaid *et al*. reported a ratio of ~5 with longer synthesis time [36]. This indicates that the hydrothermal treatment synthesis method is highly sensitive to conditions like time, type of autoclave and nature of the substrate utilized.

4.1.2 Number of active sites and electrochemical active surface area

Figure 4.2(A) presents the cyclic voltammogram obtained for both cell sides with fresh Permascand as both electrodes and serves a graphic explanation on how cyclic voltammograms were carried out in the electrolysis cell.

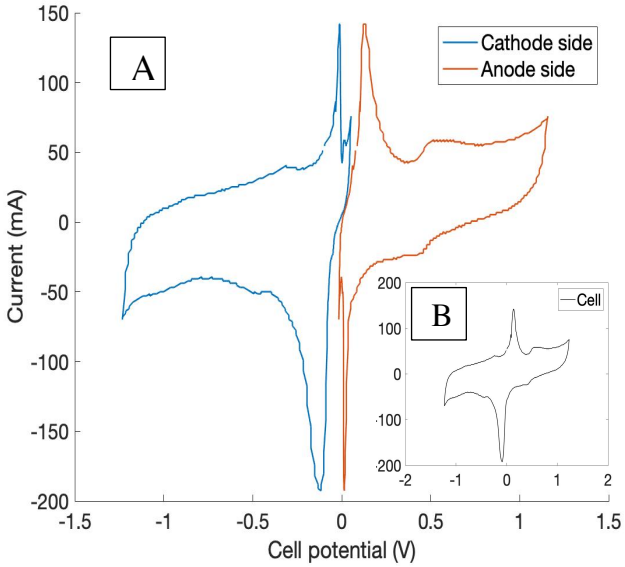

Figure 4.2. Cyclic voltammetry for both cell sides for the fresh Permascand electrode. Voltage range: - 1.23 to 1.23 V. Scanning rate: 50 mV/s. Electrolyte: 30% wt. KOH. Each individual electrode potential was measured by a pseudo-reference electrode. Zero-gap configuration.

The voltammogram for each electrode shows cathodic and anodic behavior due to the full potential range applied. The initial cycle started at a potential of 0 moving towards 1.23 V oxidizing the surface of the anode side electrode. This change in surface characteristics caused the different voltammogram shape for each electrode. Figure 4.2 (B) shows the overall cell voltammogram as obtained by the potentiostat.

The cyclic voltammograms for the synthesized electrodes (only anode side) that presented visible anodic peaks are displayed in Figure 4.3. The visible peaks labeled A to C correspond to the anodic peaks of the $Ni(OH)_2$/NiOOH redox couple [55]. The anodic peak for NiFe is not visible due to its relatively small size. No anodic peak was detected for Nickel mesh.

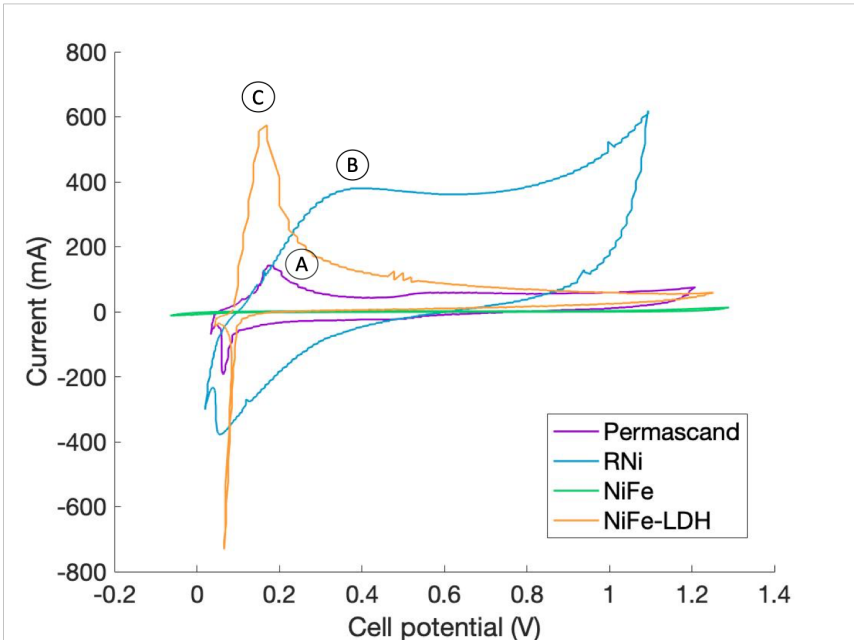

Figure 4.3. Cyclic voltammetry for fresh electrodes. Voltage range: 0 to 1.23 V. Scanning rate:50 mV/s. Potential measured with a pseudo-reference electrode, reported in reference to cell potential. Electrolyte: 30% wt. KOH. Zero-gap configuration.

The redox reaction responsible for the anodic peaks can be described by Equation 4.1 and involves the chemisorption of OH^- ions from the electrolyte and the transference of one electron. The amount of charge transferred represented by the area of the peak is an indicator of the number of Ni atoms that function as active sites for electrochemical interactions [56]. Active sites not only participate in the formation of NiOOH under anodic potential, they are also the sites where HER or OER can potentially take place.

$$Ni(OH)_2 + OH^- \rightarrow NiOOH + H_2O + e^- \quad (4.1)$$

Nickel is not the only species undergoing oxidation at anodic conditions. Permascand presented a second less noticeable peak appearing at 0.5 V believed to be the oxidation of RuO_2 or RuO_2•$Ru(OH)_3$ into Ru^{VI} species as proposed by Creus *et al*. [57]. There was no distinguishable peak for the oxidation of Fe^{2+} to Fe^{3+} as this transition happens at potentials significantly lower than for the Ni redox couple [35].

Table 4.2 presents an approximation of the number of active sites in each electrode material. The number of active sites was calculated according to Equation 4.2 [56]:

$$N = \frac{Q_{anodic\,peak}}{F}\, x \frac{6.022x10^{23} e^- mol^{-1}}{1e^-\,per\,active\,site} \quad (4.2)$$

where N is the number of active sites, Q is the charge transferred during the anodic peak and F is the Faraday constant. The calculation assumes that every transferred electron corresponds to an active site and only Ni

sites are quantified. The value calculated for RNi might include significant inaccuracies as the anodic peak is not clearly distinguished from the background current related to capacitive processes.

Table 4.2. Approximate number of active sites on the electrode materials.

Electrode material	Number of Ni active sties
Permascand	$1.54x10^{18}$
RNi	$1.06x10^{19}$
NiFe	$4.46x10^{16}$
NiFe-LDH	$7.44x10^{18}$

For an electrode with a geometric surface area of 30 cm^2.

The number of active sites predict that RNi and NiFe-LDH would have the best performance. However, not all active sites are as effective for water electrolysis. Introducing the concept of Turn Over Frequency (TOF) which quantifies the number of H_2/O_2 molecules evolved per second per active site is helpful to compare the efficiency of active sites at each electrode [56]. This value is presented in section 4.2.2 after the performance tests.

Double-layer capacitance functions as another method to estimate the amount of active sites [58]. Double-layer capacitance stems from the charging of the electrode surface when it is in contact with the electrolyte and a voltage is applied (see Appendix B). The charge on the surface is balanced by adsorbed ions with the opposite charge [9] and water molecules due to their dipolar nature. On the negative electrode, K^+ and H_2O would balance the charge while on the positive electrode, OH^- and H_2O would balance the lack of electrons. The adsorption of ions and water molecules mainly occur in sites where water electrolysis will also be favored at larger potential ranges.

The capacitive current (i_c) is related to the double-layer capacitance (C_{DL}) according to Equation 4.3:

$$i_c = sC_{DL} \tag{4.3}$$

where s is the scanning rate.

Figure 4.4 illustrates the results obtained for the Permascand electrode as an example. From the average slope of the forward and backward scans the double-layer capacitance can be calculated. To obtain the double-layer capacitance values presented in Table 4.3, the value of the average slope was multiplied by two as both electrodes were measured at the same time functioning like two capacitors in series.

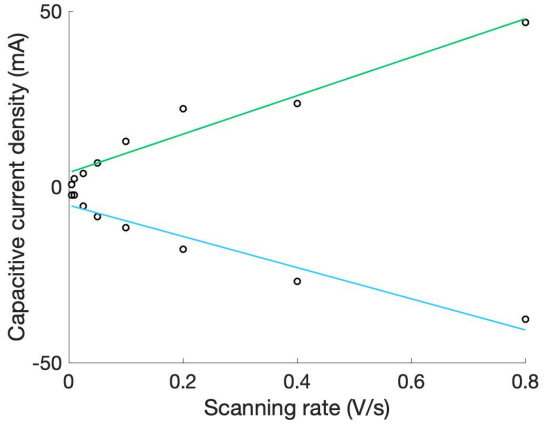

Figure 4.4. Capacitive current at different scanning rates. Permascand electrode with a geometric area of 30 cm^2. Electrolyte: 30% wt. KOH. Average slope obtained: 49.5 mF. The average slope was multiplied by two to obtain C_{DL} values as both electrodes were measured at the same time functioning like two capacitors in series.

The electrochemical active surface area (ECSA) can be calculated from the double layer capacitance (C_{DL}) and specific capacitance (C_s) which is the capacitance of an atomically smooth flat catalytic surface (see Eq. 4.4).

$$ECSA = \frac{C_{DL}}{C_s} \tag{4.4}$$

A value of 0.04 mF/cm^2 for C_s was taken for the calculations [58]. ECSA helps to compare the intrinsic amount of active sites in the electrode materials as its magnitude is directly related to the number of active sites [58].

The roughness factor (R_f) calculated in Equation 4.5 corresponds to the ratio between the surface area that participate in the interactions with the electrolyte (ECSA) and the geometric area of the electrode (S_{geo}). R_f helps to normalize the ECSA per unit of geometric area.

$$R_f = \frac{ECSA}{S_{geo}} \tag{4.5}$$

The ECSA values presented in Table 4.3 predict that RNi and NiFe-LDH would have the best performance for water electrolysis. In section 4.2.2, these values are used for the performance comparison of the different electrodes.

Table 4.3. Double-layer capacitance of fresh electrodes.

Electrode Material	Scanning range[1] (V)	Capacitance (mF)	ECSA (cm_{ECSA}^2)	Roughness Factor
Permascand	0.6-1	99	2475	82.5
RNi	0.5-0.9	588	14700	490
NiFe	0.6-1	23.4	585	19.5
NiFe-LDH	0.6-1	228	5700	190
Nickel Mesh	0.6-1	3.6	97.5	3.25
Smooth nickel [46]	-	5.7	142.5	4.75

[1]In reference to figure 4.3. For 30 cm^2 electrodes

4.2 Performance of electrode materials for alkaline water electrolysis

Figure 4.5 presents the performance for all the electrodes tested at atmospheric conditions. The Permascand and Raney nickel (RNi) electrodes had the best performance. This result can be explained by the reported high activity of RuO_2 [59] present in the Permascand electrode and the high electrochemical active surface area (ECSA) found for RNi in its characterization. The NiFe electrode showed the third best performance despite the low amount of material deposited on the substrate.

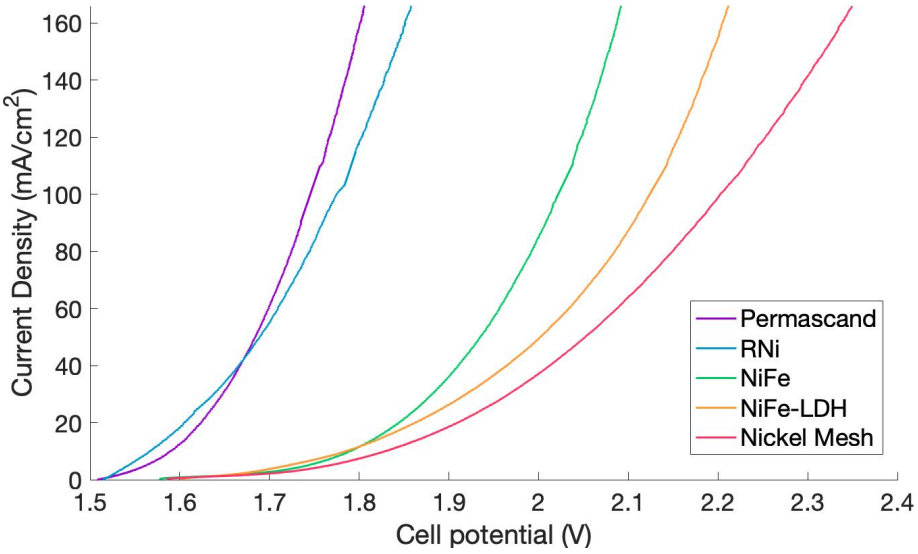

Figure 4.5. J-V curves for the different fresh electrodes tested. Same electrode material on both sides of the cell. Self-heating experiment, average external temperature: 27.5 °C[1]. Pressure: 1 bar. Electrolyte: 30% wt. KOH. Zero-gap configuration.

[1] The external temperature recorded for experiments presented in Figures 4.5 and 4.6 is presented in appendix C.1, the difference in temperature was considered to not be significant.

At a current density of 166 mA/cm², the electrodes Permascand, RNi, NiFe and NiFe-LDH presented an efficiency of 83%, 80% 71% and 67%, respectively. Meaning that at atmospheric conditions, Permascand, RNi and NiFe cover the efficiency requirement by ZEF (74% or 2V). As expected, nickel mesh had the lowest performance with an efficiency of 61%.

For comparative purposes, De Nora operates an alkaline electrolyser with an efficiency of 80% at 150 mA/cm² at 80ºC. De Nora uses Ni-plated steel for the anode and activated Ni-plated steel for the cathode, no further information is provided [9].

4.2.1 Tafel slopes for electrode materials

Figure 4.6 shows the overpotentials obtained for each electrode at the cathode (L) and anode (R) side. These overpotential were measured with the Pt pseudo-reference electrode.

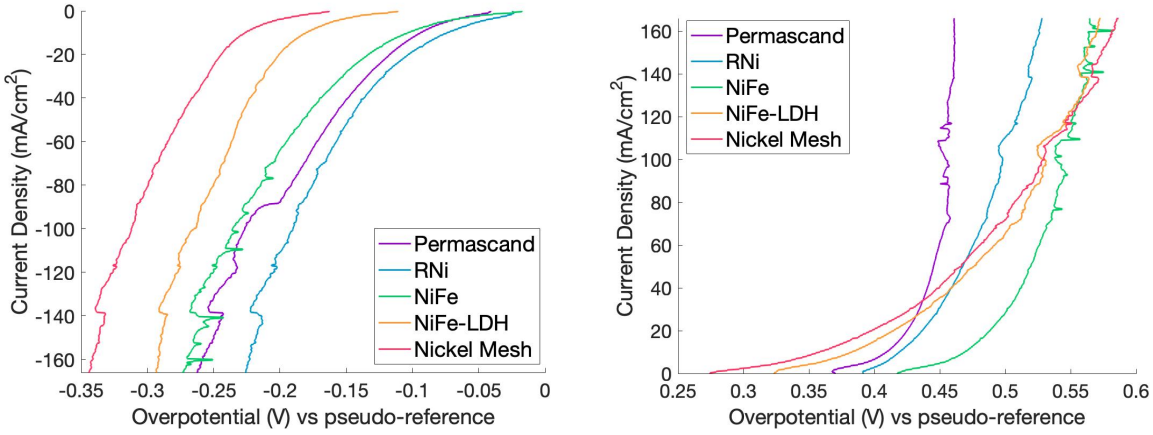

Figure 4.6. HER and OER overpotentials for the different fresh electrodes tested. (L) Cathode, (R) Anode. Self-heating experiment, average external temperature: 27.5 ºC[1]. Pressure: 1 bar. Electrolyte: 30% wt. KOH. Zero-gap configuration.

The best material for the cathode (Fig. 4.6 L) is RNi followed by Permascand and NiFe. This indicates that for HER the ECSA of RNi is more efficient than the RuO_2 active sites in the Permascand electrode. The Permascand electrode has a clear advantage in performance for OER (Fig. 4.6 R) due to the very active RuO_2 sites for this reaction [59]. The high electro-active area of RNi gives it the second-best performance

[1] The temperature recorded for experiments presented in Figures 4.5 and 4.6 is presented in appendix C.1, the difference in temperature was considered to not be significant.

as an anode material. The low performance of NiFe and NiFe-LDH, and similar performance to bare nickel mesh may indicate fast degradation of the material under oxidative conditions.

Figure 4.6 also indicates a degree of inaccuracy in the results. NiFe-LDH and nickel mesh performance for the cathode (L) appears to be shifted towards more negative voltages. In the same way, their performance for the anode side (R) appears to be shifted towards more positive voltages presenting an onset potential much lower compared to the other materials. This inaccuracy was introduced by the undefined conditions at the pseudo-reference electrodes. It is probable that without these inaccuracies both electrodes would present lower overpotential for HER and a higher one for OER. The voltage shift is not expected to affect the shape of the obtained curves.

From the best performing materials (Permascand, RNi and NiFe), Permascand presented the highest exchange current density (j_o) for the cathode side (see Table 4.4). RNi presented the lowest Tafel slope for the same cell side. A high j_o is desirable as it indicates fast kinetics at the equilibrium region, a low Tafel slope is desirable because it indicates a low increment of overpotential (η) with current at currents outside of the equilibrium region. The combined value of both kinetic parameters gives RNi the best performance for the cathode side.

Table 4.4. Tafel slopes and exchange-current densities for the materials tested.

	Cathode		Anode	
Material	j_o (A/m^2)	Tafel slope (mV/dec)	j_o (A/m^2)	Tafel slope (mV/dec)
Permascand	6.29	182	0.015	84
RNi	4.24	141	0.013	103
NiFe	3.74	164	0.0004	90
*NiFe-LDH	0.28	104	0.075	170
*Nickel mesh	0.14	111	0.22	201

Values obtained in 30% wt. KOH and average temperature of 27.5 ºC.
*Results affected by voltage shift of the j-v curves caused by the pseudo-reference electrodes.

Permascand presented the best kinetic parameters for the anode side resulting in the best performance for OER (see Table 4.4). RNi comes in second with a slightly lower j_o and higher Tafel slope resulting in a faster η increment with current. In addition to the high activity of Ru species, the larger oxygen (than hydrogen) bubbles produced on the anode side may explain the lower performance of RNi. The larger bubbles can block the porous structures in RNi diminishing the ECSA [60].

The results presented in Table 4.4 are comparable to values reported in the literature. However, the reported values vary with different electrolytes and concentrations. As an example, exchange current densities of 1.1×10^{-2} and 9.1×10^{-2} Am^{-2} for Ni and Fe, respectively, are reported for the cathode. Cathodic Tafel slopes of 121 and 133 mV are reported for the same materials in 1 M NaOH at 20ºC [61, 62]. For the

anode, exchange current densities of $1.7x10^{-1}$ and $4.2x10^{-2}$ for Ni and Fe, respectively. Anodic Tafel slopes of 95 and 191 are reported for the same materials in 50% wt. KOH at 90 ºC [63, 64].

Since all the Tafel slope values for HER are above 100 mVdec^{-}, they might indicate the rate determining step (RDS) is the Volmer step ($H_2O + e^{-1} \rightarrow H^{*} + HO^{-}$) [16]. The mechanism for OER is not yet agreed upon, however it is considered as a 2 or 4 electron process. The anodic Tafel slopes obtained are all above 80 mVdec^{-} and might indicate two RDS for OER: $M + OH^{-} \leftrightarrow MOH + e^{-}$ or $MOH + OH^{-} \leftrightarrow MO + H_2O + e^{-}$ [15].

4.2.2 Efficiency of active sites: TOF and ECSA

Figure 4.7 presents the comparison of the logarithm of Turn Over Frequency (TOF) for OER and the voltage obtained at 166 mA/cm^2.

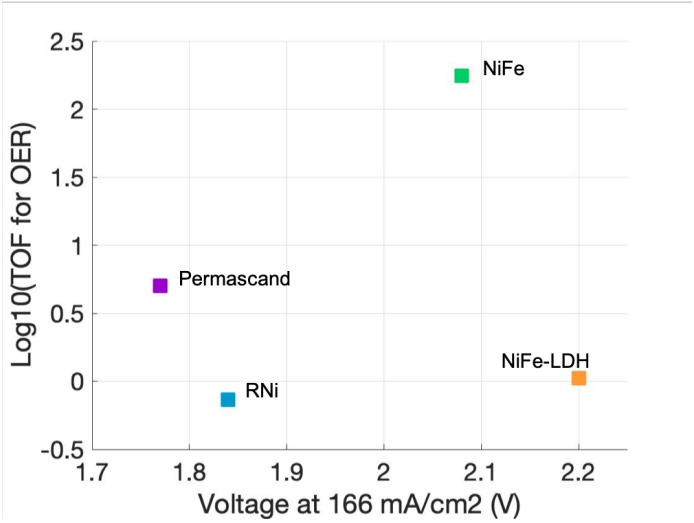

Figure 4.7. Logarithm of TOF for OER vs. voltage at 166 mA/cm^2. Same electrode material on both sides of the cell. Zero-gap configuration.

The TOF values were calculated according to Equation 4.6. The number of O_2 molecules evolved per second was calculated with Equation 4.7. The TOF for HER would be twice the one for OER at the same current. The number of active sites was taken from Table 4.2 and only considers Ni sites.

$$TOF = \frac{Number\ of\ H_2\ or\ O_2 molecules\ evolved\ per\ second}{Number\ of\ active\ sites} \tag{4.6}$$

$$O_2\ molecules\ evolved\ per\ second = \frac{i}{96485\ Cmol^{-1}} x \frac{6.022x10^{23}}{4e^{-}per\ O_2} \tag{4.7}$$

The TOF values obtained indicate that NiFe presented the most efficient active sites. NiFe active sites evolved 175 O_2 molecules per second per active site compared to 5 and 0.73 for Permascand and RNi,

respectively. This result highlights the high activity presented by NiFe individual active site indicating that its perceived lower activity might be caused by the low amount of material deposited not by the intrinsic activity of the material. The presence of Fe is believed to lower the average oxidation number of Ni and promotes a crystalline structure similar to β-NiOOH, highly active for OER [35]. The formation of the $NiFe_2O_4$ phase is also reported as the reason behind the high activity of NiFe electrodes [34].

Figure 4.8 compares the current density referred to the electrochemical active surface area (J_{ECSA}) and the voltage obtained at 166 mA/cm$_2$. J_{ECSA} was calculated according to Equation 4.8:

$$J_{ECSA} = \frac{i}{ECSA} \tag{4.8}$$

where i=5 A and the values for ECSA were taken from Table 4.3.

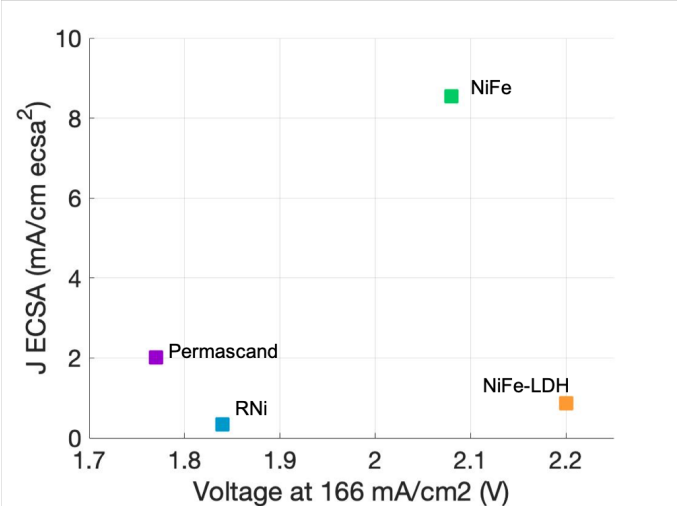

Figure 4.8. J_{ECSA} vs. voltage at 166 mA/cm^2. Same electrode material on both sides of the cell. Zero-gap configuration.

The J_{ECSA} values indicate that the NiFe electrode experience the highest 'real' current density referred to ECSA highlighting again the high activity of this material. As it was the case for the TOF, Permascand has the second highest J_{ECSA} indicating high activity in this material. The low J_{ECSA} obtained for RNi confirms that its high performance is due to its high ECSA. NiFe-LDH presented a not so different J_{ECSA} compared to RNi in addition to a higher TOF; however, it presented a significant lower performance suggesting that this material was degraded during the performance tests.

Compared to Figure 4.7, the values of J_{ECSA} do not vary as much as the values for TOF. The reason behind this is that ECSA (obtained through double-layer capacitance) quantifies the interaction of all the active sites present in the materials with the electrolyte, not only Ni sites as it is the case for TOF.

4.3 Stability of electrode materials for alkaline water electrolysis

Figure 4.9 presents the results obtained for the stability tests with a duration of 2.5 hours and consisting of 90 on/off cycles. As expected from previous results (Figure 4.5), Permascand and RNi presented the best performance.

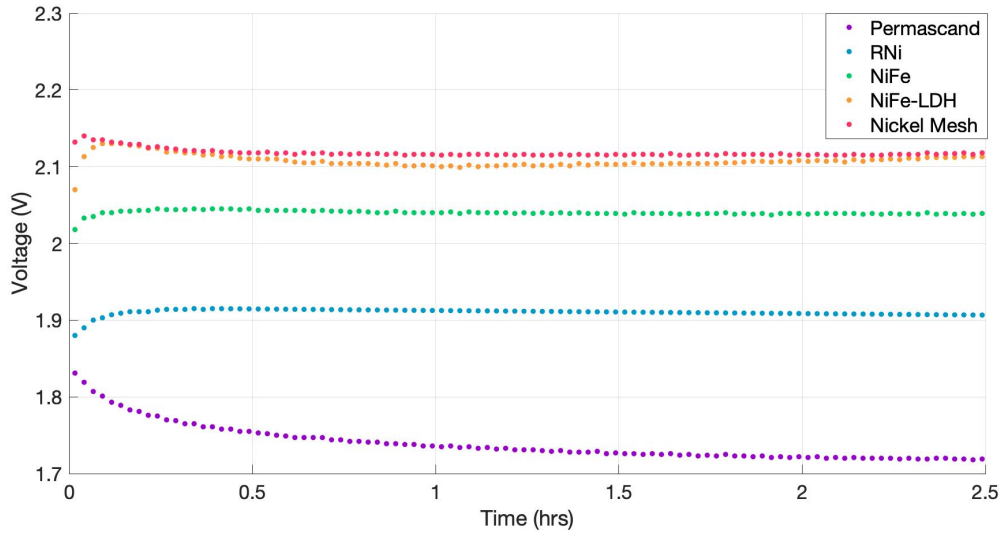

Figure 4.9. Stability tests for the different electrodes at 166 mA/cm². On/off cycles (75s/25s). Same material on both sides of the cell. Self-heating experiment, average external temperature: 32.7ºC[1]. Pressure: 1 bar. Electrolyte: 30% wt. KOH. Zero-gap configuration.

The decrease in voltage over time, much more noticeable in Permascand, might be due to a combined effect of increasing temperature during the experiment (see appendix C.2), and further activation of the material. The aging of nickel-based materials during operation increases the formation of the β- NiOOH phase, especially active for OER [33].

NiFe, NiFe-LDH and Nickel mesh showed a very stable performance during the tests. NiFe retained the third place in performance. On the other hand, NiFe-LDH presented a very similar performance to nickel mesh which indicates a significant degradation of the supported material.

The stability in performance by the end of test cannot be taken as a final conclusion on the long-term stability of the materials. Longer stability tests on nickel-based materials have reported gradual increments in voltage throughout days of operation [65].

To further detail the stability of the materials I present the individual change in overpotential, with reference to the first cycle in Figure 4.10. The general observation is that the overpotential for the cathode decreases influenced by the temperature increment during the experiment (and possibly due to aging of the

[1] The external temperature recorded for experiments presented in Figures 4.9 and 4.10 is presented in appendix C.2. The increase in temperature toward the end of the experiment is expected to increase the performance of the electrodes.

material). The changes in overpotential for the anode vary from material and indicate a combined effect of temperature increment and degradation.

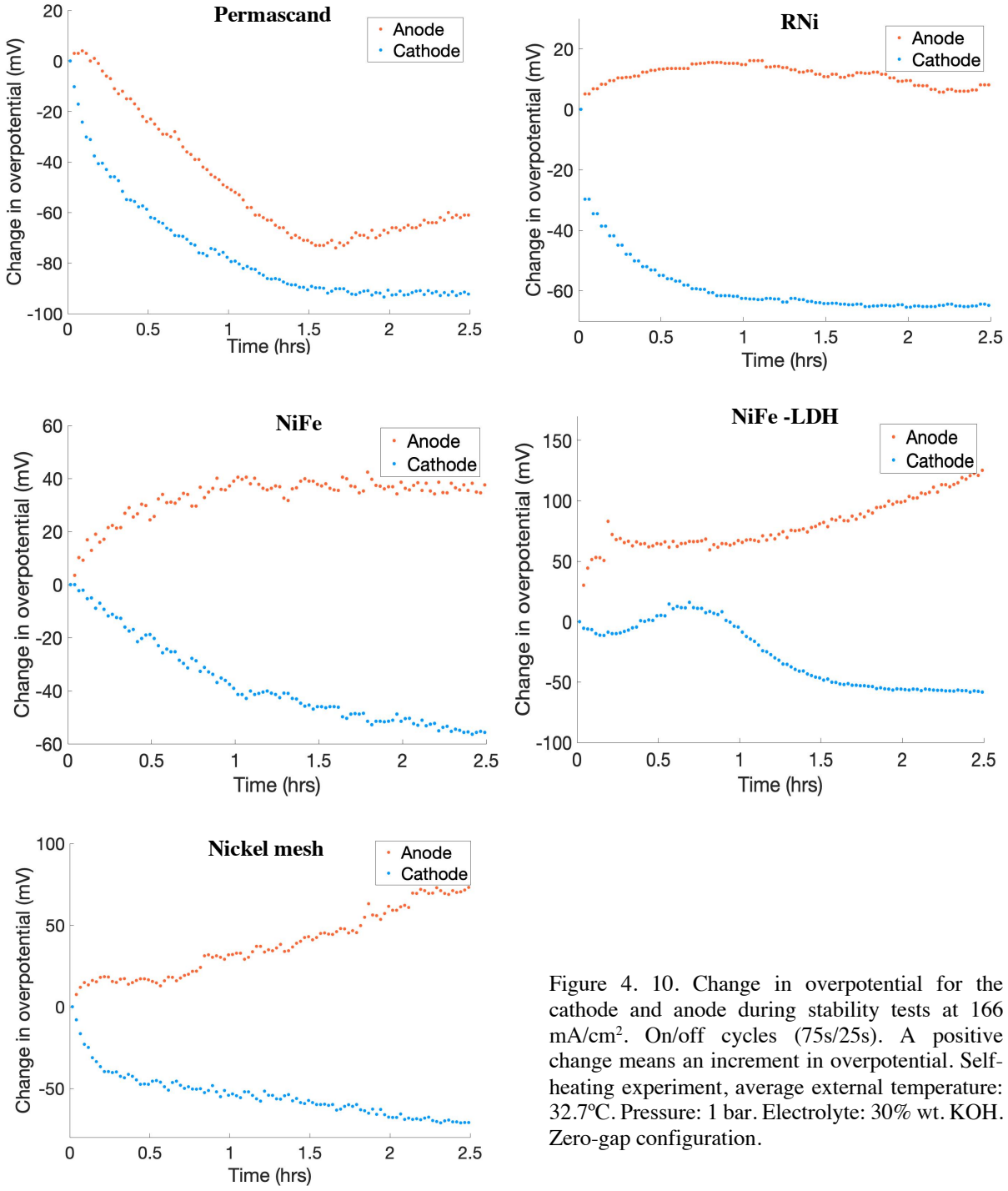

Figure 4. 10. Change in overpotential for the cathode and anode during stability tests at 166 mA/cm^2. On/off cycles (75s/25s). A positive change means an increment in overpotential. Self-heating experiment, average external temperature: 32.7ºC. Pressure: 1 bar. Electrolyte: 30% wt. KOH. Zero-gap configuration.

Figure 4.10 indicates that the stable performance observed in Figure 4.9 might be the result of the combined effect of temperature (cathode) and degradation (mainly anode) cancelling each other. The following observations are made for each material:

Permascand. The steep decrease in overpotential for the cathode might further indicate activation of the electroactive surface during the first minutes of the experiment [66]. The increment in the anode overpotential after 1.5 hours might indicate degradation of the material under oxidative conditions.

RNi and NiFe. The cathode side also presented a decrease in overpotential due to increment in temperature and possible further activation. The anode side indicates initial deactivation and then material stability for the second half of the test.

NiFe-LDH. The cathode side presented an interesting behavior. An overpotential increment that might indicate material degradation at the cathode is observed at the 1-hour mark followed by a decrease most likely related to temperature. The anode side shows a steep increase in overpotential hinting to substantial degradation of the deposited material.

Nickel mesh. The cathode side also presented a decrease in overpotential due to increment in temperature and possible further activation. The anode side showed deactivation in time. There is no proper explanation for the last phenomenon since the surface and bulk of this material has the same composition and R_f.

Section 4.4 further discusses the deactivation of the materials and hypothesizes on the mechanisms causing this deactivation.

4.4 Changes in surface and electroactive characteristics

The stability tests were expected to cause surface and composition changes on the materials. These changes can be observed with SEM and XPS analysis. The physical and chemical changes affect the electroactive characteristics of the materials, for this reason, cyclic voltammetry at different voltage ranges and scanning rates was used. This characterization techniques help understand the origin of changes in performance of the spent electrode materials.

4.4.1 Surface morphology and elemental composition after stability tests

Figure 4.11 and Figure 4.12 present the SEM pictures obtained after the 90 on/off cycles. Permascand and Raney nickel (RNi) showed the least degradation of the materials tested. Permascand was the most active and stable material during the test. In its pictures it is clear that no significant changes occurred at the surface of the cathode or anode. RNi pictures show significant degradation of the surface structure, specially at the anode. The oxidative conditions at the anode affect the surface structure and can ionize and dissolve the anode material [8, 67].

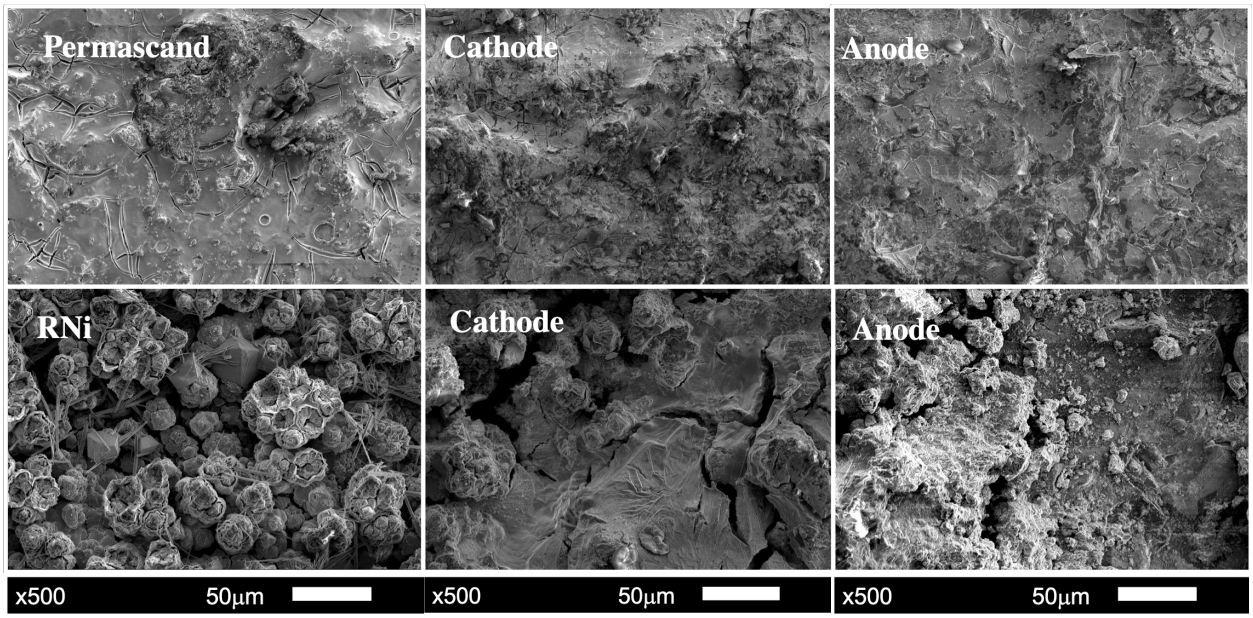

Figure 4.11. SEM pictures for the fresh electrodes and after stability tests: Permascand and RNi. Magnification: x500. Detector parameters: SEI 5kV.

NiFe pictures (see Figure 4.12) show degradation of the material deposited. On the cathode side, the distinguishable original structures are visible on the substrate edge but not on the flat surface. The degradation at the anode side is more extensive as the material that is left on the surface lost its original structure. NiFe-LDH presented the most extensive degradation even for the cathode side. The original

porous structure seems to be completed degraded (especially for the anode), the remaining deposited material has a rough aspect and looks similar for the cathode and anode.

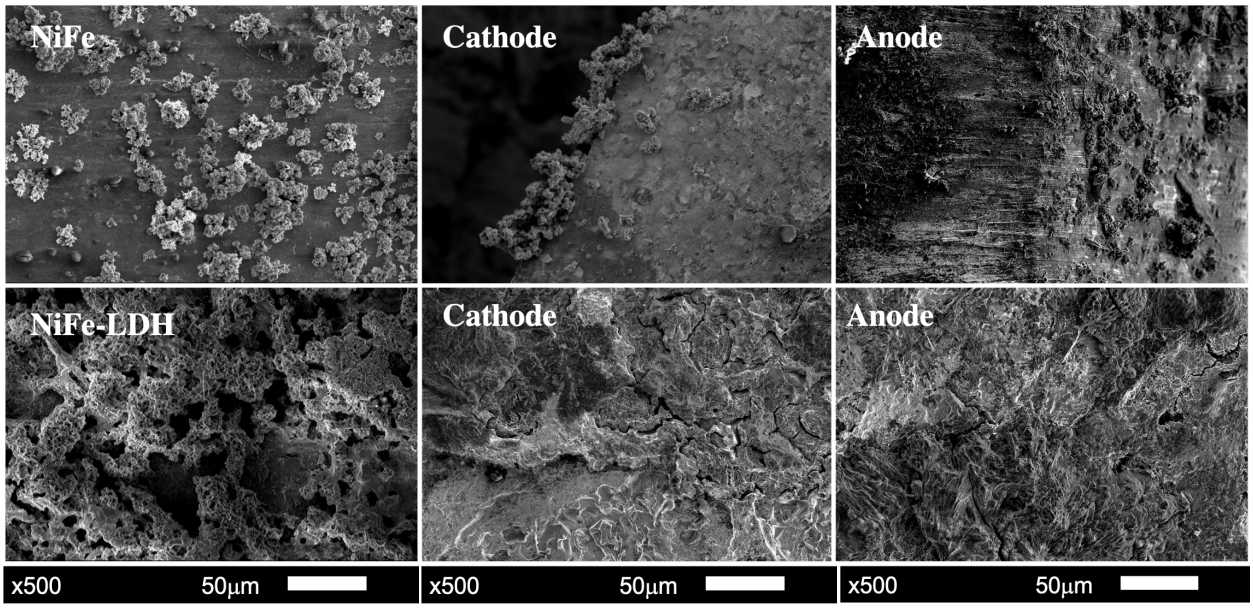

Figure 4.12. SEM pictures for the fresh electrodes and after stability tests: NiFe and NiFe-LDH. Magnification: x500. Detector parameters: SEI 5kV.

The SEM pictures in Figures 4.11 and 4.12 make it obvious that the synthesized electrodes underwent degradation during the stability tests, especially noticeable for NiFe-LDH. RNi and NiFe held better their original structure while Permascand seems to be unaffected by the electrolysis conditions.

Table 4.5 presents the XPS results for the atomic composition of fresh and spent electrodes. One of the general observations for the materials as cathodes and anodes is that after the stability tests, the oxygen content increased. This indicates that a more oxidized surface is formed during electrolysis, especially for the anode. The second observation is that nickel content (in percentage) increased when compared to the fresh electrode for the anode and cathode. This is the result of surface degradation as the other metals (Fe) are depleted from the surface.

Table 4.5 XPS elemental analysis for electrodes after stability tests.

	%Atomic content		
	Fresh electrode	Cathode	Anode
Permascand			
O	60.91	76.67	81.33
Al	1.24	1.2	2.35
Ni	11.07	13.84	10.70
Ru	20.34	7.51	5.55
Cl	4.08	0.75	-
Si	2.34	-	-
Raney Nickel (RNi)			
O	64.31	73.10	76.62
Ni	5.73	25.39	20.74
Zn	26.10	1.52	2.17
Si	3.84	-	0.45
NiFe			
O	68.53	73.96	77.70
Ni	10.52	21.34	21.82
Fe	20.94	4.69	0.46
NiFe-LDH			
O	60.72	69.70	72.62
Ni	17.84	28.42	26.57
Fe	9.58	1.87	0.81
Si	11.82	-	-

On the specific side, Permascand presented an important decrease in Ru content in the anode and cathode after electrolysis operation. This can be due to surface degradation under electrolysis conditions; however, RuO_2 is reported to be a very stable catalyst [24]. Another reason can be local differences in Ru content as the XPS analysis was performed on a single point of the sample (not the same for fresh and spent electrodes).

RNi presented a steep decrease in Zn most likely due to surface degradation during the tests exposing Zn to OH^- in the electrolyte resulting in its leaching. NiFe and NiFe-LDH presented a steep decrease in Fe content, especially in the anode. The reason behind this is most likely degradation of the surface and depletion of Fe from the anode.

Appendix E presents the XPS spectra for the fresh and spent electrodes. The main findings include that nickel is mostly present as $Ni(OH)_2$, in fresh and spent samples. NiO was only detected in the fresh Permascand electrode. No clear evidence of Ni^{3+} was detected; however, the presence of NiOOH has been extensively reported in nickel-based anodes [68].

In the case of Ru, it was mostly found as RuO_2 with $RuO_x(2<x\leq3)$ only found in the Permascand anode due to the oxidative conditions during electrolysis. Fe was found as a mixture of Fe^{2+} and Fe^{3+} in NiFe. A decrease in the signal for Fe^{2+} was detected for the spent NiFe electrodes, especially for the anode

indicating oxidation of Fe^{2+} into Fe^{3+}. As expected, Fe in NiFe-LDH was found as Fe^{3+}. It retained its oxidation state in the spent NiFe-LDH electrodes.

4.4.2 Electrochemical active surface area after stability tests

Figure 4.13 presents the cyclic voltammogram for the anode side after the stability tests (cathode side presented the same shape). The current measured for all the electrodes was much lower in comparison to the initial voltammogram (see Figure 4.3). Additionally, no anodic peaks were registered for any of the electrodes which does not allow the calculation of the number of Ni active sites. The experiment was repeated three times with clean electrolyte; however, the same result was obtained.

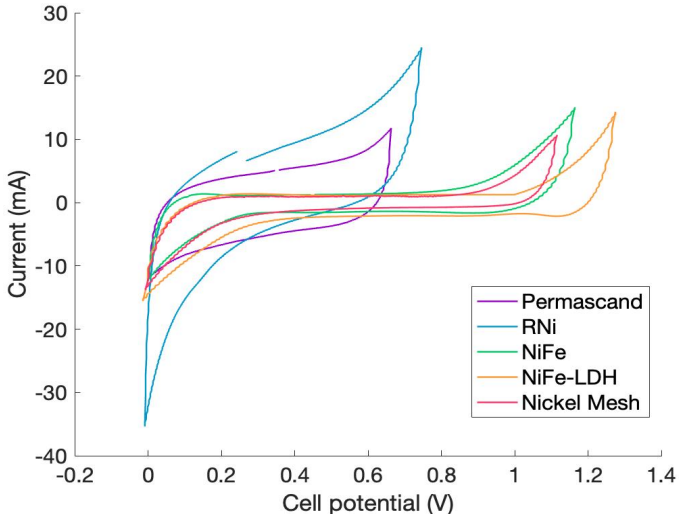

Figure 4.13. Cyclic voltammetry for electrodes after stability tests. Voltage range: 0 to 1.23 V. Scanning rate:50 mV/s. Potential measured with a pseudo-reference electrode, reported in reference to cell potential. Electrolyte: 30% wt. KOH. Zero-gap configuration.

One of the possible explanations for this behavior might be the degradation of the anode. A decreased surface area would lower the current flowing during cyclic voltammetry. This explanation does not hold especially for Permascand as it showed great stability. Another possibility is that the materials might be showing surface deactivation that can be overcome at higher potentials. Mauer *et al*. report the formation of surface hydrides on the cathode side, however, this deactivation process is reported to be irreversible [69].

In spite of the apparent low electroactive surface area of all the electrodes, Permascand and RNi show the most active surface. RNi shows the highest capacitive behavior. The voltammograms for these two electrodes seem to have a shorter scanning range, however, the experimental parameters were the same for all the materials. The shortened potential range is possibly a result of the undefined conditions at the pseudo-reference electrode.

Table 4.6 presents the ECSA for the electrodes after the 90 on/off cycles. In contrast to Figure 4.13, the results are in line with the performance recorded (Fig. 4.9) and SEM pictures after the stability tests (Fig. 4.11 and 4.12). Permascand is shown to retain its ECSA while the other materials show a significant decrease.

Table 4.6. Electrochemical active surface area after stability tests.

Electrode Material	ECSA fresh (cm_{ECSA}^2)	ECSA after stability (cm_{ECSA}^2)
Permascand	2475	2325
RNi	14700	4800
NiFe	585	142.5
NiFe-LDH	5700	157.5
Nickel Mesh	97.5	105

RNi ECSA decreased to a third of its original value. NiFe retained only one fourth of its original value, while NiFe-LDH had the biggest decrease retaining 1/35 of its original value. The reason for this is the destruction of the surface structures during the stability test. The small increment in nickel mesh capacitance might be due to the material becoming slightly rougher during the test.

The ECSA values indicate that, after the stability tests, Permascand and RNi have the largest electrochemical active surface area of the materials tested. However, RNi suffered a significant degradation at electrolysis conditions.

According to observations in the SEM pictures (Fig. 4.11 and 4.12), changes in surface composition (Table 4.5) and decrease in ECSA (Table 4.6) we can hypothesize two paths of electrode material degradation: physical break down of the surface structures and dissolution of surface species. The physical damage is believed to be caused by the mechanical stress caused by the evolution of H_2 or O_2 in the porous structures of the materials. The dissolution of the surface species is promoted by the oxidative potentials at the anode [70]. Figure 4.14 presents a schematic representation of the proposed degradation processes.

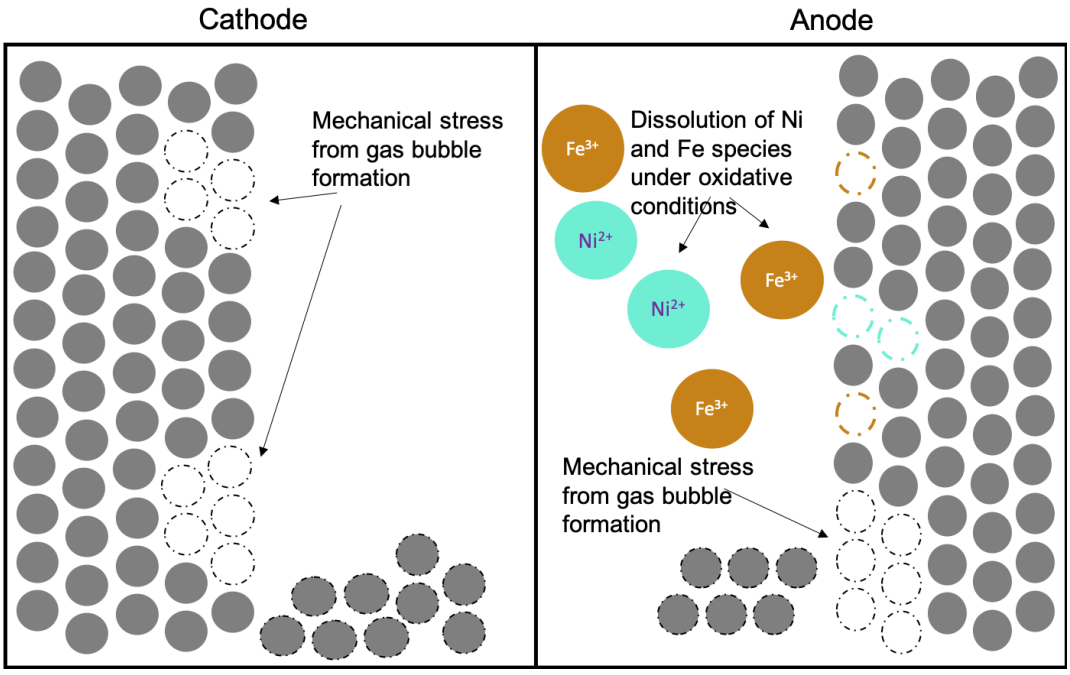

Figure 4.14. Schematic representation of the processes involved in electrode degradation for a NiFe electrode. This representation applies to nickel-based electrodes with or without Fe.

The surface degradation resulting from mechanical stress may help explain the significant degradation observed on the nano-structured NiFe-LDH electrode. Its highly porous structure may make it especially susceptible to damage during the formation of gas bubbles and during manipulation.

Regarding the dissolution of species at the surface, no exact information about the dissolution of Ni species was found. However, Ye *et al*. reported that Ni is liberated as Ni^{2+} under oxidative conditions at potentials above the formation of the NiOOH phase [71].

The dissolution mechanism of Fe is more defined: Equations 4.9 and 4.10 represent the redox process involved in the dissolution of FeOOH. The reaction in Eq. 4.9 is promoted by the oxidative conditions in the anode and is reported to happen at 0.70 V vs. SHE in 1M NaOH [72].

$$FeOOH + 5OH^- \leftrightarrow {FeO_4}^{2-} + 3H_2O + 3e^- \ (-0.70\ vs.SHE) \tag{4.9}$$

$$4\left({FeO_4}^{2-}\right) + 10H_2O \leftrightarrow 4Fe^{3+} + 3O_2 + 20\ OH^- \tag{4.10}$$

Additionally to the dissolution of Fe, the deposition of the stripped Fe^{3+} on the cathode has been reported [70]. This process may result in increased activity of cathode electrodes.

4.5 Effect of pressure on cell voltage

Fort the pressurized tests, RNi was selected for the cathode and Permascand was selected for the anode. These materials presented the best performance for both HER and OER, and RNi was the only synthesized material with similar performance to the Permascand electrode. Figure 4.15 presents the results for the performance tests at different pressures. The performance obtained for this combination of electrodes at 1 bar is lower than the original obtained for Permascand or RNi (see Figure 4.5), the reason is the degradation overtime of surface structures in RNi during the stability tests.

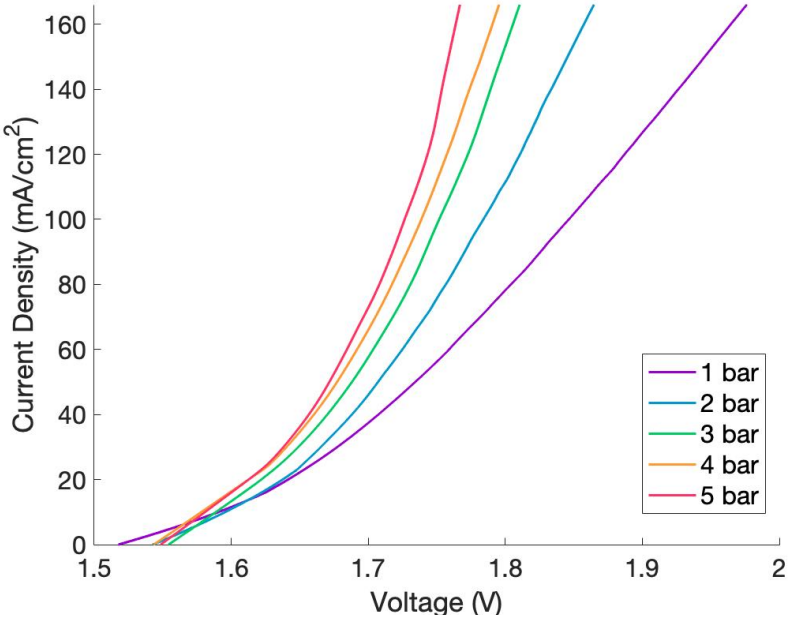

Figure 4.15. J-V curves at different N_2 pressures. Permascand as anode and RNi as cathode. Self-heating experiment, average external temperature: 26.5 °C[1]. Electrolyte: 30% wt. KOH. Zero-gap configuration.

Increasing the operating pressure with N_2 decreases considerably the voltage needed to produce the same current density. Increasing the pressure increases the efficiency of the electrolysis cell from 74% at 1 bar to 82% at 5 bar. This observed increase in efficiency might allow ZEF to avoid using expensive electrodes (Permascand) while still obtaining their efficiency setpoint of 74%.

The reduction in voltage is believed to be the result of decreasing the bubble size of gas products (reducing ohmic resistances) when applying pressure to the system [9]. The decrease in voltage is less noticeable as the base-line pressure increases; increasing the pressure from 1 bar to 2 bar has the biggest impact. This trend may indicate an inverse correlation with pressure similar to the volume of gas according to the ideal gas equation ($V=nRT/P$) indicating that the size of bubbles is most likely the reason for the

[1] The external temperature recorded for experiments presented in Figure 4.13 is presented in appendix C.3, the difference in temperature was considered to not be significant.

decrease in voltage. Important to remember that the cell has a zero-gap configuration and still benefits from the increased pressure.

Frey F. reported in 2016 that hydrogen and oxygen bubbles have a negative potential correlation with applied pressure in the electrolysis cell. It was also reported that oxygen bubbles have a larger average diameter. Equations 4.11 and 4.12 were reported for the mean bubble diameter for hydrogen and oxygen, respectively [73]. The negative correlation with P (pressure) is in line with the voltage decrease with increasing pressure.

$$\frac{dh_{2,mean}}{\mu m} = \frac{31.073}{P^{0.319}} \tag{4.11}$$

$$\frac{dO_{2,mean}}{\mu m} = \frac{40.34}{P^{0.28}} \tag{4.12}$$

Figure 4.16 takes experimental points from Figure 4.15 to illustrate the inverse correlation of voltage and pressure. It presents the experimental points at a current density of 166 mA/cm^2 fitted, with a high coefficient of determination, to a line defined by Equation 4.13.

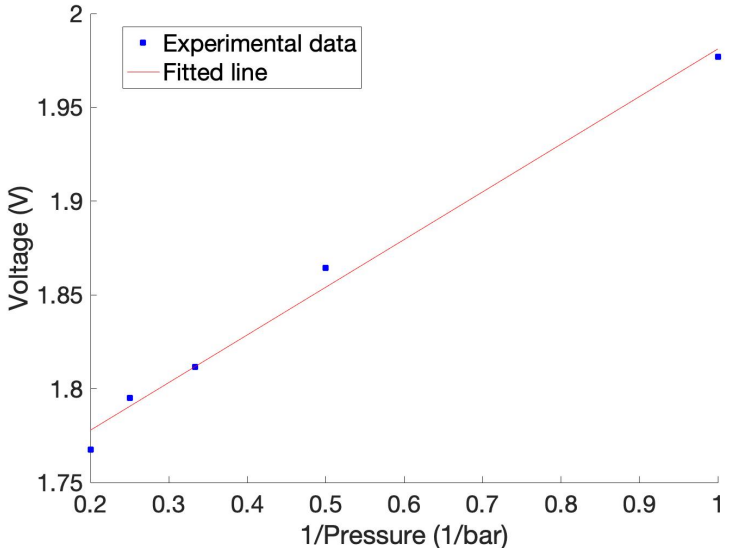

Figure 4.16. Linear fitting of experimental data at 166 mA/cm^2 at different N_2 pressures. Average temperature: 26.5 ºC. $V(P)= 0.244/P + 1.73$. $R^2= 0.9958$.

$$V_{166}(P) = \frac{0.244}{P} + 1.734 \tag{4.13}$$

Assuming that the positive effect of increasing pressure is only due to decreasing bubbles size, Equation 4.13 indicates that 1.73 V is the voltage needed to produce that current when no bubbles are present at the electrode surface and adjacent electrolyte.

Equation 4.13 only considers the effect of pressurizing with N_2 in the 1-5 bar range. ZEF, however, requires pressurizing the electrolyser up to 50 bar. Hydrogen and oxygen will be pressurized so this will also impact the thermodynamic potential for water electrolysis. Equation 4.14 is the result of fitting the experimental data while considering the thermodynamic effect (see appendix D).

$$V_{166}(P) = \frac{0.339}{P} + \frac{RT}{nF}\ln\left(\frac{P_{H_2}P_{O_2}^{1/2}}{a_{H_2O}}\right) + 1.646 \tag{4.14}$$

The three terms in the equation are related to (from left to right): 1) the effect of pressure on bubble size, 2) the thermodynamic effect of pressurizing the cell and 3) standard potential, kinetic overpotentials at the electrodes, and ohmic losses at the membrane and electrolyte.

Equation 4.14 is plotted in Figure 4.17 up to a pressure of 50 bar. The most significant decrease in voltage due to the pressurization of the cell happens in the first 5 bar. During the first 5 bar, the reduction in bubble size is expected to be the most important factor influencing voltage. After this pressure, the increment in the thermodynamic potential starts to overcome the reduction in ohmic losses due to the decreasing bubble size.

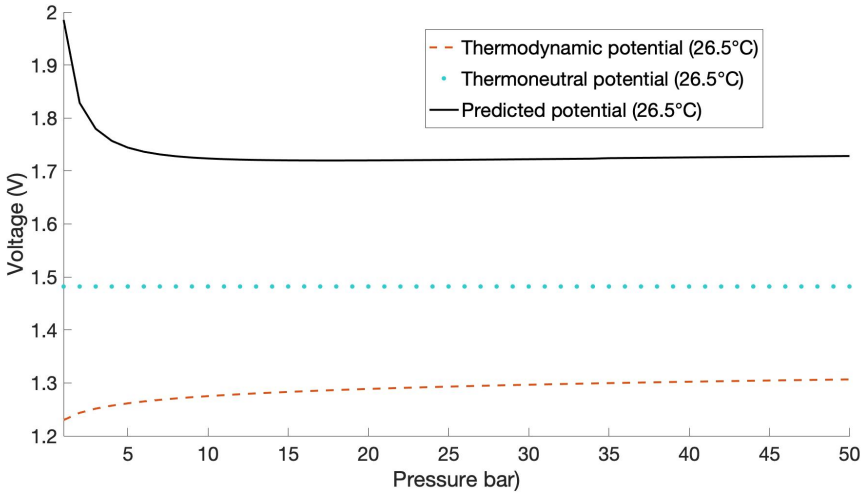

Figure 4.17. Estimated cell voltage at 166 mA/cm² at different pressures. Permascand as anode and RNi as cathode. Temperature: 26.5ºC. Zero-gap configuration.

The minimum cell voltage can be found at 17 bar (1.729 V), after this pressure, the cell voltage starts to increase slowly. However, the operating pressure of 50 bar needed by ZEF would still reflect benefits from a decrease in voltage most likely due to a smaller size of gas bubbles at the electrodes surface and electrolyte.

4.6 Summary of performance and material costs

ZEF's energy balance requires to operate the alkaline electrolyser with a maximum voltage of 2 V per cell, and a current density of 166 mA/cm^2. Figure 4.18 presents the cell voltage at the end of the stability tests for the electrode materials analyzed in this project. The Permascand and RNi are the only electrodes that can provide 166mA/cm^2 under 2V. NiFe presented the third best performance needing 2.04 V to reach the mentioned current density. NiFe-LDH seems to offer little advantage compared to nickel mesh.

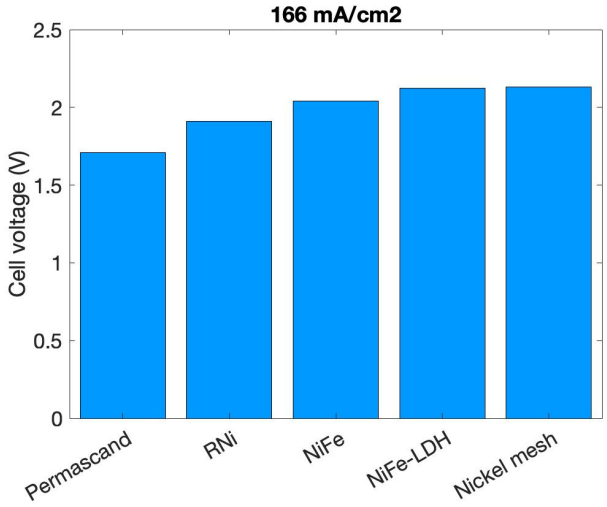

Figure 4.18. Stable electrode performance at 166 mA/cm^2. Corresponds to the final voltage measurement in the stability tests. Pressure: 1 bar.

Figure 4.19 presents the cost estimation for the electrode materials. The estimation only considers the cost of metals, it does not include the cost of manufacturing. From ZEF provided data, the cost of the nickel mesh substrate per electrode is 2 € which amounts to most of the cost for the synthesized materials. In the case of the commercial Permascand electrode, the content of ruthenium (Ru) indicates that it would cost 4.6 € per electrode, more than twice the cost for the synthesized electrodes. Appendix F presents the data for the cost estimation.

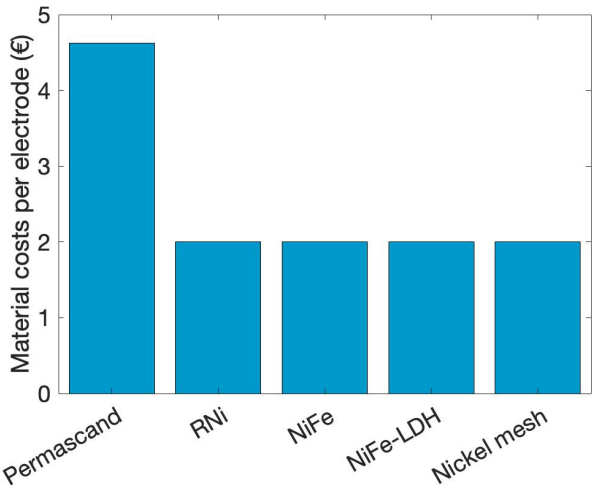

Figure 4.19. Materials costs estimation for the electrodes. Synthesis costs are not considered. The cost of nickel mech (substrate) is estimated to be 2 € (provider: Permascand).

Figure 4.20 presents the cumulative cost of electrodes and electricity for a single electrolysis cell. The estimates are based on a levelized cost of electricity of 0.078 €/kWh [74] and 8h of operations per day. The voltage required for each material corresponds to the final voltage measured in the stability test (see Fig. 4.18) and the current corresponds to 5 A or 166 mA/cm^2. The synthesized electrodes and the Nickel mesh were assumed to have a lifetime of 3 years as commercial nickel electrodes are reported to have a lifetime of 10,000 h of operation [75].

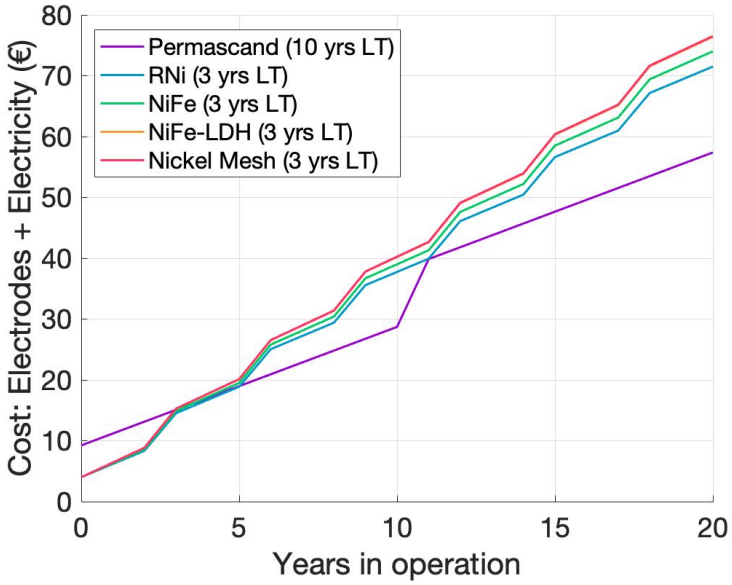

Figure 4.20. Cumulative cost of electricity and one set of electrodes vs. years in operation. The Permascand electrode was assumed to have a lifetime of 11 years. The rest of the electrodes were assumed to have a lifetime of 3 years. Calculations based on a current density of 166 mA/cm^2 and 8 hours of operation per day.

The results indicate that Permascand would need to have a lifetime of at least 11 years to remain cost competitive compared to the synthesized electrodes and Nickel mesh. Even with an extended lifetime, Permascand would not become the cheapest option until the first five years of operation.

Figure 4.21 presents the estimated cell voltage at a pressure of 50 bar and a current density of 166 mA/cm^2. It was assumed that the decrease in voltage with pressure modelled in Equation (4.14) for the combination of Permascand and RNi would apply to all the electrodes tested. The estimated decrease in voltage at 50 bar amounts to 0.25 V. This results in all the electrode materials tested operating at a voltage lower than 2V for a current density of 166 mA/cm^2.

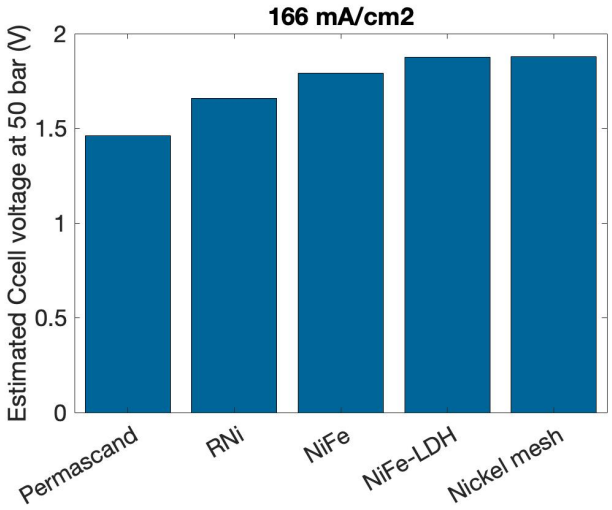

Figure 4.21. Estimated cell voltage at 50 bar for a current density of 166 mA/cm^2.

ZEF requirements could be covered with nickel mesh electrodes which would offer the lowest cost and easiest manufacturing. However, more efficient electrode materials could offer ZEF more flexibility regarding design (for higher current densities) and energy balance considerations.

5

Conclusions and recommendations

5.1 Conclusions

Zero Emission Fuels (ZEF) is developing an alkaline electrolyser that needs to be integrated into a micro methanol plant. The electrolysis cells composing the electrolyser are needed to operate at 166 mA/cm^2 under 2V to comply with the energy balance of the whole system. Additionally, the electrode materials were required to be low cost and made out of materials readily available. This thesis investigated the performance of synthesized nickel-based electrodes in a zero-gap alkaline electrolysis cell. A functional self-heating alkaline electrolysis setup was designed and built for experimentation at atmospheric conditions and up to a pressure of 5 bar.

Electrodeposition and hydrothermal treatment are effective and simple methods to synthesize nickel-based electrodes with a size of 30 cm^2 for alkaline water electrolysis. Cyclic voltammetry and capacitance tests proved that the synthesized electrodes greatly increased the electrochemical active surface area relative to a smooth nickel electrode. The Raney nickel electrode incremented the active surface area 150 times. NiFe-LDH increased the surface area by a factor of 58 while NiFe did it by a factor of 6.

The Raney nickel electrode has an initial performance comparable to a commercial electrode containing RuO_2. In the initial performance test, the commercial (Permascand) and Raney nickel electrodes were able to operate at 1.78 and 1.85 V, respectively. Their high performance was attributed to the highly active RuO_2 active sites present in the Permascand electrode and to the large electrochemical active surface area of Raney nickel. RuO_2 active sites were found to be fundamental for a lower OER overpotential while HER overpotential can be lowered with high availability of nickel active sites (large surface area).

The electrodeposited NiFe electrode had a better performance than the iron-doped electrode prepared through thermal treatment (NiFe-LDH). Neither electrode can provide the desired current of 166 mA/cm^2 under 2V. However, NiFe with an initial voltage of 2.08 V has an acceptable performance considering its low surface area. This relatively high performance is attributed to the presence highly efficient active sites promoted by the presence of Fe, especially beneficial for HER.

The Raney nickel electrode presented acceptable stability for HER. With a voltage of 1.9 V after 2.5 hours of cycling, Raney nickel was still able to produce the desired current density under 2 V. The Raney nickel electrode for the cathode side (HER) presented further activation during the experiments. The better performance after cycling was attributed to an increase in temperature in the setup and to aging of

the electrode. Raney nickel at the anode side (OER) presented significant degradation of the surface structures due to oxidative conditions. NiFe and NiFe-LDH suffered significant degradation on the cathode and anode sides during the stability tests. The Permascand electrode presented complete stability for the cathode and anode side.

Increasing the applied pressure with N_2 in the zero-gap electrolysis cell significantly decreased the voltage needed to deliver 166 mA/cm^2. Pressure and voltage were proven to have an inverse relationship in the pressure range of 1 to 5 bars. This hints that the decrease in voltage observed is due to decreasing the volume of gas bubbles present in the electrolyte and at the electrodes. A simple model estimating the voltage change in a range of 1-50 bar, also considering the thermodynamic effect of pressurizing the produced H_2 and O_2, indicated that a decrease of 0.25 Vis obtained when pressurizing the zero-gap cell up to a pressure of 50 bar.

The expected decrease in voltage would result in all the electrodes tested, including bare nickel mesh, to produce a current of 166mA/cm^2 with a voltage under 2V. This gives ZEF the option of avoiding the use of expensive Ru electrodes. It also gives ZEF the flexibility of using only smooth nickel electrodes or Raney nickel for the cathode and smooth nickel for the anode for higher efficiency.

The results obtained in this thesis provided information about the performance of nickel-based electrodes in a zero-gap alkaline electrolysis cell. This thesis also offered information about the effect of pressure on voltage for this electrolysis cell configuration. The results presented opened the option for ZEF of using cheap nickel-based electrodes. Finally, this thesis offered ZEF its first electrolysis operation at higher than atmospheric pressures linking knowledge in setup design and manufacture, and knowledge in electrode materials.

5.2 Recommendations

- On electrode materials

Raney nickel presented a high performance for water electrolysis, especially as a cathode material. NiFe presented a relative high performance considering its low electrochemical active surface area. Combining the high surface area of Raney nickel with a co-deposited mixture of nickel and iron could offer a highly active electrode material, especially for HER.

- On the setup

The temperature inside the electrolysis cell is an important factor influencing the voltage needed. For ZEF it would be useful to control the temperature during tests to get more accurate data regarding the expected performance of their electrolyser.

The use of platinum wire as a pseudo-reference electrode for the measurement of individual electrode potentials introduced inaccuracies. The undefined conditions in the electrolyte, H_2, O_2 and OH^- concentrations limited the comparability of the measurements for the different electrode materials. A stable and reliable reference electrode would facilitate the measurement of electrode overpotentials.

- On additional experiments

The results presented in this thesis assumed that all the measured current was due to water electrolysis. It is possible that other processes inside the cell were responsible for the measured current. Material oxidation, gas mixing inside the electrolyte or current leakages resulting from the cell configuration can all consume electrical current. Measuring the amount of hydrogen and oxygen produced is necessary to verify the Faradic efficiency during the tests.

Due to practical and safety impediments it was not possible to conduct stability tests for a longer period of time. For most of the synthesized electrodes it was clear that material degradation happened in the first minutes of the test; however, longer stability tests would offer more insight into the behavior of the electrode materials and the setup in the longer run.

Also due to safety considerations, pressurized tests at pressures higher than 5 bar were not carried out. Tests up to a 50 bar of pressure would offer the real performance value and setup behavior that ZEF would obtain during real operation of the electrolysis unit.

References

1. Henrik Zsiborács; Nóra Hegedüsné Baranyai; András Vincze; László Zentkó; Zoltán Birkner; Kinga Máté; Gábor Pintér, *Intermittent Renewable Energy Sources: The Role of Energy Storage in the European Power System of 2040*. Electronics, 2019. **8**: p. 18.
2. Patrick Schmidt; Werner Weindorf, *Power-to-Liquids Potentiald and Perspectives for the Future Supply of Renewable Aviation Fuel*. 2016, german Environment Agency: Germany.
3. Grégorie Léonard; Davide Giulini; Diego Villareal-Singer, *Design and Evaluation of a High-Density Energy Storage Route with CO2 Re-Use, Water Electrolysis and Methanol Synthesis*. Computer Aided Chemical Engineering, 2016. **38**: p. 1797-1802.
4. Muhammad Arif Khan; Hongbin Zhao; Wenwen Zou; Zhe Chen, *Recent Progresses in Electrocatalysts for Water Electrolysis*. Electrochenical Energy Reviews, 2018. **1**: p. 483-530.
5. E. Fabbri; A. Habereder; K. Waltar; R. Kötz; T.J. Schmidt, *Developments and perspectives of oxide-based catalysts for the oxygen evolution reaction*. Catalysis Science and technology, 2014. **4**: p. 3800-3821.
6. Karthick Sriram, *Thermal and flow characterisation of a small scale alkaline electrolysis system for hydrogen production*, in *Process and Energy*. 2019, Delft University of Technology: Delft.
7. Stefania Marini; Paolo Salvi; Paolo Nelli; Rachele Pesenti; marco Villa; Mario Berrettoni; Giovanni Zangari; Yohannes Kiros, *Advanced alkaline water electrolysis*. Electrochimica Acta, 2012. **82**: p. 384-391.
8. Jason C. Ganley, *High temperature and pressure alkaline electrolysis*. International Journal of Hydrogen Energy, 2009. **34**: p. 3604-3611.
9. Kai Zeng and Dongke Zhang, *Recent progress in alkaline water electrolysis for hydrogen production and applications*. Progress in Energy and Combustion Science, 2010. **36**: p. 307-326.
10. Robert Phillips; Charles W. Dunnill, *Zero gap alkaline electrolysis cell design for renewable energy storage as hydrogen gas*. The Royal Society of Chemistry 2016. **6**: p. 100643-100651.
11. Maximilian Schalenbach; Geert Tjarks; Marcelo Carmo; Wiebke Lueke; Martin Mueller; Detlef Stolten, *Acidic or Alkaline? Towards a New Perspective on the Efficiency of Water Electrolysis*. Journal of The Electrochemical Society, 2016. **163**: p. 3197-3208.
12. S. Marini; P. Salvi; P. Nelli; R. Presenti, *Advanced alkaline water electrolysis*. Electrochimica Acta, 2012. **82**: p. 384-391.

13. Diogo M. F. Santos and César A. C. Sequeira, *Hydrogen Production By Alkaline Water Electrolysis*. Química Nova, 2013. **36**: p. 1176-1193.
14. Allen J. Bard; Larry R. Faulkner, *Electrochemical Methods*. Second Edition ed. 2001: John Wiley & Sons, Inc.
15. Tatsuya Shinagawa; Angel T. Garcia-Esparza; Kasuhiro Takanabe, *Insight on Tafel slopes from a microkinetic analysis of aqueous electrocatalysis for energy conversion*. Scientific Reports, 2015. **5:13801**: p. 1-21.
16. Nasir Mahmood; Yunduo Yao; Jing-Wen Zhang; Lun Pan; Xiangwen Zhang, *Electrocatalysts for Hydrogen Evolution in ALkaline Electrolytes: Mechanisms, CHallenges, and Prospective Solutions*. Electrocatalysis, 2018. **5**(1700464): p. 1-23.
17. Paola Quaino; Fernanda Juarez; Elizabeth Santos; Wolfgang Schmickler, *Volcano plots in hydrogen electrocatalysis-uses and abuses*. Beilstein Journal of Nanotechnology, 2014. **5**: p. 846-854.
18. B.E. Conway; G. Jerkiewicz, *Relation of energies and coverages of underpotential and overpotential deposited H at Pt and other metals to the 'volcano curve' for cathodic H2 evolution kinetics*. Electrochimica Acta, 2000. **45**: p. 4075-4083.
19. Kummara Naga Mahesh, *Design and Development of Proton Exchange Membrane Water Electrolyser and nano Carbon supported Palladium Electrocatalyst*, in *Department of Chemistry*. 2014, jawaharlal Nehru Technological University. p. 153.
20. Paul Flowers; Robert J. Lancashire. *General Properties of Transition Metals*. LibreTexts-Chemistry 2019.
21. Deyanda Flint. *Why are transition metals good catalysts?* 2017 [cited 2020; Available from: https://sciencing.com/why-are-transition-metals-good-catalysts-12342816.html.
22. Lars Egberts *Making hydrogen with cheap materials*.
23. Min-hua Shao; Ping Liu; Radoslav R. Adzic, *Superoxide Anion is the Intermediate in the Oxygen Reduction Reaction on Platinum Electrodes*. Journal of The American Chemical Society, 2006. **128**: p. 7408-7409.
24. Isabela C. Man; Hai-Yan Su; Federico Calle-Vallejo; Jan Rossmeisl, *Universality in Oxygen Evolution Electrocatalysis on Oxide Surfaces*. ChemCatChem, 2011. **3**(7): p. 1159-1165.
25. Xiaohong Li; Frank C. Walsh; Derek Pletcher, *Nickel based electrocatalysts for oxygen evolution in high current density, alkaline water electrolysers*. Physical Chemistry Chemical Physics, 2011. **13**(3): p. 1162-1167.

26. Smith RD; Prévot MS; Fagan RD; TRudel S; Berlinguette CP, *Water oxidation catalysis: electrocatalytic response to metal soichiometry in amorphous metal oxides films containing iron, cobalt and nickel*. Journal of The American Chemical Society, 2013. **31**(135): p. 11580-11586.
27. Subir Paul, *Electrodepositon Techniques to Synthesize Electrocatalytic Nanomaterials for High Energetic Electrodes for Battery and Fuel Cell*. Nanoscience & Nanotechnology 2015. **5**: p. 50-63.
28. C.A. Schuh; T.G. Nieh; T. Yanasaki, *Nanostructured Metals and Alloys Processing*. Scripta Materialia, 2002. **46**.
29. K. Zarebska; M. Kwiatkowski; M. Gniadek; M. Skompska, *Electrodeposition of Zn(OH)2, ZnO thin films and nanosheet-like Zn seed layers and influence of their morphology on the growth of nanorods*. Electrochimica Acta, 2013. **98**.
30. Lasia; H. Menard Y. Choquette; L. Brossard; A, *Investigation of hydrogen evolution on Raney-Nickel composite-coated electrodes*. Electrochimica Acta, 1990. **35**: p. 1251-1256.
31. C.A. Marozzi; A.C. Chialvo, *Development of electrode morphologies of interest in electrocatalysis. Part 2: Hydrogen evolution reaction on macroporous nickel electrodes*. Electrochimica Acta, 2001. **46**: p. 861-866.
32. I. Herraiz-Cardona, et al., *Porous Ni and Ni-Co Electrodeposits for Alkaline Water Electrolysis - Energy Saving*. International Journal of Chemical and Molecular Engineering, 2012. **6**: p. 823-829.
33. Michael E.G. Lyons; Michael P. Brandon, *A comparative study of the oxygen evolution reaction on oxidised nickel, cobalt and iron electrodes in base*. Journal of Electronalaytical Chemistry, 2010. **641**: p. 119-130.
34. James Landon; Ethan Demeter; Nilay Inoglu; Chris Keturakis; Israel E. Wachs, *Spectroscopic Characterization of Mixed Fe-Ni Oxide Electrocatalysts for the Oxygen Evolution Reaction in Alkaline Electrolytes*. American Chemical Society Catalysis 2012. **3**: p. 1793-1801.
35. Mary WC Louie; Alexis T. Bell, *An Investigation of Thin-Fil Ni-Fe Oxide catalysts for the Electrochemical Evolution of Oxygen*. Journal of The American Chemical Society, 2013: p. 26.
36. Aisha Alobaid;, Chunsheng Wang;, and Raymond A. Adomaintis, *Mechanism and Kinetics of HER and OER on NiFe LDH Films in Alkaline electrolyte*. The Electrochemical Society, 2018. **165**: p. J3395-J3404.
37. Juan J. Bravo-Suárez, *Review of The Synthesis of Layered Double Hydroxides: A thermodynamic approach*. Química Nova, 2004. **27**: p. 601-614.
38. B. M. Hunter; W. Hieringer; H. R. Winkler; H.B. Gray; A.M. Müller, *Effect of interlayer anions on [NiFe]-LDH nanosheet water oxidation activity*. Energy and Environment Science, 2016. **9**: p. 1734-1743.

39. Alexandra Inayat; Michael Klumpp; Wilhelm Schwieger, *The urea method for the direct synthesis of ZnAl layered double hydroxides with nitrate as the interlayer anion*. Applied Clay Science, 2011. **51**: p. 452-459.
40. Rui Li; Jingsong Xu; Qifa Pan; Jingwen Ba; Tao Tang; Wenhua Luo, *One-Step Synthesis of NiFe Layered Double Hydroxide nanosheet Array/N-Doped Graphite Foam Electrodes for Oxygen Evolution Reactions*. Chemistry Open, 2019. **8**: p. 1027-1032.
41. Jr. John Dwyer, James G. Hansel, and Tom Philips *Temperature Influence on the Flammability Limits of Heat Treating Atmospheres*. 2003.
42. Agfa Group. *Advancing the H2 industry with superior electrolysis membranes*. 2018; Available from: https://www.agfa.com/specialty-products/solutions/membranes/zirfon/.
43. Fuel Cell Store. *Pseudo-Reference Electrode*. 2020; Available from: https://www.fuelcellstore.com/pseudo-reference-electrode.
44. Daniel Chade; Leonard Berlouis; David Infield, *Evaluation of Raney nickel electrodes prepared by atmospheric plasma spraying for alkaline water electrolysers*. International Journal of Hydrogen Energy, 2013. **38**: p. 14380-14390.
45. Charles McCrory; Suho Jung; Jonas Peters, *Benchmarking Heterogenoeus Electrocatalysts for the Oxygen Evolution Reaction*. Journal of The American Chemical Society, 2013. **135**: p. 16977-16987.
46. Charles C. L. McCrory, et al., *Benchmarking Hydrogen Evolving Reaction and Oxygen Evolving Reaction Electrocatalysts for Solar Water Splitting Devices*. Journal of The American Chemical Society, 2015. **137**: p. 4347-4357.
47. Jingshan Luo; David A. Vermaas; Dongkin Bi; Anders Hagfeldt; Wilson A. Smith; Michael Grätzel, *Bipolar Membrane-Assisted Solar Water Splitting in Optimal pH*. Advanced Energy Materials, 2016. **6**: p. 7.
48. Kyung Ho Kim; Jin You Zheng; Woonsup Shin; Young Soo Kang, *Preparation of dendritic NiFe films by electrodeposition for oxygen evolution*. The Royal Society of Chemistry, 2012. **2**: p. 4759-4767.
49. Warwick University. *Scanning Electron Microscopy (SEM)*. 2010; Available from: https://warwick.ac.uk/fac/sci/physics/current/postgraduate/regs/mpagswarwick/ex5/techniques/structural/sem3/.
50. NanoPhysics Analytical Services. *SEM-EDX*. [cited 2020; Available from: https://www.nanophysics.nl/services-view/edx-analysis/.
51. Physical Electronics A Division of ULVAC-PHI. *XPS/ESCA*. 2020 [cited 2020; Available from: https://www.phi.com/surface-analysis-techniques/xps-esca.html.

52. G. Roventi; R. Fratesio; R.A. Della Guardia; G. Barucca, *Normal and anomalous codeposition of Zn-Ni alloys from chloride batch*. Journal of Applied Electrochemistry, 2000. **30**: p. 173-179.
53. V. Torabinejad; M. Aliofkhazraei; S. Assareh; M.H. Allahyarzadeh; A. Sabour Rouhaghdam, *Electrodeposition of Ni-Fe alloys, composites, and nano coatings-A review*. Journal of Alloys and Compunds, 2017. **691**: p. 841-859.
54. Zhiyi Lu; Wenwen Xu; Wei Zhu; Qiu Yang; Xiadong Lei; Junfeng Liu; Yaping Li; Xiaoming Sun; Xue Duan, *Three-dimensional NiFe layered double hydroxide film for high-efficiency oxygen evolution reaction*. The Royal Society of Chemistry, 2014. **50**: p. 6479-6482.
55. Spela Trafela; Janez Zavasnik; Saso Sturm; Kristuna Zuzek Rozman, *Formation of a Ni(OH)2/NiOOH active redox couple on nickel nanowires for formaldehyde detection in alkaline media*. Electrochimica Acta, 2019. **309**: p. 346-353.
56. Aneeya Kumar Samantara; Satyajit Ratha, *Metal Oxides/Chalcogenides and Composites Emerging Materials for Electrochemical Water Splitting*. 2019: Springer Nature Switzerland AG.
57. Jordi Creus; Jonathan De Tovar; Nuria Romero; Jordi García-Antón; Karine Philippot; Roger Bofill; Xavier Sala, *Ruthenium Nanoparticles for Catalytic Water Splitting* ChemSUsChem, 2019. **12**: p. 2493-2514.
58. Ian D. Sharp; Harry A. Atwater; Hans-Joachim Lewerenz, *Integrated Solar Fuel Generators*. Energy and Environment Series. 2019: The Royal Society of Chemistry.
59. Vijaya Sankar Kalimuthu; Rinat Attias; Yoed Tsur, *Electrochemical impedance spectra of RuO2 during oxygen evolution reaction studied by the distribution function of relaxation times*. Electrochemistry Communications, 2020. **110**: p. 6.
60. A.J. Appleby; G. Crepy; J. Jacquelin, *High Efficiency Water Electrolysis in Alkaline Solution*. International Journal of Hydrogen Energy, 1978. **3**: p. 21-37.
61. N Krstajić; M Popović; B Grgur; M Vojnović; D Šepa, *On the kinetics of the hydrogen evolution reaction on nickel in alkaline solution: Part II. Effect of temperature* Journal of Electronalaytical Chemistry, 2001. **512**(1-2): p. 27-35.
62. John Bockris, *Comprehensive Treatise of Electrochemistry* Comprehensive Treatise of Electrochemistry. Vol. 2. 1981, US.
63. M.H.; Kissel Miles, G.; Lu, P.W.T.; Srinivasan, S., *Effect of temperature on electrode kinetic parameters for hydrogen and oxygen evolution reactions on nickel electrodes in alkaline solutions*. Journal Electrochemistry Society, 1976. **123:3**.
64. M. H. Miles; Y. H. Huang; S. Srinivasan, *The Oxygen Electrode Reaction in Alkaline Solutions on Oxide Electrodes Prepared by the Thermal Decomposition Method*. Journal of The Electrochemical Society, 1978. **125**(12): p. 1931-1934.

65. Alejandro N. Colli; Hubert H. Girault; Alberto Battistel, *Non-Precious Electrodes for Practical Alkaline Water Electrolysis*. Materials, 2019. **12**(1336): p. 1-17.

66. Sophia Mellsop, *Development of Electrocatalysts for the Oxygen Evolution Reaction in ALkaline Water Electrolysis*, in *Cehmical Engineering*. 2016, University of Canterbury. p. 132.

67. J.W. Evans, *Metal Production: Electrometallurgy*. Encyclopedia of Materials: Science and Technology. 2003.

68. Felix Rieck gennannt Best; Jürgen Koch; Gerhard Lilienkamp; Franz Körkemeyer; hans Jürgen Maier; Jürgen Caro; Karsten Lange, *Spiky Nickel Electrodes for Electrochemical Oxygeb Evolution Catalysys by Femtosecond Laser Structuring*. International Journal of Electrochemistry, 2018. **2018**: p. 12.

69. Anne E. Mauer; Donald W. Kirk; Steven J. Thorpe, *The role of iron in the prevention of nickel electrode deactivation in alkaline electrolysis*. Electrochimica Acta, 2006. **52**: p. 3505-3509.

70. Florian D. Speck; Kevan E. Dettelback; Rebecca S. Sherbo; Danielle A. Salvatore; Aoxue Huang; Curtis P. Berlinguette, *On the Electrolytic Stability of Iron-Nickel Oxides*. Chem, 2017. **2**: p. 590-597.

71. Jia-Ming Ye; Ding-Hong; Fang Li; Yu-Ling Li; Jian-Bo He, *Roles of Soluble Species in Alkaline Oxygen Evolution Reaction on Nickel Anode*. Chemical Communications, 2018: p. 5.

72. F. Beck; R. Kaus; M. Oberst, *Transpassive Dissolution of Iron to Ferrate(VI) in Concentrated Alkali Hydroxide Solutions*. Electrochimica Acta, 1985. **30**: p. 173-183.

73. Felix Frey, *Experimental set-up for bubble behaviour in a high pressure alkaline electrolyte*, in *Institute of Nuclear and Energy Technologies*. 2016, Karlsruhe Institute of technology: karlsruhe.

74. IRENA, *Future of Solar Photovoltaic: Deployment, investment, technology, grid integration and socio-economic aspects*. 2019: Abu Dhabi.

75. Fuel Cell Store. *Alkaline Water Electrolyzer Stack - 20 Cell*. 2020 May 2020]; Available from: https://www.fuelcellstore.com/alkaline-water-electrolyzer-stack-20-cell.

A

Maximum calculated temperature inside the electrolysis cell

The power lost during the operation of the electrolysis cell can be considered as the voltage not used to drive the reaction times the current (*IV*). The power is assumed to be lost in the form of heat. The thermoneutral voltage (1.48V) was assumed to be the minimum voltage needed for the electrolysis reaction and 2.25 V was the expected maximum voltage for a 5 A current. The experimental voltage was obtained with a smooth nickel electrode in an open electrolysis cell. The power loss is expressed in Equation A1:

$$P_{loss} = IV = (5A)(0.77V) = 3.85\ W \tag{A.1}$$

The maximum temperature inside the cell is expected during the longest experiments. The stability tests consist in 90 cycles where the cell operates under atmospheric conditions at 5 A during 75s and is turned off during 25s. This means that in an experiment the cell will operate at 5 A for 6750s. The thermal energy is assumed to accumulate completely in the electrolyte solution, in reality it is not the case as heat conduction and convection would cool off the cell. The exit of matter (gas) from the cell has also a cooling effect. The maximum theoretical change in temperature is calculated in Equation A.2:

$$\Delta T = \frac{P_{loss}t}{mC} = \frac{3.85W(6750s)}{75g(\frac{4.17J}{g°C})} = 83.7°C \tag{A.2}$$

where *t* is the time the cell operates at 5A, *m* is the mass of the electrolyte solution and *C* is the water heat capacity. Water heat capacity was used as no empirical data for 30% wt. KOH was found. Assuming that the cell starts operation at a temperature of 20ºC, the final temperature in the cell would reach 103.7ºC. This does not represent a problem for the materials used to build the cell, stainless steel and CPVC. CPVC has

heat deflection temperature of 103 ºC at a pressure of 18 bar[1] so its mechanical stability is assured at atmospheric conditions. A flexible support was employed to close the cell to avoid deformation of the material when heated.

[1] Inc., I. P. S. "Typical Properties of PVC and CPVC." 2020, from https://www.ipolymer.com/pdf/PVC.pdf.

B

Double-layer capacitance

Besides the faradic processes occurring during water electrolysis at the electrode surface like oxidation/reduction of the surface and HER or OER, there is a capacitive process happening as well. This last process is related to the "charging" of the adjacent electrolyte. When applying a voltage to an electrode, the ions al the electrolyte will organize close to the electrode surface to balance the charge of electrons, for example.

The accumulated ions on the surface are organized in two layers of adsorbed ions and solvent molecules. The ordered first layer of ions is named internal Helmholtz layer (IHL) while the second and less organized one is referred to as outer Helmholtz layer (see Figure B.1)[1]. The separation of charges creates a potential difference between the electrode surface and the bulk of the solution. This phenomenon causes a capacitive behavior.

Cyclic voltammetry can be employed to measure the magnitude of this interaction with the electrolyte by running cycles with varying scanning rate in a non-faradic potential region. The capacitive current (i_c) can be related to the scanning rate (v) and double-layer capacitance (C_{DL}) according to Equation B.1.[2]

$$i_c = vC_{DL} \tag{B.1}$$

[1]Zeng, K. and D. Zhang (2010). "Recent progress in alkaline water electrolysis for hydrogen production and applications." Progress in Energy and Combustion Science **36**: 307-326.
[2] Peters, C. M. S. J. J. (2013). "Benchmarking Heterogeneoeus Electrocatalysts for the Oxygen Evolution Reaction." Journal of The American Chemical Society **135**: 16977-16987.

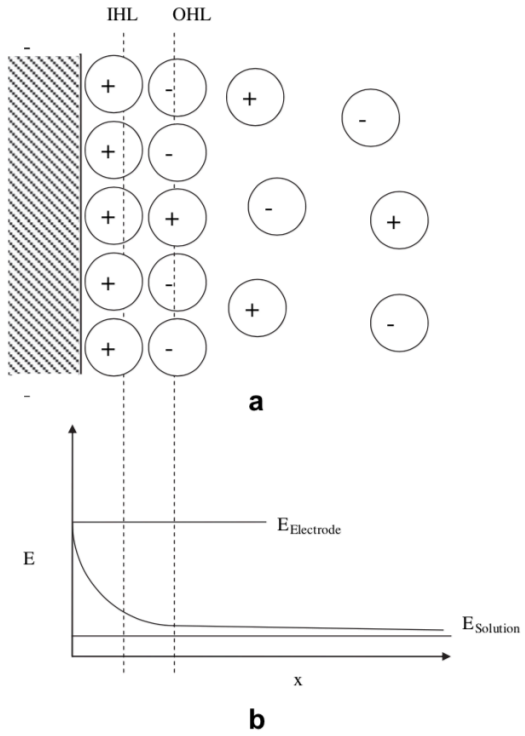

Figure B.1. Double layer and potential distribution at the electrode surface.[1]

[1]Zeng, K. and D. Zhang (2010). "Recent progress in alkaline water electrolysis for hydrogen production and applications." Progress in Energy and Combustion Science **36**: 307-326.

C

External cell temperature during experiments

This section presents the temperature cell was only measured externally as the sensor (thermistor) used cannot withstand the alkaline conditions of the electrolyte. The external temperature is only taken as an indication of temperature change inside the cell.

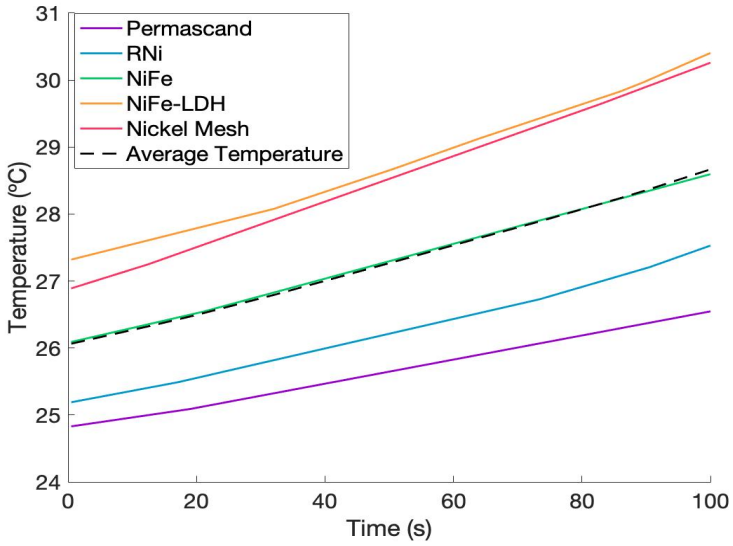

Figure C.1. External cell temperature recorded during performance tests. This temperature records refer to Figures 4.6 and 4.7 in the results section. Average temperature: 27.5 ºC.

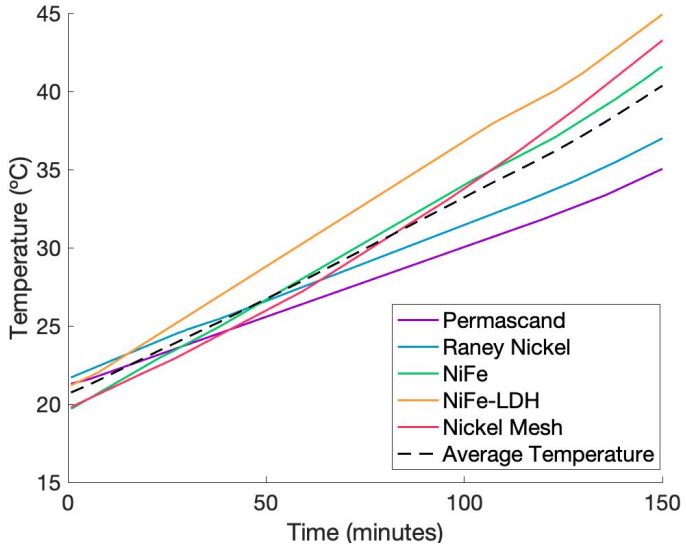

Figure C.2. External cell temperature recorded during stability tests. This temperature records refer to Figures 4.8 and 4.9 in the results section. Average temperature: 32.7 ºC.

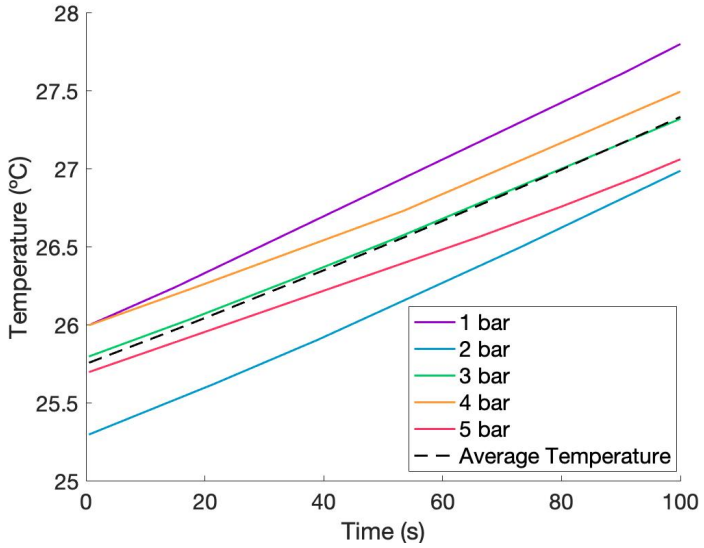

Figure C.3. External cell temperature recorded during pressure tests. This temperature records refer to Figure 4.13 in the results section. Average temperature: 26.5 ºC.

D

Curve fitting considering the thermodynamic effect of pressurizing H_2 and O_2

The experimental data for the pressurized tests only covers the 1-5 bar range. For ZEF it is interesting to estimate how the cell potential would behave at higher pressures. The experiments were carried out with N_2 to purge the product gases and to pressurize the cell. Pressurizing with N_2 affects parameters such as bubble size; however, it does not affect the thermodynamics of water electrolysis. ZEF plans to pressurize H_2 and O_2 which does have an effect on the equilibrium potential.

Equation D.1 considers the thermodynamic effect as well as the observed pressure effect

$$V_{166}(P) = \frac{a}{P} + \frac{RT}{nF}\ln\left(\frac{P_{H_2}P_{O_2}^{1/2}}{a_{H_2O}}\right) + b \quad \text{(D.1)}$$

The factor *a* indicates the observed relationship with pressure and voltage in Figure 4.16. The term *b* includes the cell voltage segment that is not affected by pressure. *P* is the partial pressure of the gases, since they would be pressurized in their separate chambers, *P* is the same for both gases and equal to the system pressure. a_{H_2O} is water activity assumed to be equal to 1.

Figure D.1 presents the results obtained for the curve fitting resulting in Equation D.2 with and R-square value of 0.97.

$$V_{166}(P) = \frac{0.339}{P} + \frac{RT}{nF}\ln\left(\frac{P_{H_2}P_{O_2}^{1/2}}{a_{H_2O}}\right) + 1.646 \quad \text{(D.2)}$$

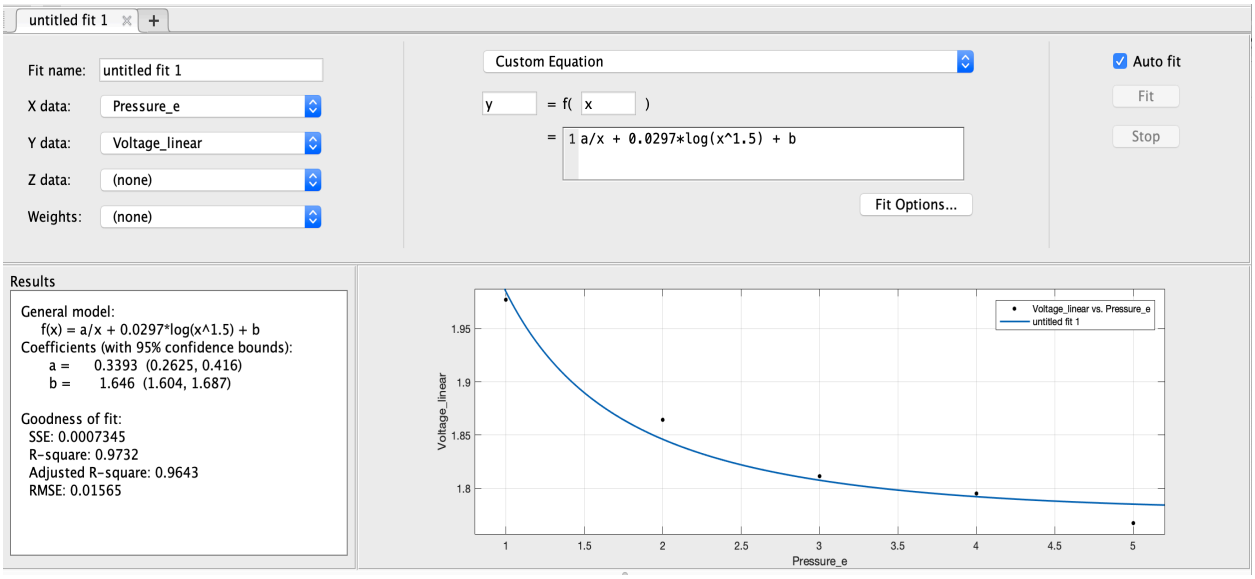

Figure D.1. Screen capture of curve fitting app in Matlab. Experimental data points obtained from Figure 4.14 in the results section.

E

X-ray spectroscopy analysis: surface composition

E.1 Permascand

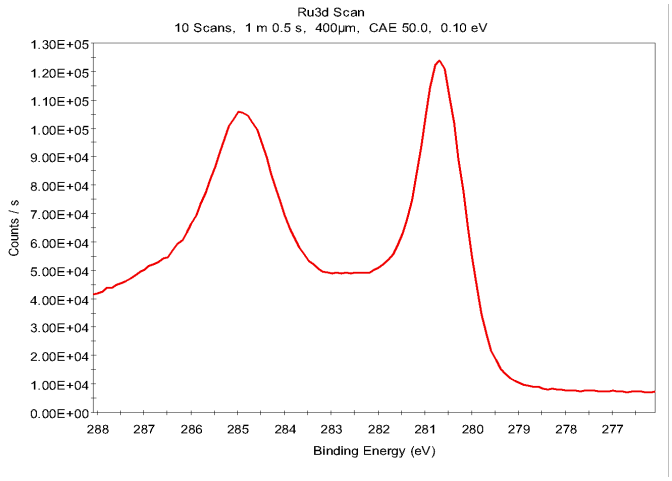

Figure E.1.1 Ruthenium scan for the fresh Permascand electrode. Spectrum corresponds to RuO_2[1].

Figure E.1.2 indicates that the content of RuO_2 decreased after the stability tests especially for the anode (Fig. E.1.2 R). The slight change in spectrum shown in Figure E.1.2 R might indicate an increase in $RuO_x(2<x\leq3)$ content[1].

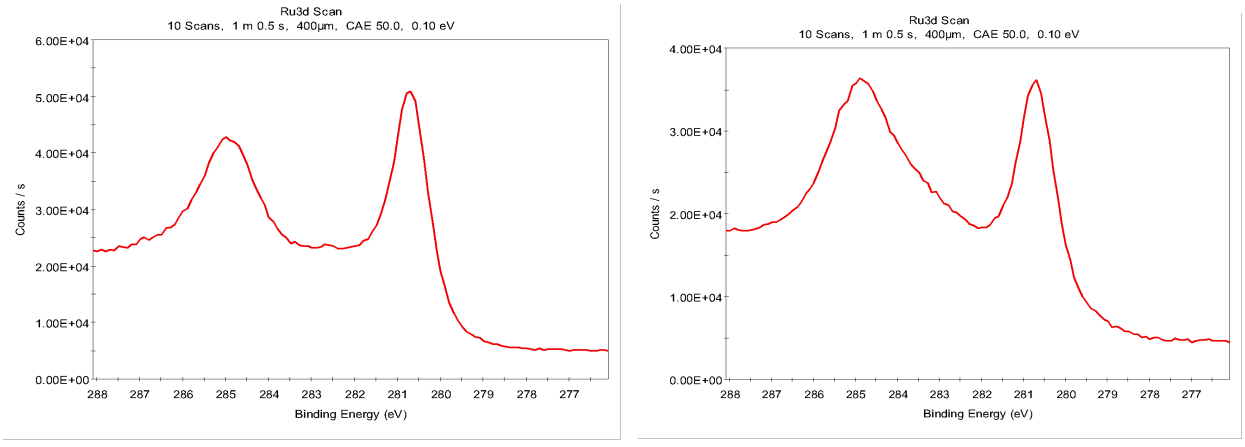

Figure E.1.2 Ruthenium scan for the sepnt Permascand electrode (L) cathode and (R) anode.

[1] Ribera, R. C. (2017). Growth and thermal oxidation of Ru and ZrO2 thin films as oxidation protective layers. Chemical Engineering. Enschede, University of Twente. **PhD**.

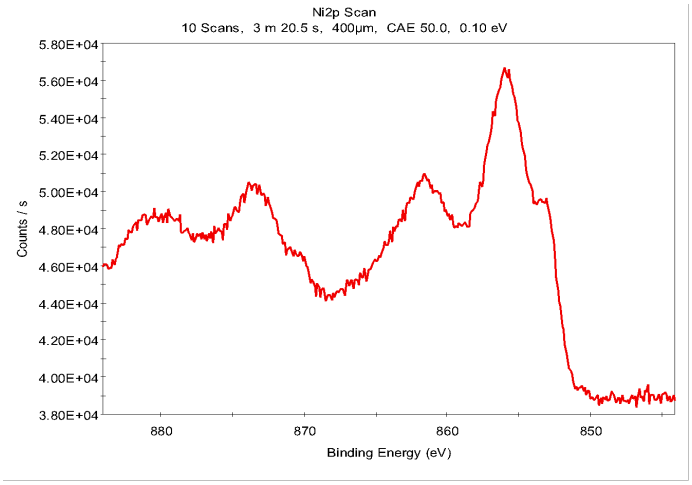

Figure E.1.3 Nickel scan for the fresh Permascand electrode. Spectrum corresponds to a mixture of NiO and $Ni(OH)_2$[1].

Figure E.1.4 indicates that nickel is present only as $Ni(OH)_2$ in the spent samples. No clear evidence of the presence of Ni^{3+} was observed in the results[2].

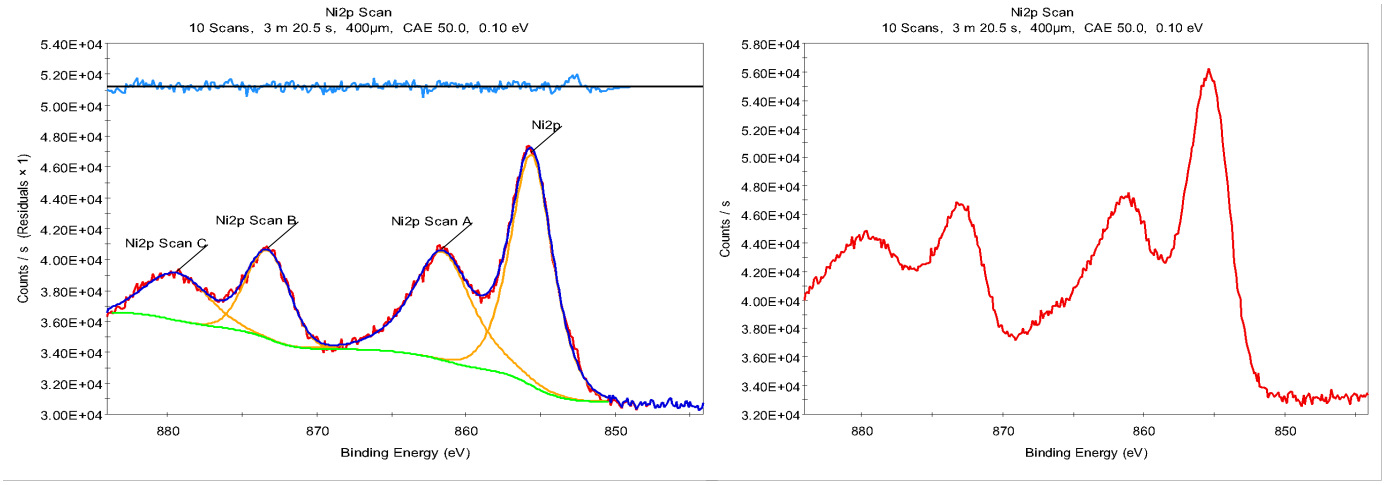

Figure E.1.4 Nickel scan for the sepnt Permascand electrode (L) cathode and (R) anode. Spectra corresponds to $Ni(OH)_2$

[1] Scientific, T. F. (2013). "XPS simplified." thermo scientific XPS. 2020, from https://xpssimplified.com/elements/nickel.php.

[2] Lu, T. Z. Z. C. P. Z. H. M. Z. G. H. W. Y. (2017). "Transition metal ions regulated oxygen evolution reaction performance of Ni-based hydroxides hierarchical nanoarrays." Scientific Reports **7**.

E.2 Raney Nickel (RNi)

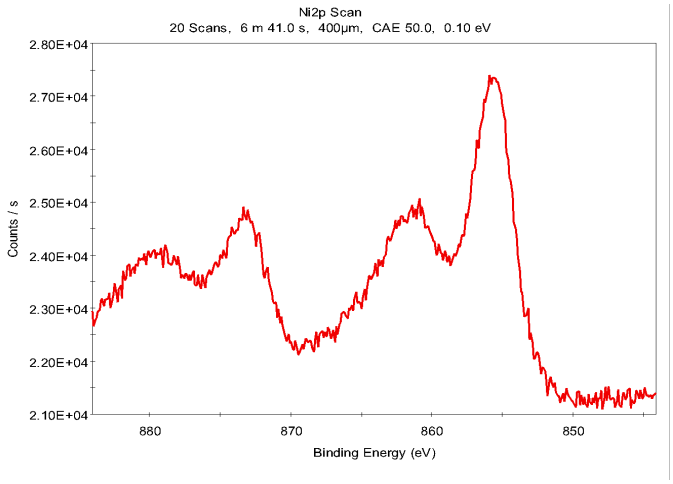

Figure E.2.1 Nickel scan for the fresh RNi electrode. Spectrum corresponds to Ni(OH)[1].

Figure E.2.2 indicates that nickel is present only as $Ni(OH)_2$ in the spent samples. No clear evidence of the presence of Ni^{3+} was observed in the results[1].

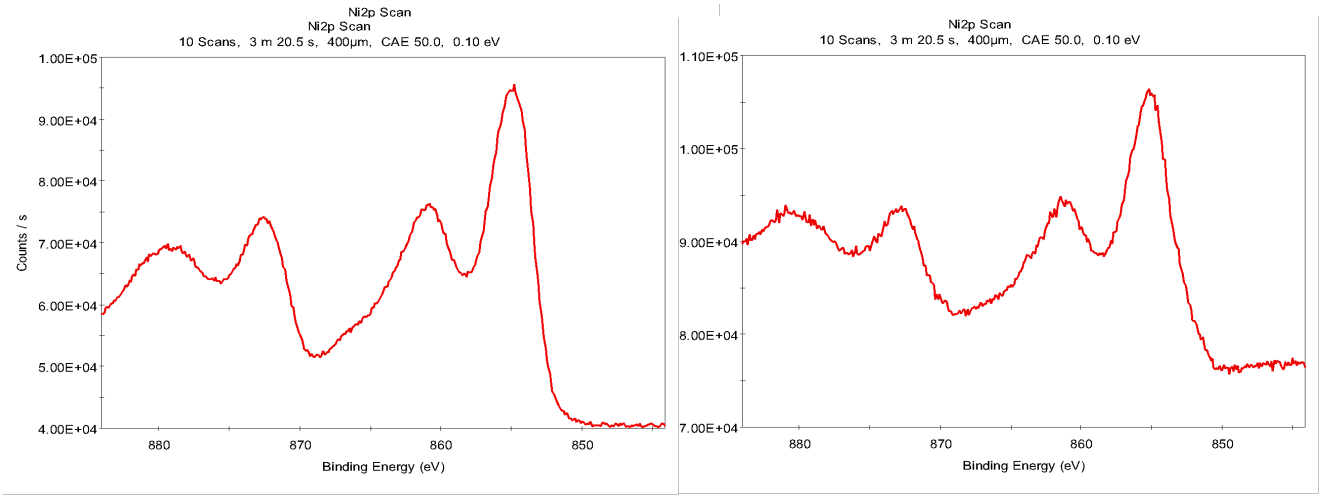

Figure E.2.2 Nickel scan for the sepnt RNi electrode (L) cathode and (R) anode. Spectra corresponds to Ni(OH)[1].

[1] Lu, T. Z. Z. C. P. Z. H. M. Z. G. H. W. Y. (2017). "Transition metal ions regulated oxygen evolution reaction performance of Ni-based hydroxides hierarchical nanoarrays." Scientific Reports **7**.

E.3 NiFe

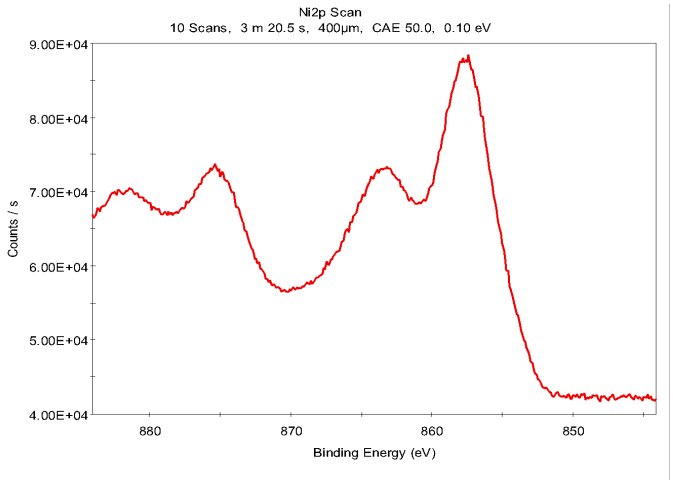

Figure E.3.1 Nickel scan for the fresh NiFe electrode. Spectrum corresponds to Ni(OH)[1].

Figure E.3.2 indicates that nickel is present only as $Ni(OH)_2$ in the spent samples. No clear evidence of the presence of Ni^{3+} was observed in the results[1].

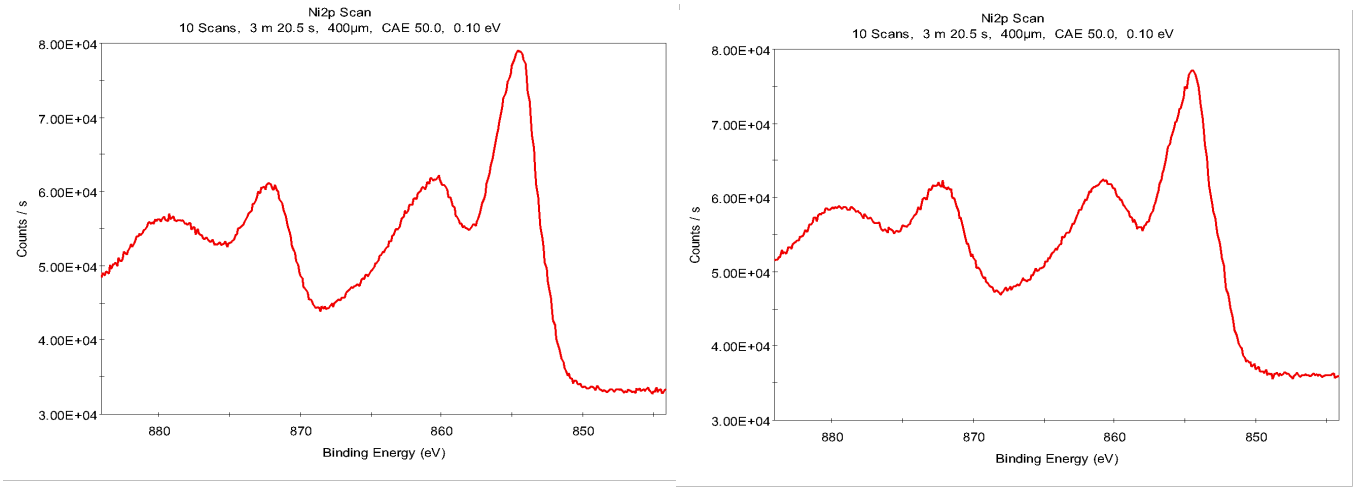

Figure E.3.2 Nickel scan for the sepnt NiFe electrode (L) cathode and (R) anode. Spectra correspond to Ni(OH)[1].

[1] Lu, T. Z. Z. C. P. Z. H. M. Z. G. H. W. Y. (2017). "Transition metal ions regulated oxygen evolution reaction performance of Ni-based hydroxides hierarchical nanoarrays." Scientific Reports **7**.

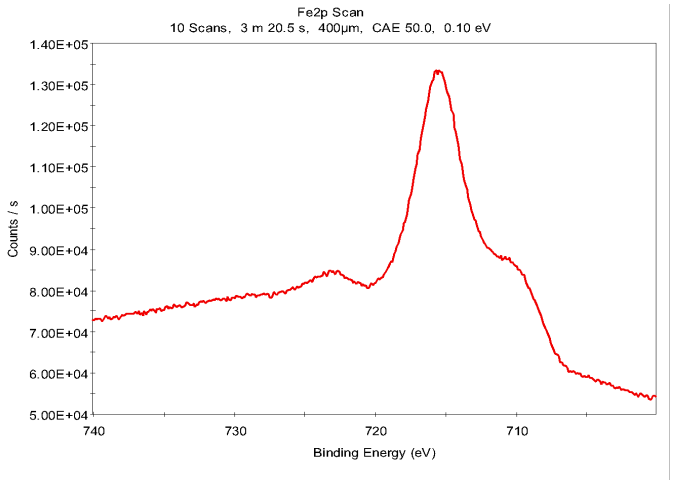

Figure E.3.3 Iron scan for the fresh NiFe electrode. The spectrum corresponds to a mixture of Fe^{2+} and Fe^{3+} species[1].

Figure E.3.4 present a similar spectrum for both cathode (L) and anode. The spent electrodes show a less defined peak at around 708 eV indicating a decrease in the content of Fe^{2+} [1].

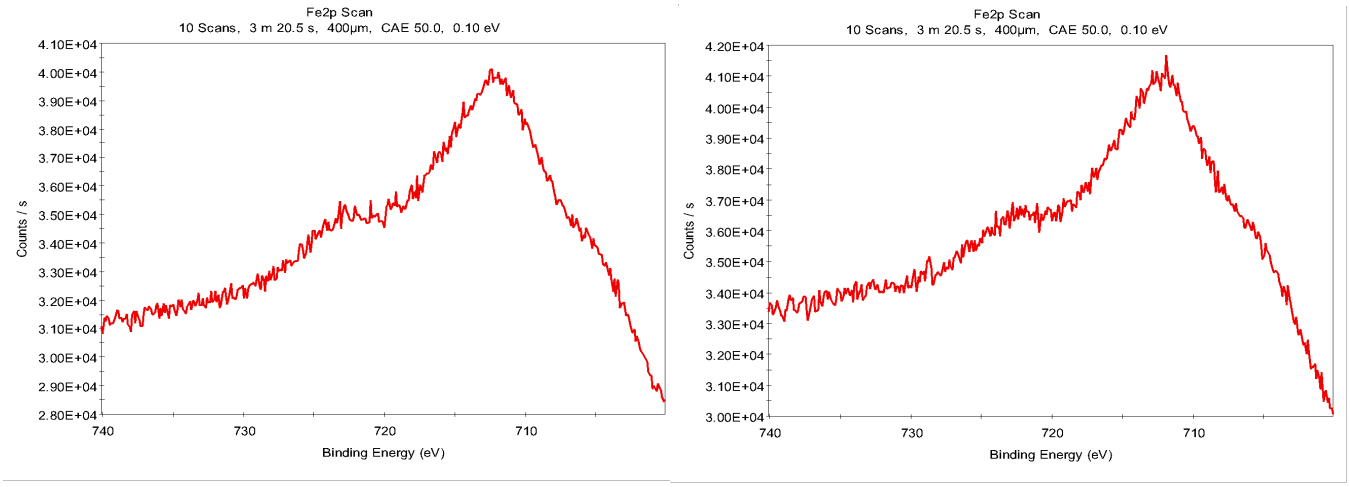

Figure E.3.4 Iron scan for the sepent NiFe electrode (L) cathode and (R) anode. The The spectra corresponds to a mixture of Fe^{2+} and Fe^{3+} species[1].

[1] Lu, T. Z. Z. C. P. Z. H. M. Z. G. H. W. Y. (2017). "Transition metal ions regulated oxygen evolution reaction performance of Ni-based hydroxides hierarchical nanoarrays." Scientific Reports **7**.

E.4 NiFe-LDH

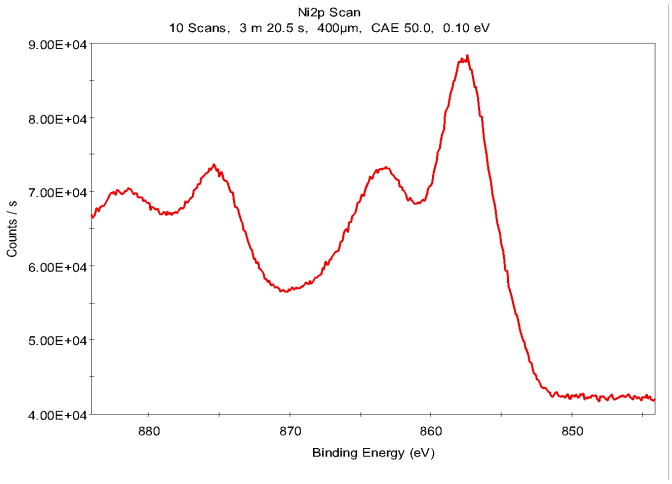

Figure E.4.1 Nickel scan for the fresh NiFe-LDH electrode. The spectrum corresponds to $Ni(OH)_2$.

Figure E.1.4 indicates that nickel is present only as $Ni(OH)_2$ in the spent samples. No clear evidence of the presence of Ni^{3+} was observed in the results[1].

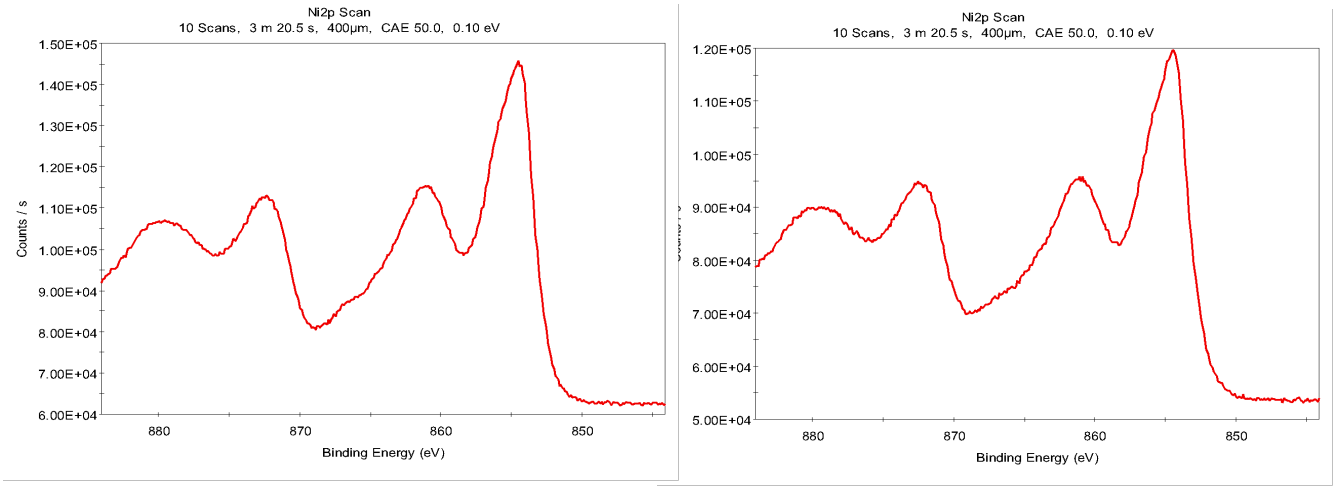

Figure E.4.2 Nickel scan for the sepnt NiFe-LDH electrode (L) cathode and (R) anode. The spectra correspond to $Ni(OH)_2$.

[1] Lu, T. Z. Z. C. P. Z. H. M. Z. G. H. W. Y. (2017). "Transition metal ions regulated oxygen evolution reaction performance of Ni-based hydroxides hierarchical nanoarrays." Scientific Reports **7**.

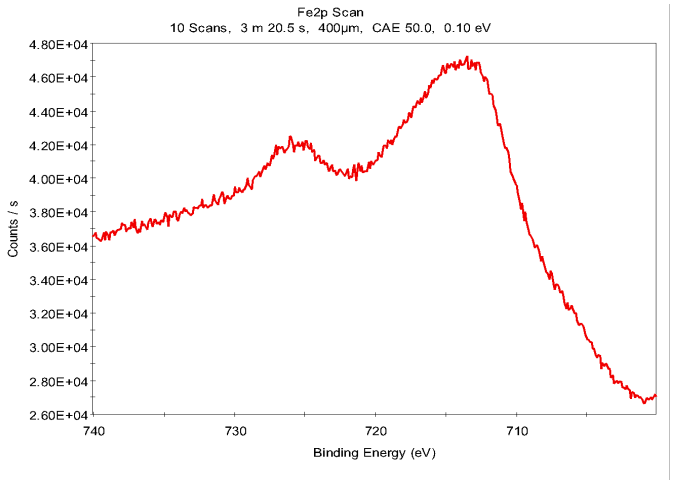

Figure E.4.3 Iron scan for the fresh NiFe-LDH electrode. Spectrum corresponds to Fe^{3+}

Figure E.4.4 indicates that iron is also present as Fe^{3+} in the spent electrodes[1].

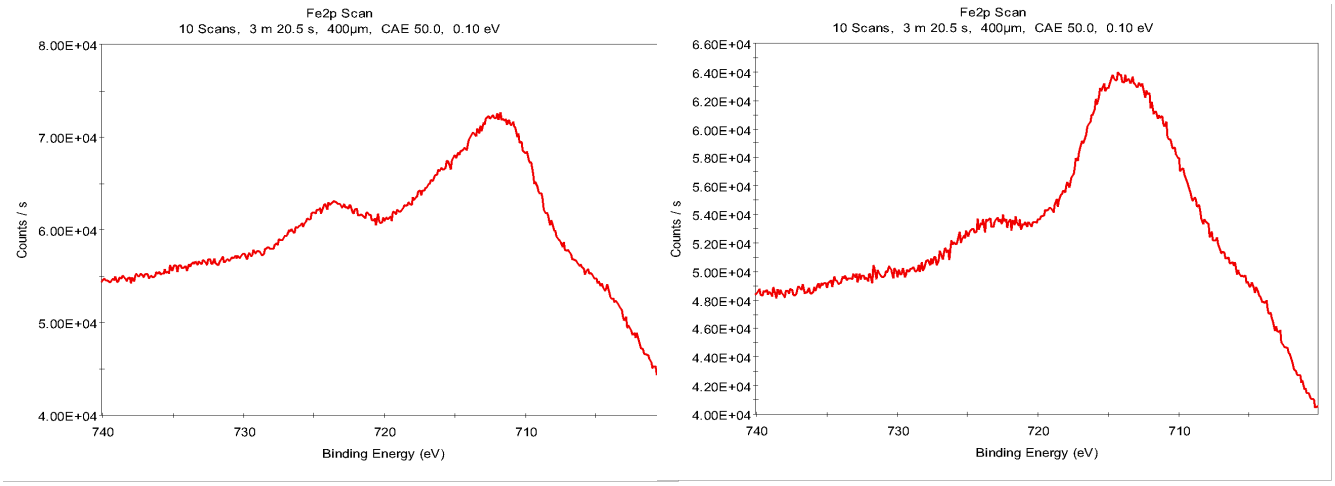

Figure E.4.4 Iron scan for the sepnt NiFe-LDH electrode (L) cathode and (R) anode. Spectra corresponds to Fe^{3+}.

[1] Lu, T. Z. Z. C. P. Z. H. M. Z. G. H. W. Y. (2017). "Transition metal ions regulated oxygen evolution reaction performance of Ni-based hydroxides hierarchical nanoarrays." Scientific Reports **7**.

E.5 Nickel mesh

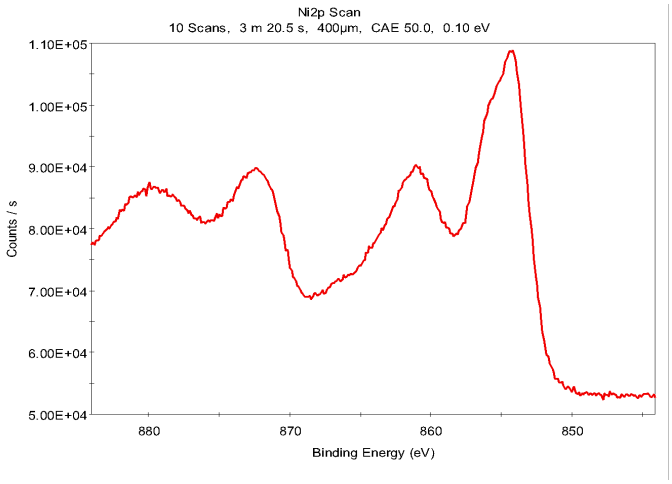

Figure E.5 Nickel scan for the fresh Nickel mesh electrode. The spectrum corresponds to $Ni(OH)_2$.[1]

[1] Lu, T. Z. Z. C. P. Z. H. M. Z. G. H. W. Y. (2017). "Transition metal ions regulated oxygen evolution reaction performance of Ni-based hydroxides hierarchical nanoarrays." Scientific Reports **7**.

F

Material costs estimation for electrodes

Table F.1. Mass percentage composition in the deposited film.

	Mass % XPS
Permascand	
O	24.83
Al	0.85
Ni	16.55
Ru	52.39
Cl	3.68
Si	1.67
Raney Nickel (RNi)	
O	32.35
Ni	10.57
Zn	53.67
Si	3.39
NiFe	
O	38.03
Ni	21.41
Fe	40.55
NiFe-LDH	
O	33.66
Ni	36.28
Fe	18.53
Si	11.50

Table F.2. Weight of deposited films and substrate.

	Weight (g)
Permascand film	0.6285
RNi film	0.6934
NiFe film	0.0941
NiFe-LDH film	0.3278
Nickel mesh (substrate)	8.6835

Table F.3. Metal and substrate costs.

	Cost per gram (€)
Ruthenium[1]	7.98
Nickel[1]	0.01
Iron (stainless steel)[2]	0.002
Zinc[1]	0.002
Cost of Nickel substrate (€)	2

Table F.4. Cost of electrode materials.

	Amount of metal (g)			
Metal	Permascand	RNi	NiFe	NiFe-LDH
Ruthenium	0.32927765	-	-	-
Nickel	0.1040640	0.0733336	0.0201509	0.1189443
Iron	-	-	0.0381626	0.0607709
Zinc	-	0.3721655	-	-
Cost of electrode (metals+substrate) (€)	4.6286763	2.001477	2.0002778	2.0013109

[1] Mining.com (2020). "Commodity and Metal Prices." from https://www.infomine.com/investment/metal-prices/.
[2] MetalMiner (2020). "Stainless Steel." from https://agmetalminer.com/metal-prices/stainless-steel/.

G

Electrode and cell pictures

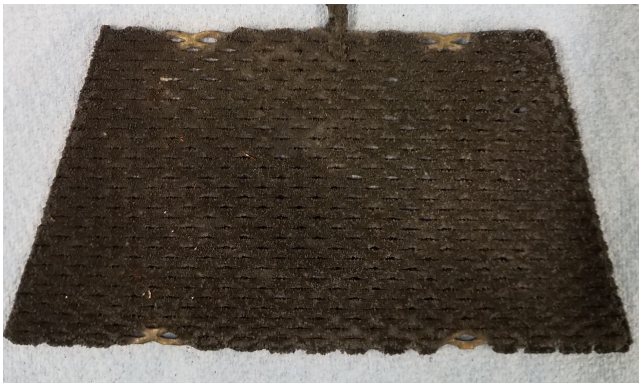

Figure G.1. RNi electrode.

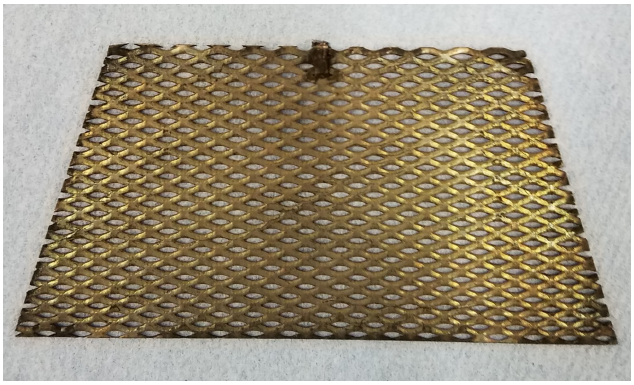

Figure G.2. NiFe electrode.

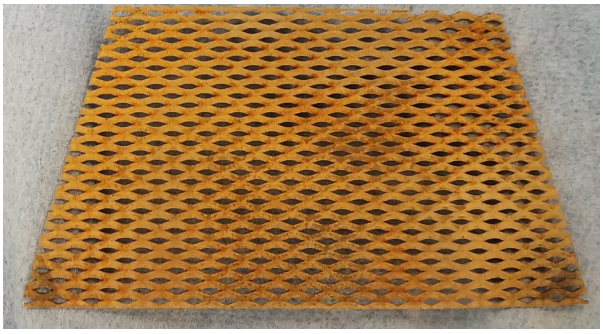

Figure G.3. NiFe-LDH electrode.

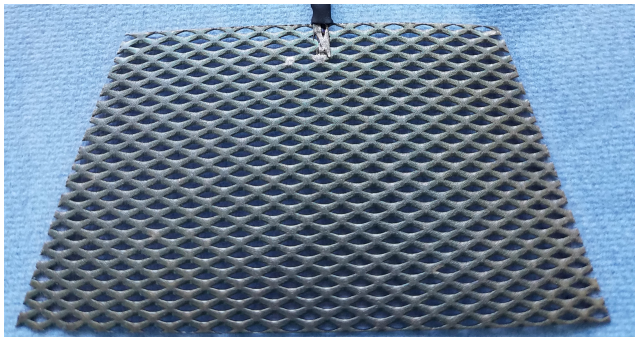

Figure G.4. Nickel Mesh.

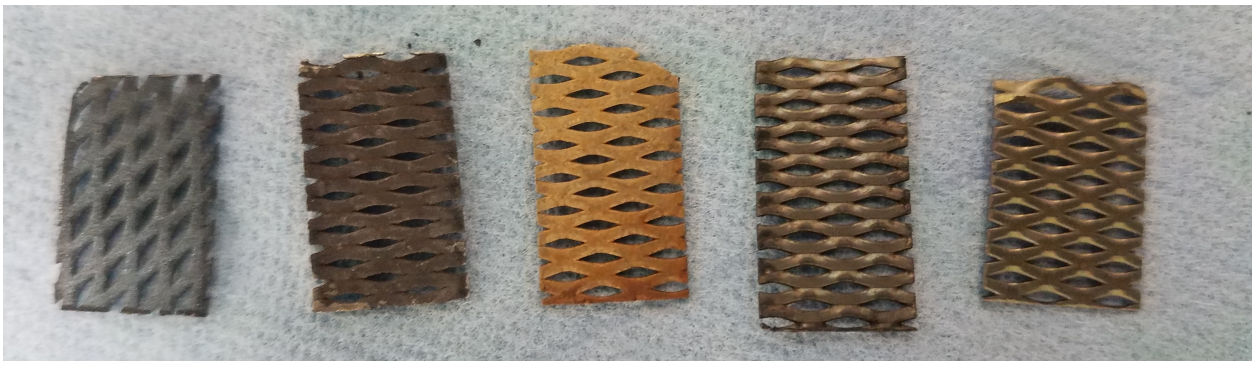

Figure G.5. Electrode fragments for XPS analysis. From left to right: Permascand, RNi, NiFe-LDH, NiFe and Nickel mesh.

Figure G.6. Frontal view of both sides of electrolysis cell.